University of Geneva

DQMP — Departement of Quantum Matter Physics

# Morphology and nanomechanical properties of snake scale microstructures

**Master Thesis**

*Presented to the Faculty of Sciences of the University of Geneva for a degree of Master in Physics*

By

**Loïc Musy**

**Supervisors:**

Prof. Patrycja Paruch

Dr. Iaroslav Gaponenko

2019

# Acknowledgements

This work was performed in the context of a Master in Physics at the Departement of Quantum Matter Physics at the University of Geneva, under the supervision of Prof. Patrycja Paruch and Dr. Iaroslav Gaponenko.

I would like to thank both of them for the masterful balance of guidance and autonomy provided throughout the necessary learning process. Even giving me the opportunity to represent the group as I presented this work at the 2019 *Deutsche Physikalische Gesellschaft* spring meeting. I would also like to give special thanks to Iaroslav who always promotes a tinkering mindset in the pursuit of science.

I am grateful to the jury members for accepting to review the present work.

I would also like to acknowledge all of the department members, especially Christian, Guillaume, Philippe, Kumara, Ralph, Marc, Mireille and Marios, for their friendly welcome, for all the lunch breaks spent together and fun extra-work activities.

Many thanks to the *Vivarium de Meyrin*, and especially to Raul Gonzalez and the vivarium team members for the snake sheds. Special recognition goes to Prof. Dragan Damjanovic for his help with the pyroelectric measurements and to Dr. Jérémy Teyssier for the contact angles measurements. This whole project would not have been possible without these collaborations.

Warm thanks to my family and friends, and especially to my fiancée Delphine Steiner who has been by my side for many years.

I would like to thank Claire Wuillemin for the tedious work of proofreading of the manuscript.

Last but not least, I would like to thank all the other students who pursued the study of physics alongside me, especially Gabriel Giardina, Adrien Bercher, Rayan Chtourou and Kassandra Caddoux. Without them these few years would have been a lot more challenging and less enjoyable.

# Contents

# List of Figures

# List of Tables

# Nomenclature

| | |
|---|---|
| AFM | Atomic Force Microscop(y/e) |
| BE | Band-excitation |
| GUI | Graphical User Interface |
| HOPG | Highly Oriented Pyrolytic Graphite |
| LFM | Lateral Force Microscopy |
| PS-LDPE | Polystyrene — Low-Density PolyEthylene |
| R.Pi | Raspberry Pi |
| SEM | Scanning Electron Microscop(y/e) |
| SFE | Schottky Field Emission |
| SPM | Scanning Probe Microscop(y/e) |

# 1 Introduction

Snakes belong to the few classes of legless vertebrates, making them rather peculiar in the animal kingdom due to their method of locomotion. In the absence of limbs, legless squamates use a variety of locomotion techniques, combining muscle contraction, lifting of the body, pressure on the substrate and scale orientation [1]: The most well-known technique is **lateral undulation**, where the snake creates undulation of its body by a periodic contraction of the muscles. When a bend enters in contact with an object, a reaction force will be applied on the snake, and as during this movement the lateral forces cancel each other, the resulting force propels the snake forward. On a smoother substrate, the snake will use **sidewinding**, which allows for faster movement than lateral undulation on smooth surfaces. During sidewinding, the snake is initially entirely in contact with the substrate, then lifts the upper and lower parts of its body, forming a U-shape with its middle section in contact with the ground. The reptile then moves the middle part of its body, resulting in a motion resembling a series of lateral jumps. **Concertina locomotion** is used mostly in confined environments, such as in tunnels. This mode is a continuous repetition of stretch and drag movements, which make use of the walls to push the snake forward. **Rectilinear locomotion** is the slowest and quietest of the techniques and consists of a series of pushes and pulls of the ventral scales on the ground. Due to the friction anisotropy of the ventral scales, this allows for a forward movement on the ground. **Slide-pushing** is the last locomotion technique and happens when the snake is on a slippery surface trying to move with large undulations, which leads to sliding.

The study of snake bone and muscle structure in order to explain their locomotion techniques goes as far back as 1932 [2], with the investigation of the effect of the arrangement of vertebrae and muscles on the in-plane flexibility of snakes. However, it is now well accepted that in all these different locomotion techniques the contact between the substrate and the snake plays a key role. The quality of this contact depends on the size, orientation and mechanical properties of the snake's ventral scales. Lateral scales are also expected to be of importance for locomotion in arboreal or burrowing species, and can thus be a target for natural selection pressure to adapt to the snake's environment.

Snake scales often present complex periodic three-dimensional structures as first illustrated by Schöttler [3] in 1938[1], and mentioned as far back as 1873 by Leydig [5]. In 2012 Schmidt & Gorb [6] carried out an analysis of the scale microstructures of multiple species from the *Pythonidae*, *Elapinae*, *Boidae* and *Hydrophiinae* families, showing a large variety of arranged structures. This study was, in our knowledge, the first large study of structures using scanning electron microscopy (SEM) and was followed by the work of Arrigo & al. [7], a systematic study of the morphology of thousands of snakes by SEM, leading to an evolutionary classification of the microstructures on snakes scales.

Like many vertebrate epithelial structures such as feathers, hairs or spines, the scales themselves are composed of keratin, whose macroscopic mechanical properties are well known [8]. However, despite a good understanding of the morphology and macroscale mechanical properties of snake scales, a comparably well detailed description of the mechanical properties at the local scale is largely lacking. Whilst several scanning probe microscopy (SPM) studies [9–11] have been carried out - showing properties such as friction anisotropy, self-cleaning and the determination of the layered structure of the keratin - they have generally been limited to a small number of species. The motivation behind the present study is to examine the local mechanical properties of a broader selection of species, encompassing multiple families with a variety of microstructure morphologies, and ranging across diverse habitats, in the hope of identifying correlation between the mechanical properties and either the phylogeny or the natural habitat of the snake.[2]

[1] A 1931 study on the comparison of the structures in the *Bulletin of the Antiven Institute of America* by Picado is mentioned in the article by Hoge & Souza [4]. Unfortunately, we were not able to find a copy of this reference

[2] Apart from their role in snake locomotion, we note that snake scale microstructures have also been widely studied for the

In this thesis, we use SEM and atomic force microscopy (AFM) techniques to extract the morphological and nanomechanical properties of snakes scales at the nanometre scale. In chapter 2, we first define the necessary theory for this project: elasticity (leading to the formal development of the Hertz model), friction, interaction of surfaces with water and pyroelectricity. We present in chapter 3 the experimental techniques used throughout our study: scanning electron microscopy, and atomic force microscopy, starting with the general operating principles. We specifically focus on the two AFM-based techniques used for nanomechanical measurement: force curve mapping and dynamical friction, the latter requiring the development of a piezo-stage for mechanical excitation. Subsequently, a brief description of the contact angle and pyroelectric setup is discussed. Our results are presented in chapter 4 demonstrating the clustering of regions with varying Young modulus and the proof of concept of the dynamic friction techniques on snake scales. To complete this study, we show the measure of the water contact angle with snake sheds, showing the hydrophobicity of the structures, and we try a measure of the pyroelectric coefficient of the scales. Finally, we conclude and provide an outlook to this study in chapter 5.

additional functionalities they confer. In particular, micrometre-scale surface structures in both animals and plants promote superhydrophobicity [12], and have been used as models for superomniphobic biomimetic materials [13]. The microstructures can also act as photonic crystals, giving rise to the iridescence observed in certain snake species [14].

Since our work focuses specifically on the mechanical properties of the microstructures, we generally do not address these additional functionalities, except for some basic wettability measurement to assess the comparative hydrophobicity of different structures.

# 2 Theoretical concepts

## 2.1 | Elasticity

The theory of elasticity explains how a material reversibly deforms under an applied force. In the language of elasticity theory, strain (applied force) is linked to stress (deformation) by Hooke's law. In this brief review of its key aspects, the formal definition of the strain and stress tensors is mainly based on the work of Landau & Lifchitz [15], and the Hertz model development uses the simplification from Johnson [16], but with the notation of Landau & Lifchitz.

### 2.1.1 Strain tensor and displacement

The position of each point in a solid when it is at rest is defined by the radius vector $\mathbf{r} = (x_1, x_2, x_3)$. Under deformation, the points move to positions defined by the vector $\mathbf{r}' = (x'_1, x'_2, x'_3)$. The displacement vector is the difference between the two, $u_i = x_i - x'_i$. We can define a radius vector between two points of the solid, $\mathrm{d}x_i$, which after the deformation will have the form $\mathrm{d}x'_i = \mathrm{d}x_i + \mathrm{d}u_i$ (see Fig. 2.1).

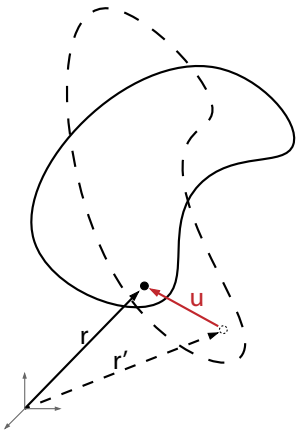


**Figure 2.1** – Schematic representation of a generic deformation. The solid and dashed lines represent the shape of the object before and after deformation, respectively. Positions of the points in the solid are defined by the vector $\mathbf{r}$. The new positions after deformation are defined by $\mathbf{r}'$. The displacement is quantified by the vector $\mathbf{u}$.

From there, the scalar distance between two points before and after the deformation, respectively, can be defined as :

$$\begin{aligned} \mathrm{d}l &= \sqrt{\mathrm{d}x_1^2 + \mathrm{d}x_2^2 + \mathrm{d}x_3^2} \\ \mathrm{d}l' &= \sqrt{\mathrm{d}x_1'^2 + \mathrm{d}x_2'^2 + \mathrm{d}x_3'^2} \end{aligned} \tag{2.1}$$

This expression can also be written as $\mathrm{d}l'^2 = \sum_i (\mathrm{d}x_i + \mathrm{d}u_i)^2$. By using the definition of total derivative, $\mathrm{d}u_i = \sum_k \frac{\partial u_i}{\partial x_k} \mathrm{d}x_k$, the deformed length can thus be expressed as:

$$\mathrm{d}l'^2 = \mathrm{d}l^2 + 2\sum_{k,i} \frac{\partial u_i}{\partial x_k}\,\mathrm{d}x_i\,\mathrm{d}x_k + \sum_{k,i,l} \frac{\partial u_i}{\partial x_k}\frac{\partial u_i}{\partial x_l}\,\mathrm{d}x_k\,\mathrm{d}x_l \tag{2.2}$$

The second term of equation (2.2) can be symmetrized by splitting the sum:

$$\sum_{k,i} 2\frac{\partial u_i}{\partial x_k}\,\mathrm{d}x_i\,\mathrm{d}x_k = \sum_{k,i} \frac{\partial u_k}{\partial x_i}\,\mathrm{d}x_k\,\mathrm{d}x_i + \sum_{k,i} \frac{\partial u_i}{\partial x_k}\,\mathrm{d}x_i \tag{2.3}$$

The suffixes $i$ and $l$ in the last term can be interchanged, leading to the equation:

$$\mathrm{d}l'^2 = \mathrm{d}l^2 + \sum_{k,i} \left( \frac{\partial u_i}{\partial x_k} + \frac{\partial u_k}{\partial x_i} + \sum_l \frac{\partial u_l}{\partial x_k}\frac{\partial u_l}{\partial x_i} \right) \mathrm{d}x_k\,\mathrm{d}x_i \tag{2.4}$$

From this, the strain tensor is defined as:

$$u_{ik} = \frac{1}{2}\left( \frac{\partial u_i}{\partial x_k} + \frac{\partial u_k}{\partial x_i} + \sum_l \frac{\partial u_l}{\partial x_k}\frac{\partial u_l}{\partial x_i} \right) \tag{2.5}$$

leading to the more compact formulation of the distance after deformation:

$$\mathrm{d}l'^2 = \mathrm{d}l^2 + 2\sum_{ik} u_{ik}\,\mathrm{d}x_i\,\mathrm{d}x_k \tag{2.6}$$

In this form, the deformation tensor is obviously symmetric, $u_{ik} = u_{ki}$.

$$u_{ik} = \begin{pmatrix} \frac{\partial u_1}{\partial x_1} + \frac{1}{2}\sum_m \left(\frac{\partial u_m}{\partial x_1}\right)^2 & \frac{1}{2}\left(\frac{\partial u_2}{\partial x_1} + \frac{\partial u_1}{\partial x_2} + \sum_m \frac{\partial u_m}{\partial x_1}\frac{\partial u_m}{\partial x_2}\right) & \frac{1}{2}\left(\frac{\partial u_3}{\partial x_1} + \frac{\partial u_1}{\partial x_3} + \sum_m \frac{\partial u_m}{\partial x_1}\frac{\partial u_m}{\partial x_3}\right) \\ \frac{1}{2}\left(\frac{\partial u_2}{\partial x_1} + \frac{\partial u_1}{\partial x_2} + \sum_m \frac{\partial u_m}{\partial x_1}\frac{\partial u_m}{\partial x_2}\right) & \frac{\partial u_2}{\partial x_2} + \frac{1}{2}\sum_m \left(\frac{\partial u_m}{\partial x_2}\right)^2 & \frac{1}{2}\left(\frac{\partial u_3}{\partial x_2} + \frac{\partial u_2}{\partial x_3} + \sum_m \frac{\partial u_m}{\partial x_2}\frac{\partial u_m}{\partial x_3}\right) \\ \frac{1}{2}\left(\frac{\partial u_3}{\partial x_1} + \frac{\partial u_1}{\partial x_3} + \sum_m \frac{\partial u_m}{\partial x_1}\frac{\partial u_m}{\partial x_3}\right) & \frac{1}{2}\left(\frac{\partial u_3}{\partial x_2} + \frac{\partial u_2}{\partial x_3} + \sum_m \frac{\partial u_m}{\partial x_2}\frac{\partial u_m}{\partial x_3}\right) & \frac{\partial u_3}{\partial x_3} + \frac{1}{2}\sum_m \left(\frac{\partial u_m}{\partial x_3}\right)^2 \end{pmatrix} \tag{2.7}$$

This allows diagonalization at any given point in the solid. It should be noted that the resulting strain tensor will only be diagonal at the specific point, and not necessarily elsewhere. After diagonalization and by using the definition of $\mathrm{d}l$ from equation (2.1), we arrive to the form:

$$\mathrm{d}l'^2 = \sum_i (1 + 2u^{(i)})\,\mathrm{d}x_i^2 \tag{2.8}$$

where $u^{(i)}$ are the eigenvalues. We can rewrite the radius vector after deformation as $\mathrm{d}x_i' = \sqrt{1 + 2u^{(1)}}\,\mathrm{d}x_1$. As it only depends on the radius vector at rest and the eigenvalues of the strain tensor, the strain tensor fully describes the deformation of the system. Except for some particular cases, a small deformation leads to a small tensor eigenvalues, allowing a Taylor expansion to be performed on the square root, leading to the following expression of the relative displacement:

$$\frac{\mathrm{d}x_i' - \mathrm{d}x_i}{\mathrm{d}x_i} = u^{(1)} \tag{2.9}$$

The volume after deformation can be written as : $\mathrm{d}V' = \mathrm{d}V \prod_i (1 + u^{(i)})$. Since we assume small deformations, the expression can be simplified further by taking only the leading order[1]:

$$\mathrm{d}V' = \mathrm{d}V(1 + \sum_i u_{ii}) \tag{2.10}$$

This lead us to conclude that the relative variation of volume of the solid is simply the sum of the diagonal elements of the strain tensor: $\frac{\mathrm{d}V' - \mathrm{d}V}{\mathrm{d}V} = \sum_i u_{ii}$.

[1] We use the fact that the sum of the diagonal elements of a tensor is invariant, meaning that we can sum over $u_{ii}$ instead of summing the eigenvalues.

### 2.1.2 Stress tensor

When a body is not deformed, it is at mechanical equilibrium: the net force on any part of the object is zero. Deformation of the solid will give rise to stresses, internal forces that do not compensate each other. The total force acting on the system can be defined as $\int \mathbf{F}\,\mathrm{d}V$, where $\mathbf{F}$ is the force per unit of volume and $\mathrm{d}V$ the infinitesimal volume element. As the internal forces inside the volume element $\mathrm{d}V$ must cancel out due to Newton's third law, the only forces contributing to stresses are those acting on the surface of $\mathrm{d}V$. Thus, it is possible to use the divergence theorem to express the integral over the surface instead of the volume. To do so, we define $\sigma_{ik}$, a rank two tensor called the stress tensor, such that :

$$F_i = \sum_k \frac{\partial \sigma_{ik}}{\partial x_k} \tag{2.11}$$

The applied force can then be rewritten as an integral over the surface, with $\mathrm{d}A_i$ as the components of the vector normal to the surface of the volume $\mathrm{d}V$:

$$\int F_i \,\mathrm{d}V = \int \sum_k \frac{\partial \sigma_{ik}}{\partial x_k}\,\mathrm{d}V = \oint \sum_i \sigma_{ik}\,\mathrm{d}A_i \tag{2.12}$$

It should be noted that in the above calculation, $F_i$ is the force applied on the volume element $\mathrm{d}V$. Thus, the force applied by the volume element to its surrounding has the opposite sign, and moreover the stress tensor is symmetric.

In the absence of external forces, the body is at equilibrium and the internal forces must cancel out, such that: $\sum_k \frac{\partial \sigma_{ik}}{\partial x_k} = 0$. Under application of an external pressure $\mathbf{P}$, the resulting force on a surface $\mathrm{d}A$ is $\mathbf{P}\,\mathrm{d}A$, and obey the following equilibrium condition:

$$P_i \,\mathrm{d}A = \sum_k \sigma_{ik}\,\mathrm{d}A_k \tag{2.13}$$

Using $\mathrm{d}A_k = n_k\,\mathrm{d}A$, where $n_k$ is the k-component of the vector $\hat{n}$ is the unit vector pointing out of the surface, the above condition can be rewritten as:

$$\sum_k \sigma_{ik} n_k = P_i \tag{2.14}$$

This equation describes the boundary conditions for the surface of a body at equilibrium, and thus links the stress to applied external forces.

### 2.1.3 Thermodynamic relations

It is possible to link the stress and strain tensors by using the definition of Helmholtz free energy (derived from the first law of thermodynamics):

$$\mathrm{d}F = -S\,\mathrm{d}T - \mathrm{d}W \tag{2.15}$$

where $\mathrm{d}F$ is the variation of free energy, $\mathrm{d}T$ the variation of temperature, $S$ the entropy and $\mathrm{d}W$ the infinitesimal work. The idea behind the following derivation is to express the work by using the previously defined tensors. First, work by unit volume $\delta W = \sum_i F_i\,\mathrm{d}u_i$, where $u_i$ is the component of the displacement vector, is integrated over the volume $\mathrm{d}V$:

$$\int \delta W\,\mathrm{d}V = \int \sum_{ik} \frac{\partial \sigma_{ik}}{\partial x_k} \delta u_i\,\mathrm{d}V \tag{2.16}$$

The right side can then be integrated by parts:

$$\int \sum_{ik} \frac{\partial \sigma_{ik}}{\partial x_k} \delta u_i\,\mathrm{d}V = \sum_{ik} \left[ \oint \sigma_{ik} \delta u_i\,\mathrm{d}A_k - \int \sigma_{ik} \frac{\partial \delta u_i}{\partial x_k}\,\mathrm{d}V \right] \tag{2.17}$$

In the case of an infinite medium, the surface contour can be taken arbitrarily as large as possible, leading to an absence of surface deformation. The stress tensor is zero on this surface and therefore the surface integral cancels out. The second integral can be symmetrized and the strain tensor factored:

$$\begin{aligned}\int \delta W \, \mathrm{d}V &= -\frac{1}{2} \sum_{ik} \int \sigma_{ik} \left( \frac{\partial \delta u_i}{\partial x_k} + \frac{\partial \delta u_k}{\partial x_i} \right) \mathrm{d}V \\ &= -\frac{1}{2} \sum_{ik} \int \sigma_{ik} \delta \left( \frac{\partial u_i}{\partial x_k} + \frac{\partial u_k}{\partial x_i} \right) \mathrm{d}V\end{aligned} \tag{2.18}$$

Here, we assume that the displacement is small, by using Eq. 2.5 and keeping only the linear terms of the strain tensor :

$$\int \delta W = -\sum_{ik} \int \sigma_{ik} \delta u_{ik} \, \mathrm{d}V \tag{2.19}$$

As such the work becomes:

$$\delta W = -\sum_{ik} \sigma_{ik} \delta u_{ik} \tag{2.20}$$

If we assume that the deformation is adiabatic, it is thermodynamically reversible, and therefore we can write $\delta \to \mathrm{d}$ . As such the free energy becomes:

$$\mathrm{d}F = -S \, \mathrm{d}T + \sum_{ik} \sigma_{ik} \, \mathrm{d}u_{ik} \tag{2.21}$$

From there we can obtain the components of the stress tensor by differentiating the free energy with respect to the components of the strain tensor:

$$\sigma_{ik} = \left( \frac{\partial F}{\partial u_{ik}} \right)_T \tag{2.22}$$

### 2.1.4 Hooke's law

In order to link the two tensors using equation (2.22), it is necessary to express the free energy in terms of the strain tensor. To do so, we will expand the free energy as a Taylor series of the strain tensor components. Due to adiabatic conditions, the first-order term is zero. Additionally, since the free energy is a scalar, it is necessary to create scalars from the components of the second rank strain tensor. This leads to the following expansion of the free energy:

$$F = F_0 + \frac{\lambda}{2} \left( \sum_i u_{ii} \right)^2 + \mu \sum_{i,k} u_{ik}^2 \tag{2.23}$$

The free energy can be separated into two terms, one corresponding to a pure hydrostatic compression, the other to a pure shear deformation (see appendix 6.1 for the details of the development), with $K = \lambda + \frac{2}{3}\mu$ the bulk modulus, and $\mu$ the shear modulus:

$$F = F_0 + \mu \sum_{ik} \left( u_{ik} - \frac{1}{3} \delta_{ik} \sum_l u_{ll} \right)^2 + \frac{K}{2} \left( \sum_l u_{ll} \right)^2 \tag{2.24}$$

Now that the free energy is expressed using the components of the strain tensor, we can use equation (2.22) to link stress and strain. Under the assumption that the temperature is constant, $\frac{\mathrm{d}F}{\mathrm{d}u_{ik}} = \frac{\partial F}{\partial u_{ik}}$, and thus the total differential $\mathrm{d}F$ can be computed:

$$
\begin{aligned}
\mathrm{d}F &= \frac{K}{2}\sum_{ik}\frac{\partial\left(\sum_l u_{ll}\right)^2}{\partial u_{ik}}\,\mathrm{d}u_{ik} + \mu\sum_{ik}\frac{\partial\left[\left(u_{ik}-\frac{1}{3}\delta_{ik}\sum_l u_{ll}\right)^2\right]}{\partial\left(u_{ik}-\frac{1}{3}\delta_{ik}\sum_l u_{ll}\right)}\,\mathrm{d}\left(u_{ik}-\frac{1}{3}\delta_{ik}\sum_l u_{ll}\right)\\
&= K\sum_l u_{ll}\,\mathrm{d}u_{ll} + 2\mu\sum_{ik}\left(u_{ik}-\frac{1}{3}\delta_{ik}\sum_l u_{ll}\right)\mathrm{d}\left(u_{ik}-\frac{1}{3}\delta_{ik}\sum_l u_{ll}\right)\\
&= K\sum_l u_{ll}\,\mathrm{d}u_{ll} + 2\mu\sum_{ik}\left[u_{ik}\,\mathrm{d}u_{ik} - \sum_l\left(\frac{1}{3}u_{ll}\delta_{ik}\,\mathrm{d}u_{ik} - \frac{1}{3}\delta_{ik}u_{ik}\,\mathrm{d}u_{ll} + \frac{1}{9}\delta_{ik}u_{ll}\,\mathrm{d}u_{ll}\right)\right]\\
&= K\sum_l u_{ll}\,\mathrm{d}u_{ll} + 2\mu\sum_{ik}\left[u_{ik}-\delta_{ik}\sum_l\frac{1}{3}u_{ll}\right]\mathrm{d}u_{ik} - \frac{1}{3}\sum_{ikl}\delta_{ik}u_{ik}\,\mathrm{d}u_{ll} + \frac{1}{9}\sum_{ikl}\delta_{ik}u_{ll}\,\mathrm{d}u_{ll}\\
&= K\sum_l u_{ll}\,\mathrm{d}u_{ll} + 2\mu\sum_{ik}\left[u_{ik}-\delta_{ik}\sum_l\frac{1}{3}u_{ll}\right]\mathrm{d}u_{ik} + \sum_l\underbrace{\left[\frac{-1}{3}u_{ll}\,\mathrm{d}u_{ll} + \frac{3}{9}u_{ll}\,\mathrm{d}u_{ll}\right]}_{=0}\\
\mathrm{d}F &= \sum_{ik}\left[K\delta_{ik}\sum_l u_{ll} + 2\mu\left(u_{ik}-\delta_{ik}\sum_l\frac{1}{3}u_{ll}\right)\right]\mathrm{d}u_{ik}
\end{aligned}
\tag{2.25}
$$

The relation between strain and stress follows from equation (2.22):

$$\sigma_{ik} = K\sum_l u_{ll}\delta_{ik} + 2\mu\left(u_{ik}-\frac{1}{3}\delta_{ik}\sum_l u_{ll}\right) \tag{2.26}$$

In order to reverse this equation we compute the sum $\sum_i \sigma_{ii}$:

$$
\begin{aligned}
\sum_l \sigma_{ll} &= 3K\sum_l u_{ll}\\
\sum_l u_{ll} &= \frac{1}{3K}\sum_l \sigma_{ll}
\end{aligned}
\tag{2.27}
$$

Equation (2.27) can then be inserted into (2.26), to obtain the inverse relation:

$$\sigma_{ik} = \frac{1}{3}\delta_{ik}\sum_l\sigma_{ll} + 2\mu u_{ik} - \frac{2\mu}{9K}\delta_{ik}\sum_l u_{ll} \tag{2.28}$$

We can now isolate $u_{ik}$, and we obtain Hooke's law:

$$u_{ik} = \frac{1}{2\mu}\sigma_{ik} - \frac{1}{6\mu}\delta_{ik}\sum_l\sigma_{ll} + \frac{1}{9K}\delta_{ik}\sum_l u_{ll} \tag{2.29}$$

### 2.1.5 Young and Shear Modulus

One example of the application of the Hooke's law can be found in the description of a homogeneous deformation of a rod. In this case, a perpendicular force is applied to one end, such that the rod compresses/expands.

We suppose that the rod is positioned along the z axis as shown in Fig 2.2. Since the deformation is homogeneous, $u_{ik}$ and $\sigma_{ik}$ are constants. The latter can be defined by the the boundary conditions (2.14). In this simple case, the force is applied to the surface perpendicular to $\mathbf{z}$, such that only $\sigma_{zz}$ is non-zero: $\sigma_{zz} = p$, where p is the applied pressure. Applying Hooke's law (2.29) to this particular case, we find:

$$u_{ik} = \frac{1}{2\mu}\sigma_{ik} - \frac{1}{6\mu}\delta_{ik}\sigma_{zz} + \frac{1}{9K}\delta_{ik}\sigma_{zz} \tag{2.30}$$

From the above, we can see that $u_{ik} = 0$ where $i \neq k$, and is non-zero only where $i = k$:

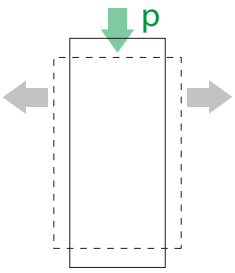


**Figure 2.2** – Schematic representation of the rod deformation under applied pressure $p$. The solid and dashed lines correspond to the rod before and after deformation, respectively. Due to the application of pressure the rod is compressed along the **z** axis. By conservation of the mass, the rod expands radially.

$$\begin{aligned} u_{xx} = u_{yy} &= \left(\frac{1}{9K} - \frac{1}{6\mu}\right) p \\ u_{zz} &= \left(\frac{1}{9K} + \frac{1}{3\mu}\right) p \end{aligned} \tag{2.31}$$

We can rewrite $u_{zz}$ as:

$$u_{zz} = \frac{p}{E} \tag{2.32}$$

$$E = \frac{9K\mu}{3K + \mu} \tag{2.33}$$

With the Young modulus $E$ which links the expansion of the rod $u_{zz}$, to the applied pressure $p$. The $u_{xx}$ and $u_{yy}$ components correspond to the lateral compression of the rod as it expands along z. The relation between the expansion and compression can be expressed as:

$$u_{xx} = -\sigma u_{zz} \tag{2.34}$$

Here, $\sigma$ is the Poisson coefficient:

$$\sigma = \frac{1}{2}\frac{3K - 2\mu}{3K + \mu} \tag{2.35}$$

### 2.1.6 Hertz Model

In our study, we extract the Young modulus of the probed material, by pressing on it with the tip of an AFM. Hertz first developed the theory of the contact behaviour between two elastic bodies [17]. When two surfaces approach each other, they first enter in contact at a single point, but as they get closer and start to press into each other, the contact surface becomes elliptic. In the case of an AFM tip in contact with the sample surface, we assume that the end of the tip is a sphere and the surface is flat. As a result, the ellipse becomes a circle, simplifying the calculations considerably. We define the xy plane as the plane perpendicular to the point of contact of the two bodies, and the z axis is perpendicular to this plane. The surface of the sphere of radius $R$ is defined as:

$$z_1 = \frac{1}{2R}\left(x^2 + y^2\right) \tag{2.36}$$

Additionally, the surface of the sample is considered flat, such that $z_2 = 0$.

As the bodies are brought into contact for a distance $\delta$ beyond the point of initial contact, they respectively deform by $u_{z1}$ and $u_{z2}$ (see Fig. 2.3), such that:

$$\delta = \frac{1}{2R}r^2 + u_{z1} + u_{z2} \tag{2.37}$$

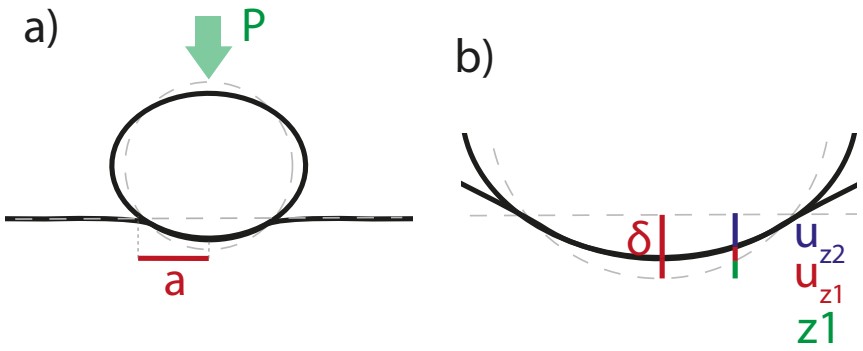


**Figure 2.3** – Deformation of a flat surface due to indentation by a sphere. Dashed lines correspond to the position of the sphere and flat surface in the absence of deformation, $a$ is the contact area radius, $\delta$ is the distance beyond the initial point of contact, $u_{zi}$ are the deformations of the two mediums, and $z1$ is the position of the point on the sphere.

with $r = \sqrt{x^2 + y^2}$ expressed in polar coordinates due to the rotational symmetry of our system.

It is shown that the pressure in this configuration has the form: $p = p_0 \left(1 - \frac{r^2}{a^2}\right)^{1/2}$ [16]. In the simple case where the pressure only depends on z, finding the displacement is trivial, since $u_{zz} = \frac{\partial u_z}{\partial z}$, and in the case of homogeneous deformation we have $u_{zz} = \frac{p}{E}$ leading to:

$$u_z = \frac{1}{E} \int_0^{z_m} p(z)\, \mathrm{d}z \tag{2.38}$$

However, in the case of a circular area of contact, the problem is a lot more complex, since, surprisingly, the radial coordinates are not the natural ones for the problem, and we have the following relation:

$$u_z = \frac{1 - \sigma^2}{\pi E} \int_S p(s, \phi)\, \mathrm{d}\phi\, \mathrm{d}s \tag{2.39}$$

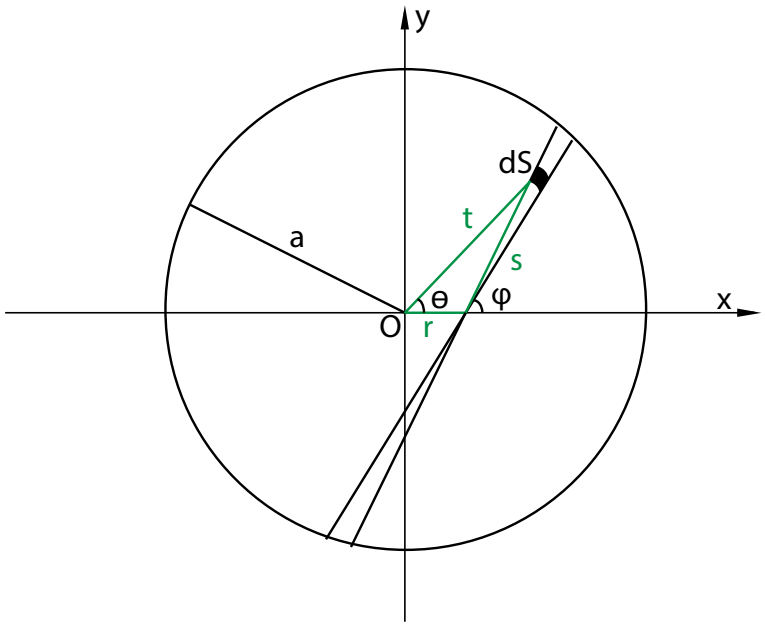


**Figure 2.4** – Definition of the change of variables for the integral over the contact area in the Hertz model. Based on a figure in *Contact Mechanics* [16]

where $s$ and $\phi$ are defined as shown in Fig. 2.4. Using the cosine rule $t^2 = r^2 + s^2 - 2rs\cos(\phi)$, the pressure becomes $p(s,\phi) = \frac{p_0}{a}(\alpha^2 - 2\beta s - s)^{1/2}$, with $\alpha^2 = a^2 - r^2$ and $\beta = r\cos(\phi)$. Finally we can rewrite this integral into a solvable form:

$$u_z = \frac{1-\sigma^2}{\pi E}\frac{p_0}{a}\int_0^{2\pi}\int_0^{s_1}(\alpha^2 - 2\beta s - s^2)^{1/2}\,\mathrm{d}\phi\,\mathrm{d}s \tag{2.40}$$

where $s_1$ is the positive root of $\alpha^2 - 2\beta s - s^2 = 0$.
The integration over $s$ yields:

$$\int_0^{s_1}(\alpha^2 - 2\beta s - s^2)^{1/2}\,\mathrm{d}s = \frac{1}{2}\alpha\beta + \frac{1}{2}\left(\alpha^2 + \beta^2\right)\left[\frac{\pi}{2} - \tan^{-1}\left(\frac{\beta}{\alpha}\right)\right] \tag{2.41}$$

Since $\beta \propto \cos(\phi)$, the integration over $[0, 2\pi]$ cancels this term and we are left with:

$$u_z = \frac{1-\sigma^2}{\pi E}\frac{p_0}{a}\int_0^{2\pi}\frac{\pi}{4}\left(a^2 - r^2 + r^2\cos^2(\phi)\right)\mathrm{d}\phi \tag{2.42}$$

finally leading to the expression of $u_z(r)$, which is only valid inside the area of contact, for $r \leq a$:

$$u_{z1}(r) = \frac{1-\nu_1^2}{E_1}\frac{\pi p_0}{4a}(2a^2 - r^2) \tag{2.43}$$

The equation for $u_{z2}$ is similar and can be obtained by substituting: $1 \leftrightarrow 2$, meaning that it is thus useful to define an effective modulus such as $\frac{1}{E^*} = \frac{1-\nu_1^2}{E_1} + \frac{1-\nu_2^2}{E_2}$. This solution can be inserted into equation (2.37):

$$\delta = \frac{1}{2R}r^2 + \frac{\pi p_0}{4aE^*}(2a^2 - r^2) \tag{2.44}$$

The above equation holds true for any value of $r$, and by taking $r = 0$, the value of $\delta$ can be obtained:

$$\delta = \frac{\pi a p_0}{2E^*} \tag{2.45}$$

The value for $a$ can be computed by inserting $\delta$ into the equation at any value of $r \neq 0$:

$$a = \frac{\pi p_0 R}{2E^*} \tag{2.46}$$

With these, the pressure $p_0$ can be linked to the applied force $P$, given that the applied force is the sum of the pressure over an area of radius $a$:

$$P = \int_0^a p(r)2\pi r\,\mathrm{d}r = \frac{2}{3}\pi a^2 p_0 \tag{2.47}$$

This finally yields the main result of the Hertz model: the relation between the displacement $\delta$ and the applied force $F$:

$$\delta = \left(\frac{9P^2}{16RE^{*2}}\right)^{1/3} \tag{2.48}$$

In the case of an AFM tip, the displacement is approximated by the deflection of the cantilever, allowing us to measure the Young modulus by performing force curves. To do so, we need to know the Young modulus and Poisson coefficient of the tip. These parameters are calibrated inside the software of the AFM. We also need to know the contact area, which is extracted from the nominal value of the tip radius. Unfortunately, it is well known that the sharpness of the tip deteriorates during measurement, leading to a slight variation of the tip radius. However, as shown in chapter 4.2.1, this effect does not seem to affect our measurements drastically. Additionally, the model assumes a flat substrate, which is not the case in most of our samples: the height heterogeneity of the snake scales leads to a variation of the contact surface, which in turn leads to a variation of the calculated Young modulus of the tip, especially at the edges of images structures.

## 2.2 | Tribology — Friction

Tribology describes the contact interaction between two objects as they are moving across each other. It is a vast domain studied in engineering, due to its importance in industrial applications. In this chapter, we look into the concept of friction, the force which appears to oppose the movement of an object on a solid. Here, we will focus on the interaction between two solid bodies in contact with each other.

The usual formal definition of friction is:

$$F_s = \mu_s F_N \tag{2.49}$$

where $\mathbf{F_s}$ is the static friction force, $\mu_s$ the coefficient of static friction and $\mathbf{F_N}$ the normal force. When the applied force is sufficient to overcome the static friction, the object will start to move. From there it does not disappear but instead becomes the dynamic friction $\mathbf{F_R}$, and with $\mu_k$ instead of $\mu_s$, the dynamic friction coefficient. Contrary to popular belief, the friction coefficient does not seem to depend on the surface roughness. [18] Nevertheless, the first theory of dry friction by Coulomb used roughness as an explanation for friction. If we observe a point-mass on a corrugated surface, locally it is situated on a tilted plane. (see Fig. 2.5). $\mathbf{F_N}$ is the force by the gravity, and $\mathbf{F}$ is the applied force to make the system move. For a low value of $\mathbf{F}$, the system is at equilibrium, leading to:

$$F = F_N \tan(\theta) \tag{2.50}$$

Where $\theta$ is the angle of the inclined plane. As long as the system is at equilibrium, this equation holds and therefore the static friction force is given by the maximal value of $F$, such that:

$$F_S = F_M = F_N \tan(\theta_M) \tag{2.51}$$

leading to the definition of the friction coefficient:

$$\mu_s = \tan(\theta_M) \tag{2.52}$$

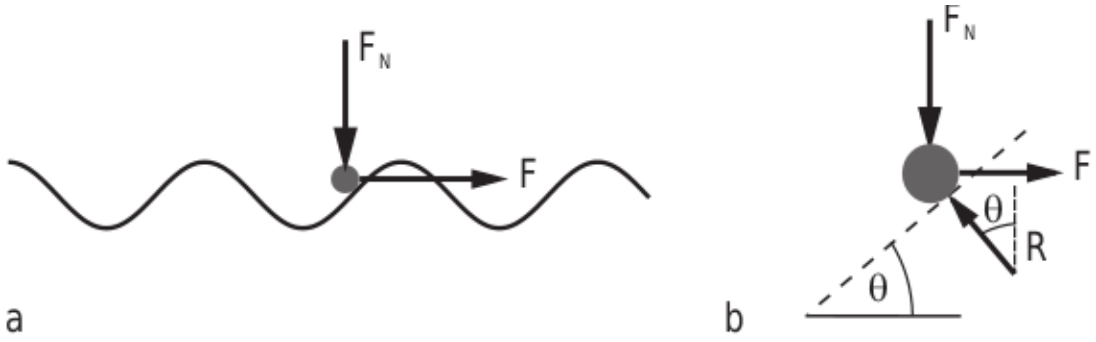


**Figure 2.5** – Schematic of Coulomb's friction model [18]. $\mathbf{F_N}$ is the normal force due to gravity and $\mathbf{F}$ is the driving force. As long as the system is at equilibrium, the sum of these two forces is compensated by the force $\mathbf{R}$.

This theory explains in details the behaviour of friction between solids, but not the non-dependency of the friction coefficient on the surface roughness. In 1949, Bowden and Tabor proposed a theory using a microscopical explanation [19]: when two bodies are in contact, due to asperities, the atoms of some of their regions are brought very close and are in "contact", while other are sufficiently far away to not interact. It is only this surface of contact (the real area of contact $A_R$) which determines the frictional properties between the two solids $F_F \propto A_R$. Moreover, the contact surface depends on the applied force, since under an applied pressure the two bodies will deform (see Chap.2.1), and thus increase the area of contact.

$$F_F = \sigma A_R \tag{2.53}$$

where $F_f$ is the friction force and $\sigma$ is the shear strength. While its properties are not well known, we can assume that it depends linearly on the pressure $P$, such that $\sigma = \sigma_0 + \alpha P$, and therefore:

$$F_F = \sigma A_R = (\sigma_0 + \alpha P) A_R \tag{2.54}$$

$$F_F = \sigma_0 A_R + \alpha F_N \tag{2.55}$$

In the case where the applied pressure is large ($P \gg \sigma_0$), we recover the macroscopic law of friction:

$$F_F = \alpha F_N \tag{2.56}$$

The study of friction and its anisotropy on snake scales is essential for a deeper understanding of snake locomotion, and especially of the stick-to-slip transition - the passage from static to dynamic friction - which would explain how the snake is able to slide in a defined direction.

## 2.3 | Water interaction with surfaces

The theory of the formation of droplets on substrates is a complex subject, inscribing itself in the broader theory of pinned elastic interfaces [20]. The models described below are large simplifications which present some flaws but are sufficient for the succinct study presented here.

### 2.3.1 The Wenzel and the Cassie-Baxter models

This theoretical part is mostly based on the work of De Gennes, Brochard-Wyart and Quere [21]. The work of Law and Zhao [22] was used to emphasize the difficulty of reproducible measurements of the contact angle.

A liquid is a state where molecules are mobile but maintain strong nearest neighbour interaction. This coupling leads to the presence of cohesive energy between neighbours, $-U$. In an infinite medium, all the particles have roughly the same number of neighbours. However, as can be seen in Fig. 2.6, if an interface is present, the number of neighbours at its location is roughly half of that of the bulk, meaning that the cohesive energy would only be approximately $\frac{-U}{2}$, making the interface energetically unfavourable. Therefore, the system tries to minimize the area of the interface.

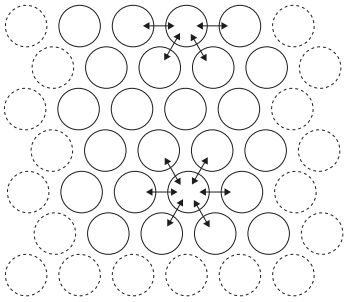

**Figure 2.6** – Schematic representation of the nearest-neighbour interaction. At the interface, the number of neighbours is roughly half the one in bulk, leading to a lower cohesive energy at the surface.

The surface tension $\gamma$ is the energy loss per unit area due to the interface formation, therefore for a molecule of size $a$, the surface tension is roughly[2]:

$$\gamma = \frac{U}{2a} \tag{2.57}$$

To increase the size of the interface by a surface $\mathrm{d}A$, some work $\mathrm{d}W$ needs to be applied to the system. Since the interface formation energy by unit area is $\gamma$, the work required is:

$$\mathrm{d}W = \gamma \, \mathrm{d}A \tag{2.58}$$

In our case, three phases coexist inside the system: the substrate, the water and the air. Such a configuration allows for two kinds of interface, either between water and substrate, or between water and air. If the energy cost of the interface is lower for the water-substrate boundary, the water will try to maximize its contact area with the surface by wetting it totally. Otherwise, an equilibrium will form and the water will take the shape of a drop, with an angle of contact $\theta_E$ between the substrate and water. This behaviour can be described by the spreading parameter $S$, defined as:

$$S = \gamma_{SG} - (\gamma_{SL} + \gamma_{LG}) \tag{2.59}$$

Where $S, G$ and $L$ stand for solid, liquid and gas, and $\gamma_{XY}$ is the surface tension between the corresponding $X$ and $Y$.

When $S > 0$, we have a total wetting of the sample ($\theta_E = 0$). Otherwise, we have partial wetting, with an angle of contact $\theta_E$. For an angle $\theta_E > \frac{\pi}{2}$, the surface is hydrophobic and for $\theta_E < \frac{\pi}{2}$ it is hydrophilic. The transition from hydrophobic to hydrophilic is meaningful when looking at a rough substrate.

[2] In the case of water, $\gamma \approx 72 mJ/m^2$ [21]

The contact angle can be expressed as a function of $\gamma$ by looking at the energy cost of moving the interface a small distance $\mathrm{d}x$ (see Fig. 2.7):

$$\mathrm{d}E = (\gamma_{SL} - \gamma_{SG})\,\mathrm{d}x + \gamma_{LG}\cos(\theta_E)\,\mathrm{d}x \tag{2.60}$$

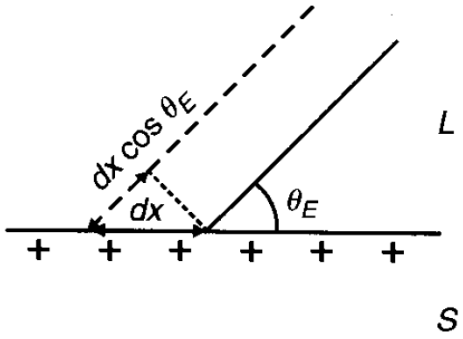


**Figure 2.7** – Moving the interface by a length $\mathrm{d}x$ requires work equivalent to the interface formation energy: $(\gamma_{SL} - \gamma_{SG})\,\mathrm{d}x$ and $\gamma_{LG}\cos(\theta_E)\,\mathrm{d}x$

At the equilibrium, $\frac{\mathrm{d}E}{\mathrm{d}x}$ must be zero, so we obtain the Young-Dupré Law:

$$\gamma_{LG}\cos(\theta_E) = \gamma_{SG} - \gamma_{SL} \tag{2.61}$$

Moreover, a droplet on a smooth surface and a droplet on a rough surface have different angles of contact, even if the two surfaces have the same composition. This angle is called the apparent angle $\theta^*$. Wenzel expanded the Young-Dupré Law to take roughness into account by assuming that the length of the solid-liquid interface when moved by $\mathrm{d}x$ is, in fact, $r\,\mathrm{d}x$ (see Fig. 2.8(a)). This leads to the **Wenzel model**, described by:

$$\mathrm{d}E = r\,(\gamma_{SL} - \gamma_{SG})\,\mathrm{d}x + \gamma_{LG}\cos(\theta^*)\,\mathrm{d}x \tag{2.62}$$

Assuming that the system is at equilibrium ($\frac{\mathrm{d}E}{\mathrm{d}x} = 0$), rearranging the terms, and inserting the Young-Dupré law (2.61) leads to:

$$\cos(\theta^*) = r\cos(\theta_E) \tag{2.63}$$

This implies that for $\theta_E > \frac{\pi}{2}$, $\theta^* > \theta_E$, and for $\theta_E < \frac{\pi}{2}$, $\theta^* < \theta_E$. Here, the distinction between hydrophobicity and hydrophilicity can be interpreted: the roughness enhances the wetting property of the material.

It should be noted that for $r > \frac{1}{\cos(\theta_E)}$, the contact angle jumps to a value of $\pi$ or 0, depending on the sign of $\cos(\theta_E)$. This behaviour is unphysical, and is due to the assumption that the layer of water in contact with the substrate follows the surface perfectly. This is not always the case: for a strongly hydrophobic material, the recesses may trap air pockets under the water droplet.

The **Cassie-Baxter model** assumes a chemically heterogeneous planar surfacem which is composed of a fraction $f$ of a chemical species, and of a fraction $f - 1$ of another species, as illustrated in Fig. 2.8(b), repeating the same calculation and moving the interface by a small distance $\mathrm{d}x$ yields:

$$\mathrm{d}E = f\left(\gamma_{SL}^{(1)} - \gamma_{SG}^{(1)}\right)\mathrm{d}x + (1-f)\left(\gamma_{SL}^{(2)} - \gamma_{SG}^{(2)}\right)\mathrm{d}x + \gamma_{LG}\cos(\theta^*)\,\mathrm{d}x \tag{2.64}$$

Where the superscript indices correspond to the two chemical species.

By the same process as that for the Wenzel model, we obtain:

$$\cos(\theta^*) = f\cos(\theta_1) + (1-f)\cos(\theta_2) \tag{2.65}$$

where $\theta_{1,2}$ are the contact angles of the corresponding surfaces.

Now let us go back to a chemically homogeneous substrate, with some roughness $r$. Assuming that the substrate is very hydrophilic, water will go into the recesses, reducing the system to a flat substrate with two chemical components: substrate and water. Due to the Laplace theorem, the contact angle of

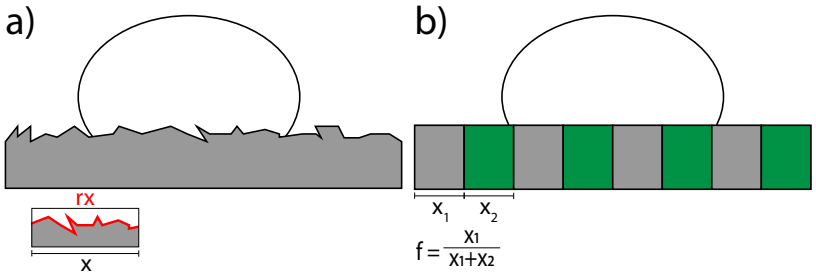


**Figure 2.8** – Schematic representation of the Wenzel (a) and Cassie-Baxter (b) models. In the Wenzel model, the roughness of the substrate changes the apparent angle. In the Cassie-Baxter model the sample is topographically smooth but presents chemical heterogeneities which change the contact angle.

water on water is $\theta_E = 0$. By applying the Cassie-Baxter model, and assuming that the fraction of holes filled with water is $(1 - f)$, we obtain:

$$\cos(\theta^*) = (1 - f) + f\cos(\theta_E) \tag{2.66}$$

The penetration of the water inside the recesses is not always given. When water goes into one of the holes, it covers a surface $r\,\mathrm{d}x$. However, the volume of water is finite and this water has to be removed from one of the flat surfaces, leaving a surface $f\,\mathrm{d}x$ dry. By looking at the energy condition of such a displacement we obtain:

$$\mathrm{d}E = (r - f)(\gamma_{SL} - \gamma_{SG})\,\mathrm{d}x + (1 - f)\gamma_{LG}\,\mathrm{d}x \tag{2.67}$$

Thus movement of the line is favourable only if it reduces the energy, $\frac{\mathrm{d}E}{\mathrm{d}x} < 0$, leading to the condition:

$$\cos(\theta_E) > \frac{1 - f}{r - f} \tag{2.68}$$

This leads to a critical angle $\theta_c$, which defines whether the water will go into the recesses or not: the equation (2.66) is valid only for $\theta_E < \theta_c$. It should be noted that $\theta_c$ is always smaller than $\frac{\pi}{2}$, meaning that the filling of holes happens only on hydrophilic materials.

Conversely, assuming that the material is hydrophobic leads to $\theta_E > \theta_C$, meaning that pockets of air form under the droplet. In the case of a planar surface, the angle of contact between air and water will be $\pi$, leading to the equation:

$$\cos(\theta^*) = f\left[\cos(\theta_E) + 1\right] - 1 \tag{2.69}$$

The critical behaviour discussed above is compiled in Fig. 2.9, with the jump in the Cassie-Baxter model corresponding to the transition through the critical angles, where water fills the air pockets. The two jumps in the Wenzel model correspond to the unphysical behaviour when $r > \frac{1}{\cos(\theta_E)}$.

### 2.3.2 Beyond Wenzel and Cassie-Baxter models

Unfortunately, the theories advanced by Wenzel, Cassie and Baxter are all defined by using the angle $\theta_E$. It has been observed that this angle does not uniquely define the contact between water and a substrate: if a drop placed on a substrate is inflated, the angle will grow up to a critical angle, the advancing angle $\theta_A$, leading to the motion of the interface. The contact area increases and the angle goes back to $\theta_E$. Conversely, for a deflating drop, the angle will decrease up to the recessing angle $\theta_R$ before motion occurs and the angle $\theta_E$ is restored. It has been shown that roughness influences these two angles. This observation means that a droplet deposited on a substrate may take any angle in the interval $[\theta_R, \theta_A]$, rendering the use of the above equations challenging [22, 23]. Another point of contention is that most of the theoretical assumptions are based on a global description of the substrate, either by the roughness $r$ or the chemical variability fraction $f$. However, it has been shown that the structure of the substrate dictates the shape of the drop only under the contact line between the three phases.

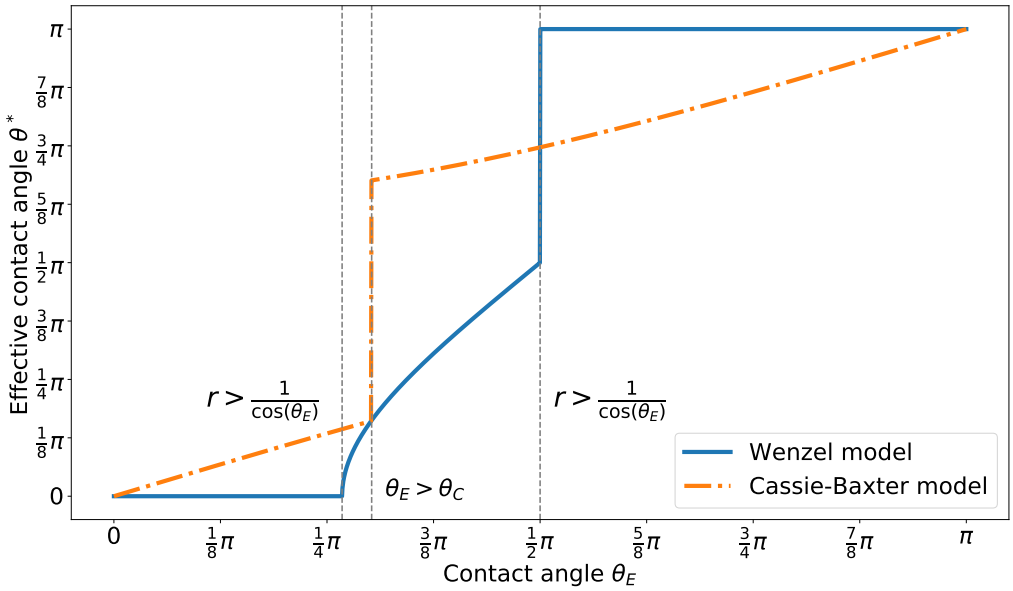


**Figure 2.9** – Calculated effective contact angle $\theta^*$ for the Wenzel and Cassie-Baxter models. In this calculation $r = 1.5$ and $f = 0.3$.

Fortunately, Meiron & al. [24] demonstrated that it is possible to recover the contact angle $\theta_E$ by applying a small vibration to the substrate at 30 to $80Hz$. This will force the droplet into a metastable state with a random angle between $\theta_A$ and $\theta_R$. Then, the energy given by the excitation allows it to quit the metastable state and to go to the "global energy minimum". In this state, it has been experimentally demonstrated on beeswax treated surfaces that the angle of contact is very similar to the one provided by Wenzel.

## 2.4 | Pyroelectricity

Pyroelectricity is a phenomenon that can appear in any crystal with non-centrosymmetric periodic arrangement. Since snake skin structures are periodic, we expect the underlying blocs to have a polarisation, which would force the keratin proteins to arrange themselves anisotropically. Thus, the measurement of the pyroelectric response of snake scales could give us information about the arrangement and properties of the keratinous sub-structure of scales. The following discussion is based on the work of Batra & Aggarwal [25].

In a dielectric material, it is possible to induce a polarisation by applying an electric field: the electric field induces a small movement of the charged particles in the material, leading to small dipolar moments $\mathbf{m_p} = q\mathbf{x}$. which sum up to a macroscopic polarisation $\mathbf{P} = \sum_i \mathbf{m_p^{(i)}}/V$. The displacement field $D$ can be defined as the resulting field due to the polarisation and the external electric field:

$$\mathbf{D} = \epsilon_0 \mathbf{E} + \mathbf{P} = \epsilon \mathbf{E} \tag{2.70}$$

In some particular dielectrics, it is also possible to induce a polarisation by deforming the material (piezoelectricity) or by varying its temperature (pyroelectricity). All pyroelectric materials are piezoelectric, and all piezoelectric materials are dielectric. In the case of pyroelectric materials, their crystalline structure is noncentrosymmetric. This leads to intrinsic dipolar moments, which give rise to a spontaneous polarisation $\mathbf{P_s}$, and add to the polarisation created by the electric field. The displacement field becomes:

$$\mathbf{D} = \epsilon \mathbf{E} + \mathbf{P_s} + \mathbf{d}\sigma \tag{2.71}$$

where $\sigma$ is the stress tensor[3], defined in section (2.1) and $\mathbf{d}$ is a piezoelectric coefficient. We will focus on the variation of the displacement field $\mathrm{d}\mathbf{D}$ along one particular axis, so that all the vector quantities become scalar:

$$\mathrm{d}D = \frac{\partial D}{\partial T}\,\mathrm{d}T + \frac{\partial D}{\partial u}\,\mathrm{d}u + \frac{\partial D}{\partial E}\,\mathrm{d}E \tag{2.72}$$

In the presence of a non-varying external electric field, the last part of the equation cancels out, and we can define the pyroelectric coefficient along the axis as:

$$p = \frac{\mathrm{d}D}{\mathrm{d}T} = \frac{\partial D}{\partial T} + \frac{\partial D}{\partial u}\frac{\mathrm{d}u}{\mathrm{d}T} \tag{2.73}$$

If we assume that the external electric field does not change with temperature, then we can define the primary pyroelectric coefficient as $p_p = \frac{\partial D}{\partial T}$, and the secondary pyroelectric coefficient as $p_s = \frac{\partial D}{\partial u}\frac{\mathrm{d}u}{\mathrm{d}T}$.

In the cases where $\frac{\partial \epsilon}{\partial T}$ is zero (which is the case for non-ferroelectric materials), the primary coefficient depends only on the spontaneous polarization:

$$p_p = \frac{\partial P_s}{\partial T} \tag{2.74}$$

The secondary coefficient corresponds to the change of polarization due to the piezoelectric effect caused by the thermal expansion of the material. The displacement of charges due to the thermal expansion can be seen as an additional polarisation $P_u$, such that $P_{tot} = P_s + P_u$, we have :

$$\begin{aligned} p = \frac{\mathrm{d}P_{tot}}{\mathrm{d}T} = \frac{\sum_i x_i}{V}\frac{\mathrm{d}q}{\mathrm{d}T} = \frac{\sum_i x_i}{V}\frac{\mathrm{d}q}{\mathrm{d}t}\frac{\mathrm{d}t}{\mathrm{d}T} \\ p\frac{\mathrm{d}T}{\mathrm{d}t} = \frac{1}{A}\frac{\mathrm{d}q}{\mathrm{d}t} \end{aligned} \tag{2.75}$$

This implies that a variation of temperature creates a current flowing through the pyroelectric material, proportional to the area $A$ and the pyroelectric coefficient:

$$I_p = Ap\frac{\mathrm{d}T}{\mathrm{d}t} \tag{2.76}$$

[3]For the purpose of this development, we assume that the property tensors are diagonal, even though it is not always the case.

# 3 Materials and methods

## 3.1 | Snake scales samples

The snake scales samples used in this study were prepared from sheds given to us by the *Vivarium de Meyrin*[1], which possesses a large variety of snakes and other reptiles kept in good conditions and provided with exemplary care. We studied a total of sixteen snakes from six families: *Elapidae* (3), *Boidae* (3), *Pythonidae* (1), *Viperidae* (5), *Dipsadinae* (1) and *Colubridae* (3). A list of all the snakes which were at least analysed with SEM are presented in Table 3.1, and a subset of the snakes featured on this study are presented in Fig. 3.1, demonstrating the large diversity of various snake species.


**Figure 3.1** – A selection of photographs of some of the snake species featured in this study.

[1]Rue du Cardinal-Journet 32A, 1217 Meyrin. Website: `http://vivariumdemeyrin.ch/`

### 3.1.1 Shed collection and conditioning

The snakes went through natural shedding in glass vivariums on substrates similar to their natural environments. The enclosures were checked daily for new sheds by the members of the vivarium. Samples in good condition were put into labelled bags and kept at ambient conditions away from light. Most of the sheds were full or almost full (head to tail), allowing us to know the position and orientation of the scales on the snake.

Samples were selected from the middle section of the snake shed. Specifically, ventral, lateral and dorsal scales from the inner and outer layers were prepared from each shed[2]. A schematic representation of the selected regions is shown in Fig. 3.2. The samples were not rehydrated since it would have added an additional layer of complexity to the measurements, and it appears that most of the previous studies keep the samples under dry conditions.

From there, a full analysis of the scale microstructures was performed by SEM. The inner part of the sheds did not show any particular features, and therefore the study was focused on the outer parts. Additionally, a large number of structures were relatively similar, and therefore the mechanical measurements were performed on samples representative nanostructures.

| Scientific Name | Common name | Family | Habitat | Continent |
|---|---|---|---|---|
| *Morelia Viridis* | Green tree python | Pythonidae | Arboreal | Oceania |
| *Naja Melanoleuca* | Black and white cobra | Elapidae | Terrestrial | Africa |
| *Naja Nivea* | Cape cobra | Elapidae | Terrestrial | Africa |
| *Naja Samarensis* | Samarensis cobra | Elapidae | Terrestrial | Asia |
| *Sanzinia Madagascariensis* | Madagascar ground boa | Boidae | Arboreal | South America |
| *Boa Constrictor* | Boa Constrictor | Boidae | Arboreal & Terrestrial | South America |
| *Corallus Hortulanus* | Amazon Tree Boa | Boidae | Arboreal | South America |
| *Bitis Arietans* | Puff Adder | Viperidae | Terrestrial | Africa |
| *Crotalus Atrox* | Western Diamondback Rattlesnake | Viperidae | Terrestrial | North America |
| *Deiangkistrodon Acutus* | Hundred-Pace viper | Viperidae | Terrestrial | Asia |
| *Protobothrops Elegans* | Spearhead | Viperidae | N/A | Asia |
| *Daboia Ruselii* | Russell's Viper | Viperidae | Terrestrial | Asia |
| *Philodyas Baroni* | Long-nosed snake | Dipasdinae | Arboreal | South America |
| *Panterophis Guttatus* | Easter cornsnake | Colubridae | Terrestrial | North America |
| *Orthriophis Taeniurus Frisei* | Stripe-tailed ratsnake | Colubridae | Terrestrial | Asia |
| *Lampropeltis Triangulum Hondurensis* | Honduran milk snake | Colubridae | Terrestrial | Central America |

**Table 3.1** – List of the studied snakes, with their families and habitat.

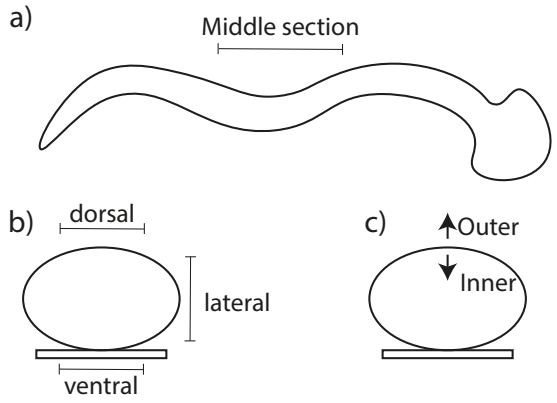


**Figure 3.2** – Schematic representation of the sample acquisition protocol. (a) The samples were taken from the middle section of the snake, (b) from the ventral, lateral and dorsal parts, (c) both from the inner and outer layers of the shed.

The initial project workflow idea is presented in Fig. 3.3. First, the sheds are acquired from the *Vivarium de Meyrin* and basic information about them is recorded within a metadata file. From there, global characterisation is performed by scanning electron microscopy (SEM) after gold sputtering of

[2]During moulting, the shed is turned inside-out, meaning that the outer layer is inside the shed. The atomic force microscopy (AFM) measurements were only done on the outer layer, which is in contact with the ground during locomotion.

the samples to avoid charge accumulation during imaging. This enables us to have a large view of the microstructures and their evolution along the scales. From there, topography and physical properties are measured at the nanoscale by AFM. Additionally, some scales were also subjected to wetting properties and pyroelectric coefficient measurements.

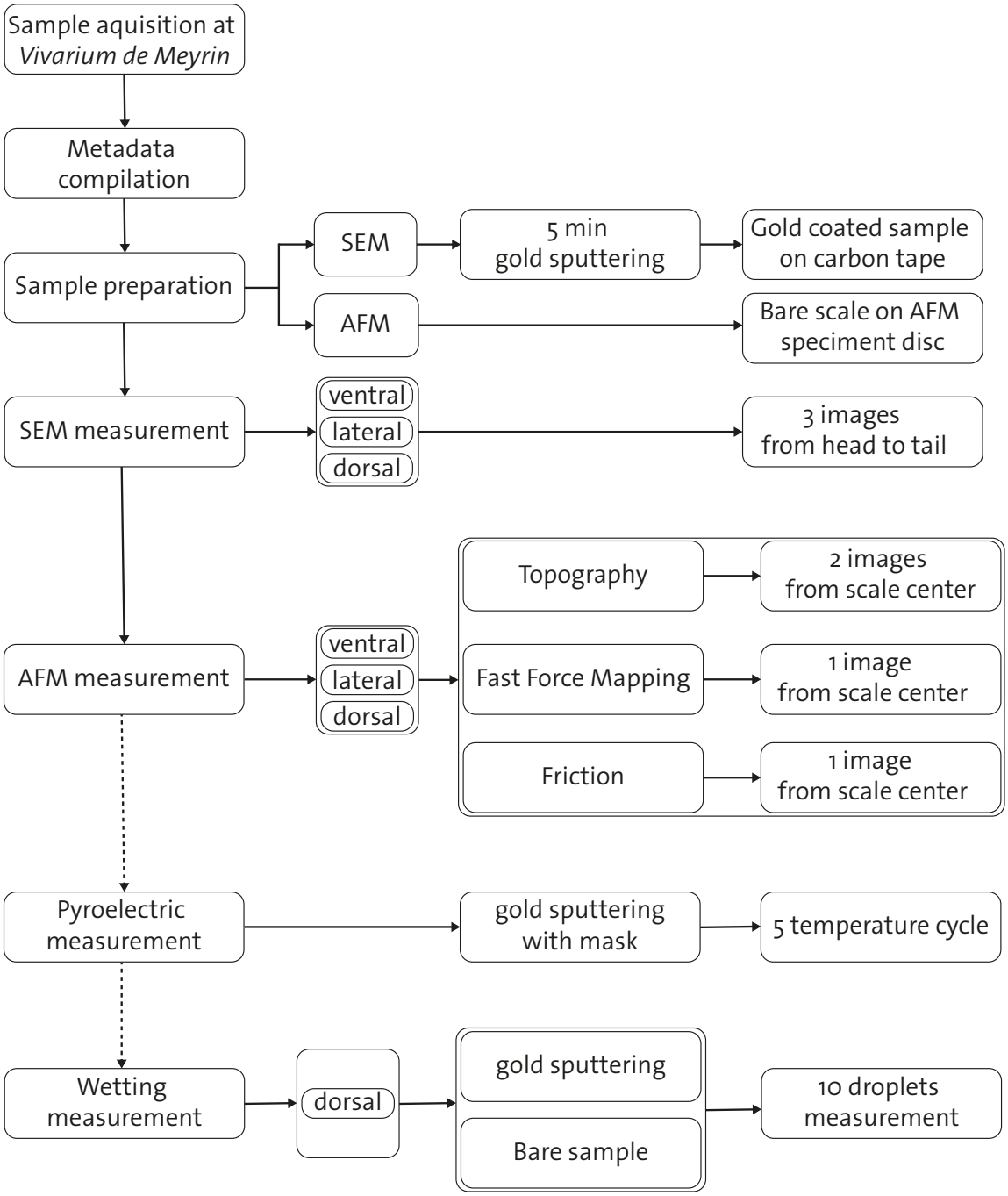


**Figure 3.3** – Schematic representation of the project workflow. First the sheds are acquired from the *Vivarium de Meyrin*. All the samples are recorded in a metadata file for classification purposes. The first measurements are performed by SEM in order to have a broad view of the microstructures. From there AFM is used to measure mechanical properties, starting with the topography, following up with stiffness, and ending with friction maps. The study was expanded by wetting and pyroelectric property measurements on a few select samples.

# 3.2 | Scanning electron microscopy

Scanning electron microscopy (SEM) was invented in 1925 by Ruska & al. [26]. It has since found a widespread use mainly in physics and biology, as a technique to precisely characterise surface morphology and composition. The operating principle of an SEM is very similar to that of old televisions with cathode-ray tubes: an electron beam is accelerated and focalised with electromagnetic fields towards the sample, and outgoing particles are collected and used to construct an image.

## 3.2.1 Beam production and focalisation

To generate the electron beam, either thermionic emission or field emission [27] are used.

| **Method** | **Brightness** ($A/cm^2$ sr) | **Lifetime** ($h$) | **Source size** | **Energy spread** $\Delta E$ (eV) | **Beam current stability** (%/h) |
|---|---|---|---|---|---|
| Thermionic Emission (Tungsten hairpin) | $10^5$ | 40-100 | 30-100 $\mu$m | 1-3 | 1 |
| Thermionic Emission ($LaB_6$) | $10^6$ | 200-1000 | 5-50 $\mu$m | 1-2 | 1 |
| Schottky Field Emission | $10^8$ | >1000 | 15-30 nm | 0.3-1.0 | $\sim 1$ |

**Table 3.2** – Comparison of the characteristics of different emitters used in commercial SEMs. Note the highest brightness is produced by field emission [27].

Thermionic emission is based on the thermally assisted emission of electrons from a source, usually tungsten or $LaB_6$. Thermal energy is provided to the electrons making them overcome the work function of the emitter. Field emission makes use of an electric field in order for the particles to leave the emitter, usually through the use of a "tip-effect": a voltage is applied to a sharp tip, concentrating the field lines at its apex due to the geometry of the system. This creates a strong electric field, which emits the electrons from the tip.

Other methods such as the Schottky Field emission[3] (SFE) combine both, using the electric field to reduce the height of the potential barrier that the electrons have to overcome in order to leave the solid, thus allowing a higher current for the same emitter temperature. The current density in this process presents a highly non-linear dependence on the field E, as detailed in equation (3.1), where $m_e$ is the electron's mass, $k_B$ the Boltzmann constant, $h$ is the Planck constant, $\epsilon_0$ is the vacuum permittivity, $T$ is the temperature and $\phi$ is the work function of the solid. The first term in the exponential corresponds to the lowering of the potential barrier due to the Schottky effect [28].

$$J_s = \frac{4\pi m_e (k_b T)^2}{h^3} \exp\left( \frac{e^{3/2} E^{1/2}}{(4\pi\epsilon_0)^{1/2} k_b T} - \frac{\phi}{k_b T} \right) \tag{3.1}$$

A SFE emitter usually combines this effect with the use of a thin layer of ZrO on top of the tungsten filament. This reduces the effective work function compared to a tip of pure crystalline tungsten. Additionally, the tip is designed with a reservoir of $ZrO_2$ on the emitter, allowing adsorption of ZrO. An SEM image of a reservoir can be seen in Fig. 3.4. Under regular use the life expectancy of such a reservoir being usually from 12 to 15 months, with the reservoir being the limiting factor: once it is empty, the emitter needs to be changed [27].

The beam produced by all the different kinds of emitters is still too large to obtain an optimal resolution, so magnetic lenses are used to focus it. A magnetic lens is an electromagnet: a current goes through a copper wire inserted into an iron core, such that the wire produces a strong magnetic field perpendicular to it. The geometry of the magnet is engineered to control the density and orientation of the magnetic field, shaping the beam. In a magnetic lens, the focal length is the distance between the point where the beam starts to bend and the point where the beam crosses the optical axis. Varying the current in the electromagnet allows to control the value of the focal length: $f = \frac{V_0}{(NI)^2}$, where $V_0$ is the accelerating voltage of the beam, $N$ the number of spires in the magnet and $I$ the current. The usual optical lens formula can also be used for magnetic lenses:

$$\frac{1}{f} = \frac{1}{p} + \frac{1}{q} \tag{3.2}$$

where $p$ is the lens-object distance and $q$ lens-image distance, and the demagnification is defined as $m = \frac{p}{q}$. The simplest SEM column is composed of two lenses. The first one is a condenser lens, with a

[3] This method is used in the Jeol JSM-7600F, the microscope used for the SEM part of this study.

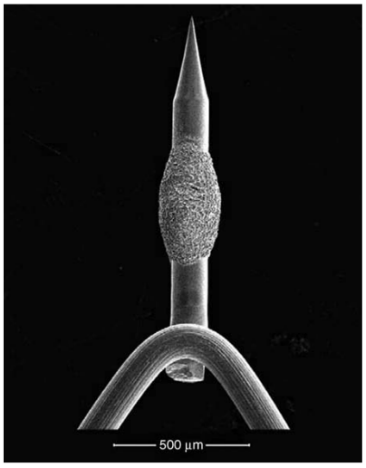


**Figure 3.4** – An SEM image of a SFE emitter with a $ZrO_2$ reservoir [28]

variable current to control the demagnification. The second, an objective lens, is used to focus the beam onto the sample. The Jeol JSM-7600F used in this study uses a snorkel lens (see Fig. 3.5), where the sample is placed outside the objective lens. This geometry allows for large samples to be measured.

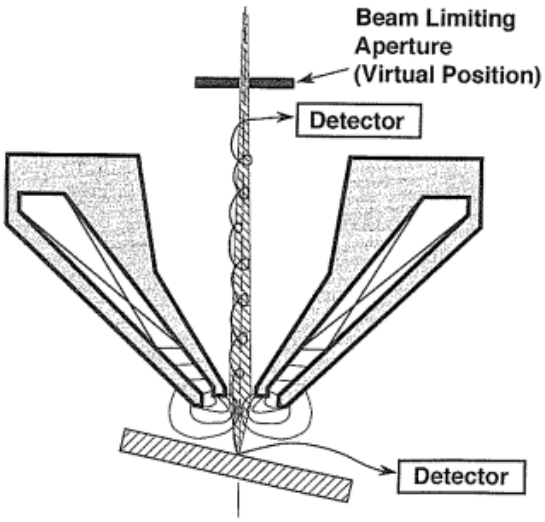


**Figure 3.5** – Schematic of a snorkel lens. [27] The magnetic field extends far from the pole, thus allowing for a large sample size, since it does not need to be inside the lens, contrary to an immersion lens. However it as a lower aberration formation than the pinhole lens, which also accommodates large sample sizes.

Fig. 3.6 presents an overview of the lens column, where $d_i$ and $\alpha_i$ are the diameters and divergence angles of the beam at different stages of the beam focusing, $f_i$ are the focal distances of the lenses. In a standard SEM, there are typically three control parameters acting on the image quality [27]:

1. **The objective aperture size**, which controls the portion of the beam going through the objective lens and can reduce the effects of aberration. It also controls the depth of field and the beam intensity.

2. **The working distance**, which, when increased, reduces the demagnification $m$, thus increasing the final beam size. This results in a reduction of the resolution (even after refocusing by using the objective). However, the angle $\alpha_2$ increases, which results in a larger field of view.

3. **The current** going through the condenser lens controls the focal length of the lens. A reduction of the focal length produces an increase in beam size, but also an increase in electron irradiation

intensity of the sample. Therefore, an equilibrium must be found to minimise the beam size and at the same time keep enough intensity to image the sample.

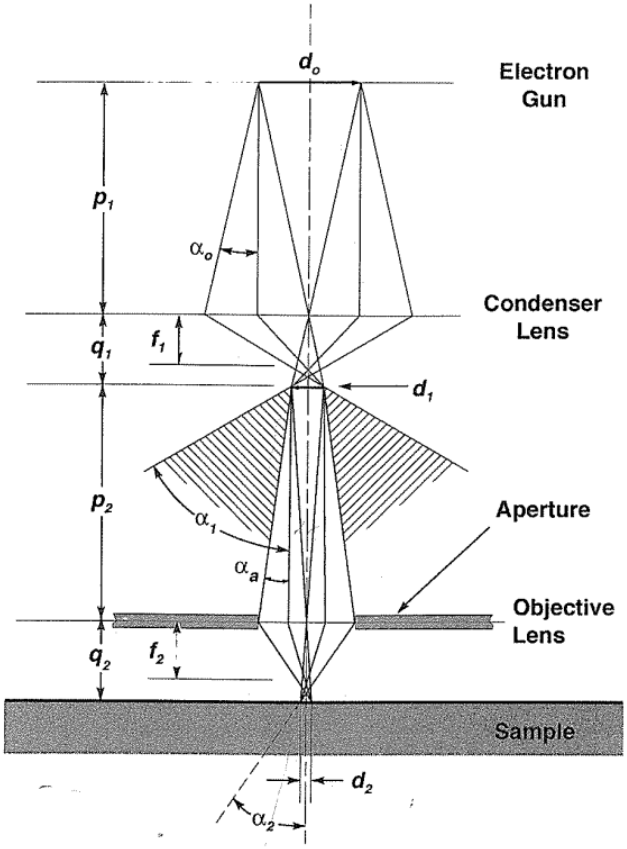


**Figure 3.6** – Schematic of the beam path. The beam starts with a diameter $d_0$ and a divergence angle $\alpha_0$. It is focused by the condenser lens to a diameter $d_1$, with a large divergence angle $\alpha_1$. Finally the objective lens reduces the diameter even further, leading to a spot size $d_2$. Image from ref. [27]

### 3.2.2 Beam interaction with the sample

In a SEM, electrons penetrate the sample for up to a few micrometres in depth. The penetration volume is called the interaction volume and is pear-shaped (Fig. 3.7). In this volume, numerous scattering events take place and decrease the resolution of the system compared to the one expected from the beam size [27].

Various phenomena occur during the interaction of the beam with the sample, producing different kinds of particles. The SEM used in this study has detectors for the following three types of outgoing particles:

- **Secondary electrons**. The incoming electrons give part of their energy to the bound electrons of the sample. The energy is sufficient to ionise the atoms fully, and the detector collects the outgoing ionised electrons.
- **Backscattered electrons**. Beam electrons interact by elastic scattering with the sample and are scattered back into the detector. The backscattering depends on the atomic number so it can be used to determine the local chemical composition of the sample qualitatively.
- **X-ray emission**. The incoming electrons can excite bound electrons within the sample to a higher energy level. Since this results in an unstable configuration, after some time the excited electrons will decay to their initial state, emitting photons whose frequency depends on the energy gap between

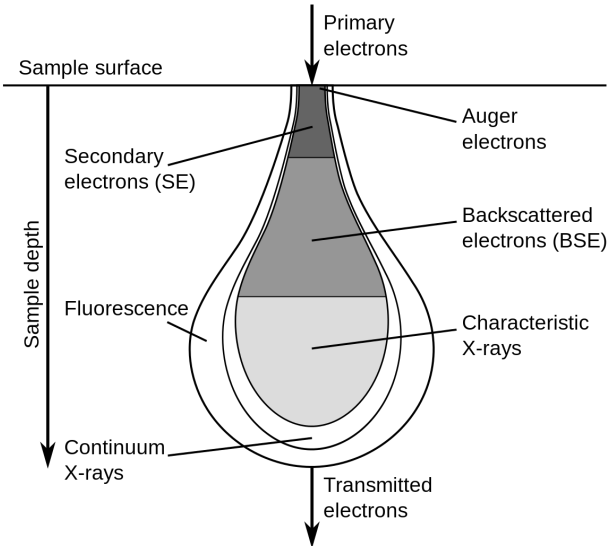


**Figure 3.7** – Electronic interaction volume in a SEM. Each reaction has a certain penetration depth, leading to a lower resolution. An SEM can usually detect secondary electrons, backscattered electrons, as well as x-ray emission. [29]

the bound and excited states. Measuring such photons, therefore, allows the chemical composition of the sample to be determined quantitatively.

## 3.3 | Electrode deposition

Since the snake scale samples are primarily composed of insulating keratin, it is necessary to coat them with a conductive layer for SEM imaging in order to avoid undesirable charging effects. Plasma sputtering is a well-known technique mainly used to produce thin layers and coatings. Furthermore it allows the growth of near-perfect thin films of pure metals and alloys. It was used during this project to deposit thin layers of gold on our samples.

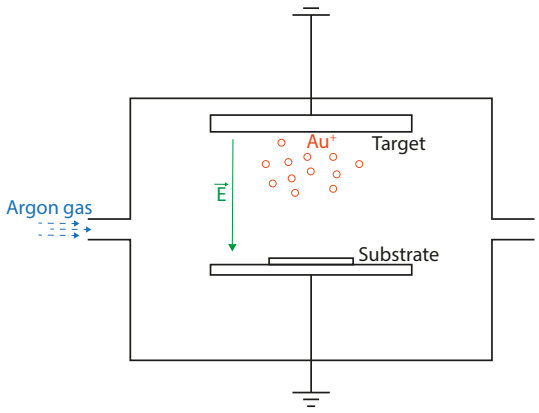


**Figure 3.8** – Schematic representation of a typical DC diode sputtering system. Image based on ref. [30]. A voltage is applied between the target and the substrate, producing an electric field moving the gold particles into the sample.

The standard design of a DC diode sputtering system consists of two metallic plates kept under a controlled argon atmosphere. One of the plates is a metallic target - in our case, gold. The other one is a sample holder. The plates are positioned in a parallel-plate capacitor geometry, with a generated electric field used to ionize the gas and accelerate the resulting $Ar^+$ ions toward the target. The magnitude of the field is chosen to make the ions collide with the gold plate at sufficient speed so that the transferred energy exceeds the binding energy of the metal. At the moment of the collision, two events can occur [30]:

- The heavy ion **backscatters**: this effect does not contribute to the sputtering and has a very low probability of happening.
- The heavy ion **penetrates** the target: it transfers its energy to the surrounding area, such that the metal atoms close to the point of impact gain energy. If sufficient, it allows them to escape the target and deposit onto the sample.

Such a bombardment emits secondary electrons and photons due to energy dissipation; it also emits clusters or individual metal atoms due to kinetic energy and momentum transfer[4].

In a perfect vacuum, the mean free path of the sputtered metal atoms would be substantial, and the movement could be considered ballistic. In such a system, the particle would travel at high velocity, which could damage or even resputter the sample[5]. However, the presence of the argon atmosphere reduces the mean free path and the sputtered atoms smoothly deposit onto the sample at a far lower speed.

[4] Fortunately, the probability of cluster emission is low, so most of the emission is single neutral metal atoms.
[5] In a resputtering process, the incoming metallic atoms transfer their energy to the already deposited atoms, making them leave the surface.

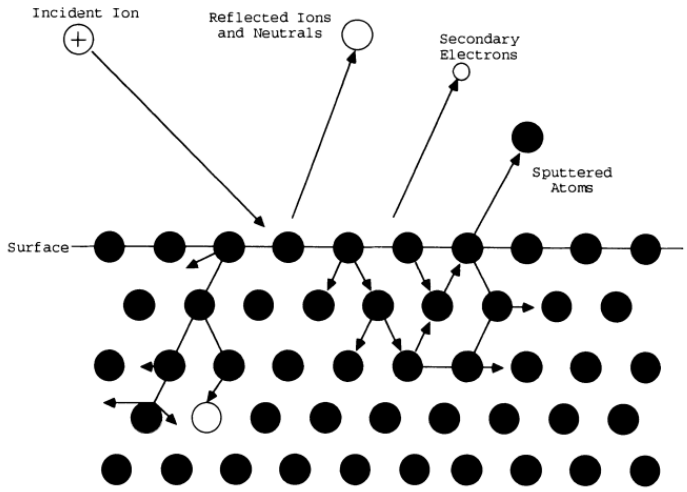


**Figure 3.9** – Scattering process taking place during sputtering. The incident ions enter in contact with the surface and can either be reflected, or penetrate into the surface, leading to the expulsion of a sputtered atom. The energy dissipation leads to electronic and photonic emission. Image from ref. [31]

# 3.4 | Atomic Force Microscopy

Atomic force microscopy (AFM) is a surface sensitive technique used to probe many very different physical properties, from measurements as simple as topography scans to determine the morphology or surface roughness, to more complex functional probing of mechanical, electrical or magnetic properties at the nanoscale.

## 3.4.1 Operating principle

### Piezoelectric actuators

At its core, AFM is quite a relatively simple device: it consists of a nanometric tip located at the end of a cantilever which is moved by piezoelectric actuators. The probe slides across the surface of the sample and contact forces attract or repel the tip inducing a bending of the cantilever. The bending of the cantilever is used to keep the tip-sample interaction constant and is recorded and analyzed to extract physical quantities.

Even though the concept behind AFM is simple, the application is less so: moving a nanometric tip above a sample, without destroying the tip or the sample, requires some precise engineering. A system of piezoelectric actuators is used to move the tip in three dimensions. Piezoelectrics are materials that exhibit a linear deformation under an applied voltage, and vice versa; the deformation being usually of the order of hundreds of picometers, up to hundreds of nanometers per volt. The most common geometries of piezoelectric actuators for microscopy applications are tube scanners and tripod scanners [32] (Fig. 3.10).

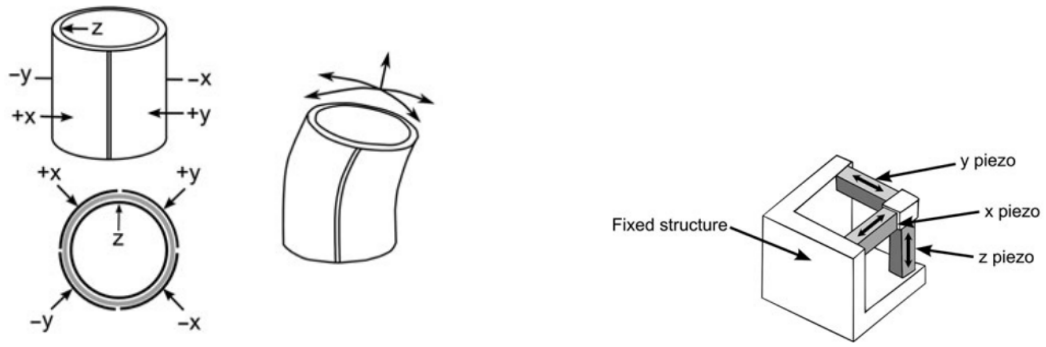


**(a)** Tube scanner **(b)** Tripod Scanner

**Figure 3.10** – Example of the two most common piezoelectric actuators. (a) The tube scanner uses cylindrical-shaped piezoelectric tubes, with four outer electrode quadrants and one inner cylindrical electrode. Applying voltage to the outside quadrants bends the tube, enabling movement in the x or y direction. Voltage applied to the inner electrode expands the tube along the z axis. (b) The tripod scanner uses three linear piezoelectric actuators along the three orthogonal axes of movement. Images from ref. [32]

### Tip-sample interaction

The interaction between the tip and the sample is governed by a combination of multiple forces acting at different length scales; van der Waals, electrostatic, and magnetic forces combined with the Pauli exclusion principle [33]. The **van der Waals force** is produced by charge fluctuation in neutral atoms, creating transient dipole moments. The interaction between two van der Waals dipoles can be approximated by:

$$U_{vdW} \propto \frac{-1}{r^6} \tag{3.3}$$

Because the van der Waals interaction is long range[6], it is necessary to consider the interaction between a volume of the tip $\mathrm{d}V_A$ and a volume of the sample $V_B$, such that the interaction is:

$$\mathrm{d}U_{vdW} = -\frac{C\rho_A\rho_B}{|r_a - r_b|^6}\,\mathrm{d}V_A\,\mathrm{d}V_B \tag{3.4}$$

[6]Between water and a neutral surface, the van der Waals interaction is approximately $10meV$ at 3Å[34].

Where the $\rho_a$ and $\rho_b$ are respectively the tip and sample densities. Integrating over a sphere of radius $R$ for the tip, and a plane for the sample, we obtain a long-range van der Waals potential of the form:

$$U_{vdW} = -\frac{HR}{6r} \tag{3.5}$$

This potential defines the interaction for distances larger than 1 nanometre. For short-distance interactions the **Pauli exclusion principle** dominates. The exclusion principle is often repulsive, due to the overlap of electronic states, but a process similar to chemical bonding can happen, leading to attractive forces. Solving the Schrödinger equation is far too complicated for most applications, and usually the Lennard-Jones potential (see Fig. 3.11) is used as an approximation:

$$U_{LJ} = 4U_0 \left[ \left( \frac{R_a}{r} \right)^{12} - \left( \frac{R_a}{r} \right)^{6} \right] \tag{3.6}$$

**Magnetic forces** can be neglected in our case, and the **electric force** are long-range interaction of the form (assuming a cone-shaped tip and an infinite plane sample):

$$F_e = -\pi\epsilon_0 \frac{R}{r} (\Delta V)^2 \tag{3.7}$$

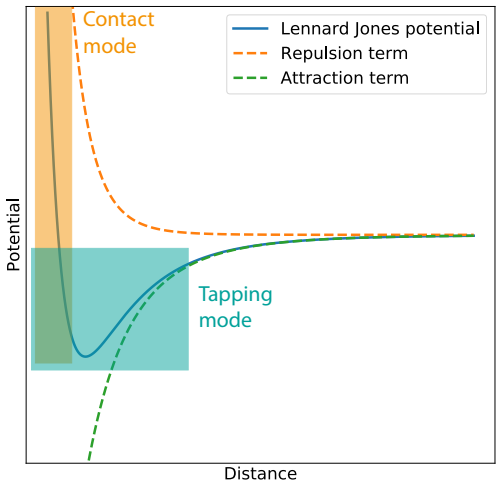


**Figure 3.11** – Schematic behaviour of the Lennard-Jones potential, showing the attractive and repulsive regimes. The orange and blue shaded areas correspond to regions where the contact and tapping AFM modes operate, respectively. Based on an image from *Scanning Probe Microscopy* [33]

### Detection

To probe either the morphology or the functional and mechanical properties of the sample, it is necessary to detect the tip-sample interaction precisely. Five detection techniques have been implemented over the course of AFM development history [32] :

- **Scanning Tunnelling Microscope (STM):** A biased STM tip is located above the metal-coated cantilever of the AFM, and the tunnelling current between them is measured with a current amplifier. This was the original method used for the proof of concept of the AFM in 1985 [35], but its complexity and low bandwidth renders it impractical for general applications.
- **Interferometer:** A laser illuminates the AFM tip through an optical fibre located just above the cantilever, and the reflected beam goes through an interferometer [36]. This technique allows for a very precise measurement of tip displacement, as opposed to cantilever deflection measured by

optical lever sensors. However, there is a risk of "fringe hopping" when the cantilever suddenly displaces over a large distance: when there is a rapid change of deflection, the interference pattern changes rapidly, causing the detector to miss one or more maxima/minima of the pattern, leading to a misevaluation of the tip-sample distance by a multiple of the laser wavelength.

- **Crystal oscillator:** The tip is engineered to contain a piezoelectric crystal inserted between two gold electrodes at the back of the cantilever. If an AC voltage is applied to the system, it induces vibrations in the crystal. The induced current in the crystal is measured and its response used as the feedback signal. As the tip approaches the sample, the resonance frequency of the system changes, inducing a phase-shift and an amplitude reduction of the induced signal. [37] This technique allows for precise measurements and removes the need for a complex optical setup that can become troublesome for some application of AFM, such as at ultra low temperatures, in magnetic fields or in in-situ. However, since the system is directly integrated into the tip, it leads to significantly more expensive tips than the one used in AFM based on other detection mechanisms.
- **Piezo-resistive cantilever:** The cantilever contains a small piezoelectric element which produces a voltage when it bends [38] (using the converse piezoelectric effect: a deformed piezoelectric produces a voltage). This technique shows the same advantages and disadvantages as the crystal oscillator configuration.
- **Optical lever sensor:** This is the most ubiquitous method of detection. A laser beam illuminates the back of the cantilever and is reflected into a four-quadrant photodetector [39]. When the cantilever bends, the position of the laser spot on the photodetector is displaced. If the detector is far away from the tip, a small deflection angle will induce a large displacement on the detector, allowing for a precise measurement of the deflection. This method is the most versatile since it allows the measurement not only of the bending but also of torsional movement and provides the highest bandwidth.

### Feedback and control

It is necessary to use feedback to keep the tip-sample interactions constant (either with a constant height above the sample or in contact with a constant deflection). This is usually achieved through the use of a controller which receives error signals and feeds inputs into the system. As can be seen in Fig. 3.12, the error signal is the difference between a set-point $w$ and the output of the sensor $x(t)$, and is used by the controller to adapt the system response. This will lead to a new output of the sensor, which will be fed back into the controller, leading to the creation of a feedback loop.

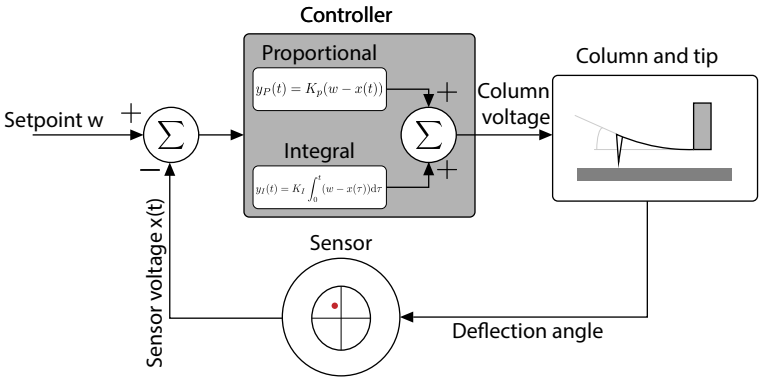


**Figure 3.12** – Schematic of a PI feedback controller. The controller take a setpoint $w$ and the sensor output $x(t)$ as inputs, and computes the error signal $w - x(t)$. The controller then applies the equation (3.4.1) to compute the voltage output to apply to the column, leading to a new sensor voltage $x(t)$. (Based on an image in *Scanning Probe Microscopy* [33])

In the case of an AFM controller operating in static mode (see Chap. 3.4.2), the set-point is given by the user as a voltage, corresponding to a position of the laser on the photo-diode, which in turn

corresponds to a specific deflection of the cantilever. In dynamic mode, the set-point is often the oscillation amplitude, which corresponds to a fixed tip-sample distance. The feedback signal is then the effective voltage/amplitude of the tip oscillation.

The most common controller is the PI controller, which receives the error signal, defined as $w - x(t)$ and applies the following function to it [33]:

$$y(t) = K_p(w - x(t)) + K_I \int_0^t (w - x(\tau))\,\mathrm{d}\tau \tag{3.8}$$

The first term is the proportional part and the second the integral part of the controller feedback. $K_P$ and $K_I$ are the gains and are chosen to optimize the controller behaviour. The proportional function corrects the system input proportionally (hence the name) to the error signal. The variable $K_P$ can be seen as the reactivity of the controller: the larger it is, the more reactive the controller will be to deviation. However, too large a value of the constant can lead to oscillations around the set-point value. The problem of a pure proportional controller is that it will produce an offset between the effective value and the set-point as in most systems the system-input is non-zero at the set-point, whereas the proportional term is zero for $w = x(t)$.

The integral part of the PI controller corrects this problem. It sends a signal proportional to the sum of all the errors during the interval of time $[0, t]$. This eliminates the constant error of the P controller and allows the system to reach the set-point. However, the reactivity of an I-controller is low and does not allow for fast variations of the system input. Therefore, a combination of proportional and integral feedback is usually used.

### 3.4.2 Measurement modes

#### Contact mode

Contact mode is the simplest measurement mode in AFM. The tip is in contact with the sample, in the strongly repulsive potential regime (as can be seen in Fig. 3.11). In this case, the long-range interactions are negligible, and only the repulsive force between the tip and the sample leads to the cantilever deflection. In this work, this technique is used to measure either the topography or the mechanical properties such as the stiffness and the frictional behaviour.

To image the topography of a sample, the deflection is used as a set-point, such that the applied force is constant. The tip is rastered across the sample by the xy-actuators. When topographic changes occur, the tip deflection will change and the z-axis actuator will displace the tip slightly to bring the deflection back to its set-point value. Since the short-range forces have a strong dependence on the tip-sample distance, this technique allows for topographical images to be acquired.

It is possible to locally measure stiffness with an AFM tip: a force versus deflection curve is acquired on a point of the sample by ramping the z-actuator. This first brings the tip in contact with the sample, and then keeps increasing the applied force at the area of contact driving the tip into the sample. This leads to a sample deformation and a tip deflection. Depending on the sample stiffness, the deformation/deflection ratio will be different, and will follow Hooke's law (see Chap. 2.1 for a detailed derivation of Hooke's law):

$$\delta = \left(\frac{9}{16RE^{*2}}\right)^{1/3} P^{2/3} \tag{3.9}$$

If the properties of the tip are known, this formula allows the materials Young modulus to be extracted.

In principle, other mechanical properties can be extracted by moving the tip laterally across the sample in contact mode. Since the cantilever is a lot stiffer along the lateral axis, it is possible to extract the tribological properties of the sample. However, this technique usually suffers from topographic cross-talk in the case of non-flat samples, so we have employed a more advanced technique described below to probe the friction of snake scales at the nanoscale.

#### AC mode

In contact mode, the tip and the sample can undergo damage due to the constant pressure applied on the sample, in case of large topographical variation, the tip can hit the side of the features and be

damaged. AC mode[7] is a non-contact technique based on an oscillatory mechanical excitation of the tip in order to record the topography of the sample. The tip is placed above the sample and excited at its resonance frequency. There are two configurations, either the tip is far from the sample and never touches it (non-contact mode), or the distance is such that the tip intermittently comes into contact with the sample (AC mode). The photodetector signal is fed into a lock-in amplifier to extract the amplitude and the phase of the oscillation. In this regime, the tip-sample system behaves as a mass-spring oscillator, where the interaction force and the deflection can be modelled as two springs. In such a system, the frequency and amplitude depend on the values of the spring constants $k_{1,2}$, which in turn depend on the tip-sample interaction and therefore the distance. Thus, running a feedback loop with the set-point on the amplitude, and using the z-actuator to keep the amplitude constant, allows the topography of the sample to be measured.

### Band excitation and Bending mode - dynamic friction

Three techniques were evaluated in order to try to recover friction properties with as little as possible topographical cross-talk. The first, using lateral excitation, employs a lock-in amplifier to measure the amplitude and phase at the lateral contact-resonance frequency. As can be seen in Fig. 3.13(a)-(c), this technique produces bright contrast on PS-LDPE, a copolymer blend commonly used for benchmarking nanomechanics measurements. However, the contact-frequency peak often shifts due to energy transfer between lateral bending and torsional movement [40]. This means that this lock-in technique could produce misleading results as the peak shifts. To take into account the shift of the peak, it is possible to excite the tip with a frequency band around the resonant peak. We combined band-excitation force-curves to investigate friction [41]. The idea is to laterally excite the tip while increasing the normal force applied by the cantilever to the sample. The evolution of the shape of the peak gives information on the dissipative forces present, and can therefore be linked to friction mechanisms. This technique works but is computationally demanding, leading to long acquisition times and low spatial resolution. While it yields a large amount of physical data, it is difficult to interpret since it encompasses a whole range of frictional behaviour and the dynamical stick-slip transitions.

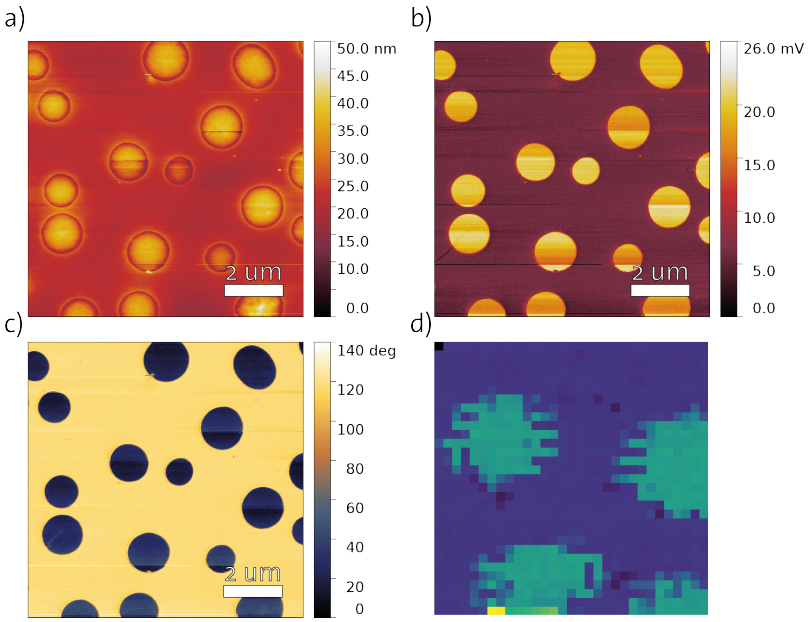


**Figure 3.13** – a) Topography of the PSLD-PE sample. b) Lock-in amplitude at the contact resonance frequency. c) Lock-in Phase at the contact resonance. d) slope of the linear response during the band-excitation. Clear contrast can be seen between the two components of the polymer on all the channels.

The band-excitation technique was ultimately judged too complicated in the framework of this project. Instead, we were inspired by the work of Mertens & al. [42, 43], which is based on the tracking of the bending motion of the cantilever. The sample is excited at a harmonic frequency of the free resonance

[7] AC mode is also called tapping mode or intermittent contact mode by some manufacturers.

frequency of the tip, and the response amplitude at the primary resonance is recorded. When the tip is brought into contact with the oscillating sample, it can either stick or slip. If the tip sticks to the sample, the response signal will only appear at the excitation frequency. However, if the tip starts to slip, the response will have a component at the free resonance frequency of the tip. Thus, by looking at the relative amplitudes of the two peaks, we can observe the energy transfer from the stick to slip transition. The larger the amplitude at the free resonance frequency, the lower the friction coefficient at that location in the sample. We first tried this technique on the PS-LDPE sample, and as can be seen in Fig. 3.14(b-c), obtained a similar contrast to the previous methods. Since Mertens & al. used a graphite (HOPG) sample as a proof of concept, we tried to reproduce these results. As can be seen in Fig 3.15(b-c), the amplitude and phase graphs show contrast, which is not visible on the topography. The results are similar to what the authors saw in their publication: a more significant contrast at the edges of the HOPG, where it is known that the frictional properties are different.

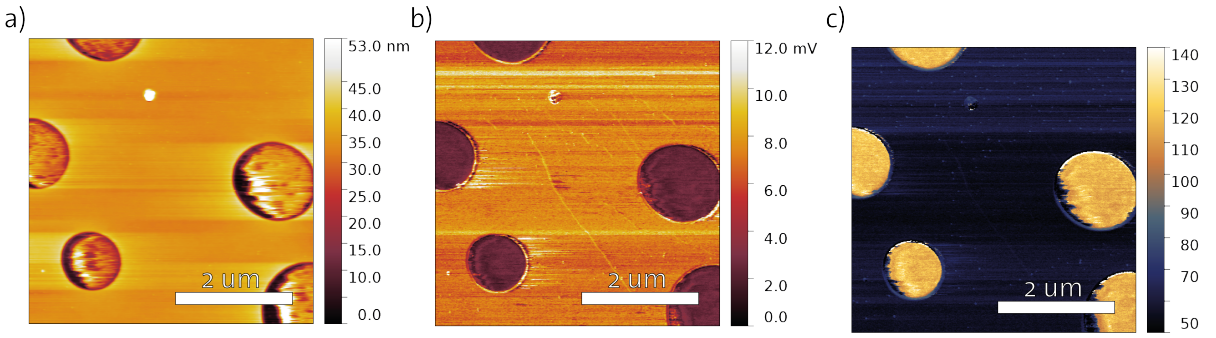


**Figure 3.14** – Bending friction measurement on PSLD-PE. The topography image (a) shows the presence of the two polymers. The two polymers give a clear contrast in the amplitude (b) and phase(c) channels.

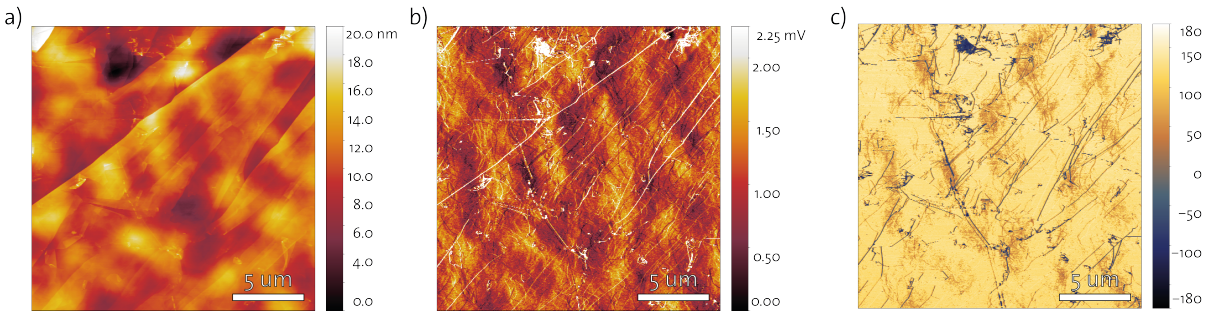


**Figure 3.15** – Bending friction measurement on HOPG. Steps are visible in the topography (a) and present large visible contrast in the amplitude(b) and phase(c) channels.

### 3.4.3 Humidity control

During the summer preceding the start of the project, we developed an upgrade of the homemade humidity controller for the AFM [44]. It enabled precise and extremely low noise control of the relative humidity so that all nanomechanical measurements could be performed under identical conditions. [44, 45] In the framework of this project, it was primarily used for the Young modulus measurements.

The controller uses a flow-mixing principle: flows of dry and wet nitrogen are mixed using two mass-flow controllers (Fig. 3.16). The wet flow is produced by an atomizer which creates a water-saturated atmosphere in a chamber. The dry flow is split into two, the first part goes through the saturated atmosphere, the other flows as is. Therefore the two flows can be considered either as "fully dry" or "fully wet". The resulting mixture can be continuously changed by modifying the ratio of the two flows, from a relative humidity of 5% up to 90% with a precision of less than one per cent.

The first version of the system had manual control of the flows [44]. The upgrade is centred around a Raspberry Pi (R.Pi), which carries out sensor acquisition, flow regulation, data acquisition, and communication between the controller itself and a remote user interface.

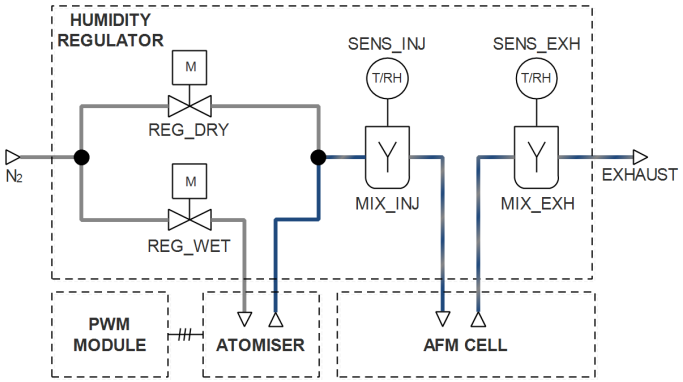


**Figure 3.16** – Schematic of the flows in a controller using flow-mixing principle.

To achieve the above tasks, the R.Pi hosts a multi-process server written in Python. Nine processes run in parallel, each taking care of a specific part of the system and shared memory in the form of a standard Python dictionary provides interprocess communication. The system is based on a core process consisting of a web server continuously receiving and sending a custom set of GET/SET commands based on a JSON API.

The other main processes are flow regulation, PID control, and sensor acquisition. The flow regulation process reads the shared memory, looking for any change to flow values coming from the PID or manual entry from the graphical user interface (GUI), and sends a corresponding DC voltage to the mass flow controllers to regulate the mixing of the flows. The PID process is a simple PID controller, reading the I, D and set-point values and continuously sending commands to the flow control to keep the humidity as close as possible to the set-point.

The system can be controlled using a client-side GUI written in C#.net which can be installed on any computer running Windows. This program gives full access to the humidity controller parameters, allowing the configuration of set-point, flows and close monitoring of the humidity status.

A detailed description of the controller can be found in appendix 6.2.

## 3.5 | Wettability

Additionally to the nanomechanical characterization of the snake scale microstructures, we examined the wettability of dorsal scales of different snake species to detect any variation in hydrophobicity which could potentially be correlated with the mechanical properties and morphology.

The experiment was first performed using a home-built setup consisting of a camera with a macro-lens, a white LED panel and a 3-axis precision stage (see Fig. 3.17(a)). A droplet was placed on the sample using a standard micropipette. The LED panel provided a uniform background, and the stage was used to place the droplet in the centre of the image and focus. The camera captured the resulting droplet. Data analysis was carried out using the contact angle analysis software developed by the Biomedical Imaging Group at the *École Polytechnique Fédérale de Lausanne* (EPFL) [46]. Unfortunately, the contrast was insufficient, leading to incorrect drop border extraction and thus to wrong contact angles.

To address this problem, subsequent measurements were performed on commercial setup[8] (see Fig. 3.17(b)), based on a similar configuration with the exception of the pipette being fixed above the plate. However, the most useful improvement was the built-in software which allowed a more precise and reproducible analysis of the contact angle.

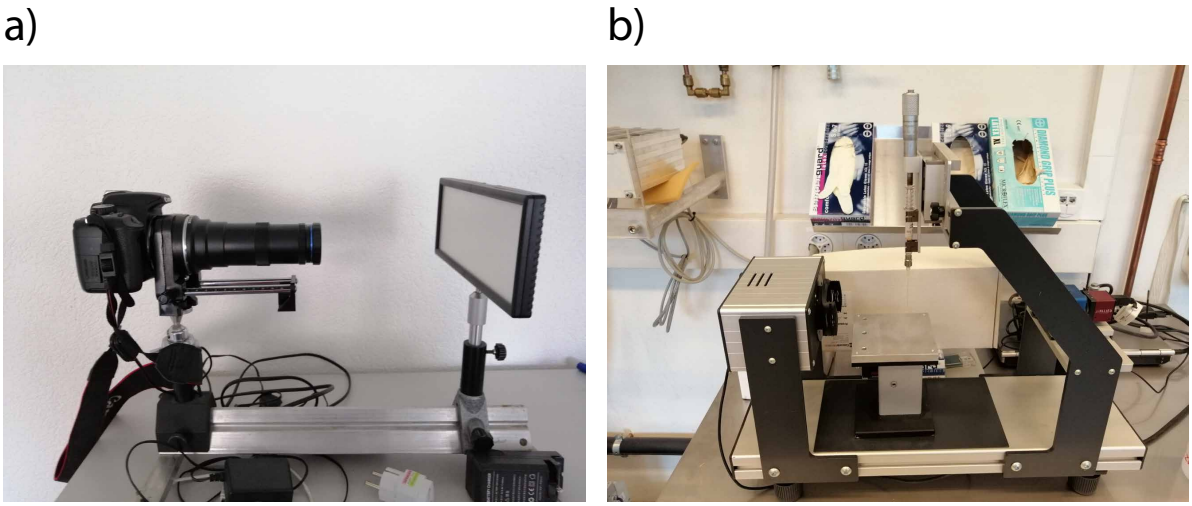


**Figure 3.17** – (a) Home-made contact angle measurement device, using a standard camera with a macro lens and a LED panel. (b) Commercial setup for contact angle measurements.

[8] Courtesy of Dr. Jérémie Teyssier, *Laboratoire des Technologies Avancées*.

## 3.6 | Pyroelectricity

As the snake scale microstructures are highly anisotropic and quasi-periodic, we decided to investigate whether the resulting micro-scale breaking of inversion symmetry confers any detectable polar properties to the scales, as previously reported for collagen structures [47]. Such properties can be probed via a bulk pyroelectric measurement. A typical pyroelectric setup consists of a grounded heater stage (which allows variation of a few degrees around room temperature), and two needle probes which are used to measure the pyroelectric current. As can be seen in Fig. 3.18, the two probes are mounted on 3-axis precision positioning stages individual electrodes to be probed. The typical currents measured by such a setup are of the order of $\mu A$, so in addition to the stage, low noise and high precision electronics are necessary to amplify the signal[9].

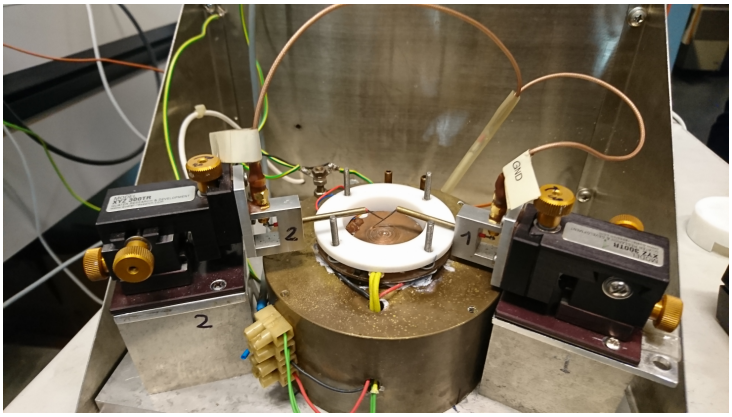

**Figure 3.18** – The pyroelectric setup used to measure the coefficient of the snake scale (from Prof. Damjanovic, ceramics Laboratory, *EPFL*).

We initially planned to measure the pyroelectric coefficient along the three main axes of our samples, so top electrodes were patterned in a cross-shaped configuration (see Fig. 3.18) with a single central ground electrode at the back. Thus, by using one of the border electrodes, we expected to mainly measure the in-plane pyroelectric coefficient component, as the sample is thin. In hindsight, this electrode configuration was probably not optimal: the low pyroelectric coefficient of the keratin structure was difficult to extract from the noise since the small electrodes lead to a small current. We did not push this study further, but should we return to the question of pyroelectricity, we will use a different electrode geometry with two large pads in order to improve the signal-to-noise ratio.

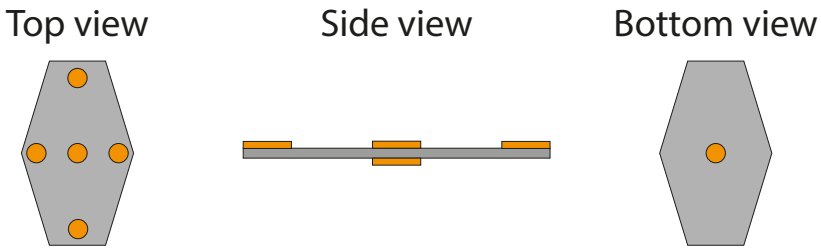


**Figure 3.19** – Schematic representation of the electrodes deposited on snake scales for pyroelectric measurements. The cross-shape enables measurements of the pyroelectric coefficient along the three main axes.

[9] Measurements performed at EPFL, courtesy of Prof. Dragan Damajanovic.

# 4 Results and analysis

## 4.1 | Morphological microstructure classification

### 4.1.1 Morphology imaged by SEM and AFM

The initial working classification scheme we developed was based on the visual inspection of scale microstructures using SEM images, supplemented by AFM topographies when necessary to resolve finer 3D features (which may not be as readily apparent in SEM). From the sixteen species investigated, we were able to distinguish six different microstructures, which we termed **fibril**, **plate**, **hole**, **dune**, **spike** and **leaf**.

As shown in Fig. 4.1(a), the **fibril** structures are characterised by the presence of strongly oriented digitation along the cranial-caudal axis. This structure is present on eleven of the sixteen investigated species. It covers the body of most*Elapidae* and *Colubridae* and appears in a large number of other species on the ventral and lateral scales (Table 4.1). Most of the scales present some small **holes** that are often visible only in the AFM measurements, but some of the scales present structures that are mostly composed of a regular arrangement of holes, as can be seen in Fig. 4.1(b). For instance, this microstructure appears on the lateral and dorsal scales of *Viperidae*. The **plate** structure in Fig. 4.1(c) is characterised by large cell shapes, with homogeneous border and the presence of low elevation structure. It is only present in two of the three *Boidae* species: *Sanzinia madagascariensis* and *Boa constrictor*. The SEM images of the third *Boidae* (*Corallus Hortulanus*) are not sufficiently clear to attribute a classification with certitude, but the structure seems to be similar to a plate structure. The **dune**, **leaf** and **spike** structures, in Fig. 4.1(d-f), appear to be rare, each observed only in one species. In retrospect, the dune and pike microstructures could probably be classified as variations of the plate and holes structures respectively. However, the leaf structure is truly unique as it has a larger scale than the other structures: it consists of flat sheets which protrude from the surface of the scale. It seems to be present only on the dorsal scale of *Bitis Arietans*.

The fibril, plate, hole and dune microstructures showed maximum height of variations of approximately 0.15 $\mu m$, 0.05 $\mu m$, 0.20 $\mu m$, 0.45 $\mu m$, allowing detailed topographical AFM measurements (as shown in Fig. 4.1, inserts) and nanomechanical characterisation to be performed. Such measurements allowed us to quantify the features metrologically and to distinguish fine details which were not accessible by SEM, such as small holes between the fibrils. Unfortunately, the spike and leaf structures presented too important height differences to be imaged by AFM[1].

We note that the microstructures across the length of an individual scale are not homogeneous. As can be seen in Fig. 4.2 for images taken in the cranial, middle and caudal zones of fibril, plate and leaf structures, the microstructure presents a clear evolution. On the cranial side, we always observe very similar features across all the species investigated: the structures present nanometric holes and no digitation or noticeable height differences. Traversing the scale towards the caudal zone, this initial configuration evolves into more complex structures: strong denticulation, channels, holes. Arrigo and al. showed that the simple structure at the cranial side is very similar to the scale microstructure of neonatal individual [7]. For mechanical and tribological studies, we focused on the caudal zone, shown in Fig. 4.2, where the fully developed microstructures were observed.

[1] As he maximum range of the z-actuator in the AFM used for this study is 5 $\mu m$, attempting to image larger features could lead to tip or sample damage.

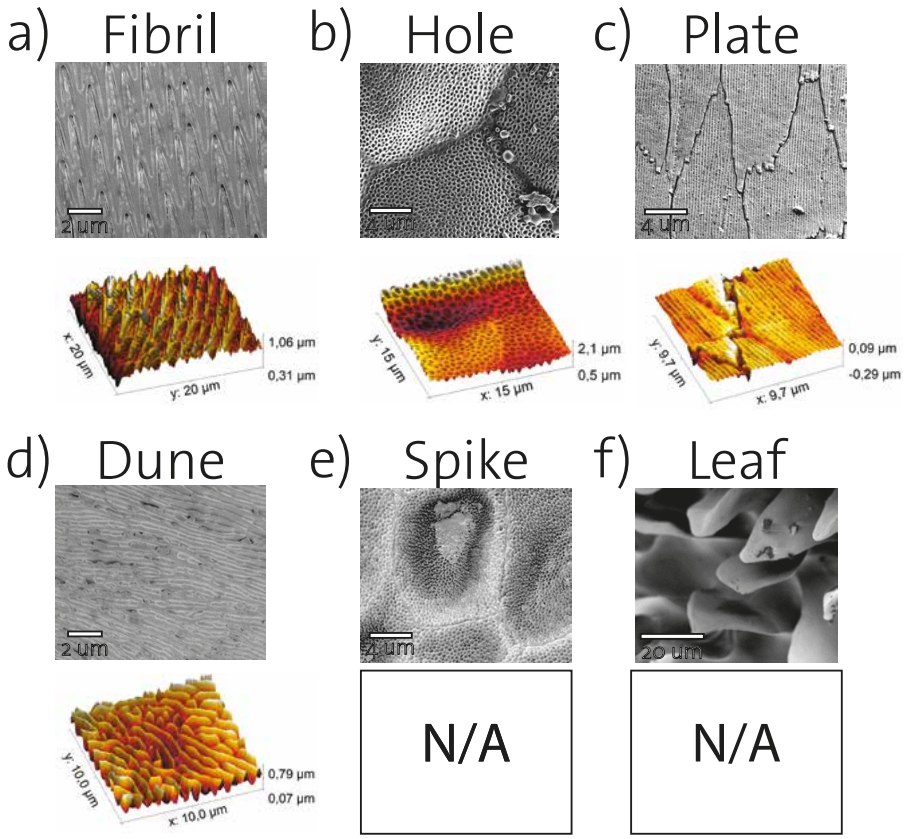


**Figure 4.1** – SEM and, when possible, corresponding AFM images representing the microstructure classification presented in this study. (a) The fibril structure is an arrangement of periodic digits. (b) The hole structure regroups the scales with periodic arrangements of small holes. (c) The plate structure is an arrangement of large flat cells. (d) The dune structure is an arrangement of channels flowing along the scale. (e) The spike structure consists of an arrangement of small barbs on the scale. (f) The leaf structure is the most peculiar structure due to its high elevation and large scale compare to the other structures.

| **Scientific name** | **Ventral** | **Lateral** | **Dorsal** |
|---|---|---|---|
| *Morelia viridis* | Fibril | Fibril | Holes |
| *Naja melanoleuca* | Fibril | Fibril | Fibril |
| *Naja nivea* | Fibril | Fibril | Fibril |
| *Naja samarensis* | Fibril | Fibril | Fibril |
| *Sanzinia madagascariensis* | Plate | Plate | Plate |
| *Boa constrictor constrictor* | Plate | Plate | Plate |
| *Corallus hortulanus* | N/A | N/A | N/A |
| *Bitis arietans* | N/A | N/A | Leaf |
| *Crotalus atrox* | Fibril | Fibril | Dunes |
| *Deinagkistrodon acutus* | Fibril | Fibril/holes | Holes |
| *Protobothrops elegans* | Fibril | Fibril/holes | Spikes |
| *Daboia russelii* | N/A | N/A | Holes |
| *Philodryas baroni* | Fibril | Fibril | Fibril |
| *Pantherophis guttatus* | Fibril | Fibril | Fibril |
| *Orthriophis taeniurus friesei* | Fibril | Fibril | Fibril |
| *Lampropeltis triangulum hondurensis* | Fibril | Fibril | Fibril |

**Table 4.1** – Table of the presence of the structure types. For some of the species, the sheds were too damaged to clearly define a microstructure classification based on SEM or AFM images.

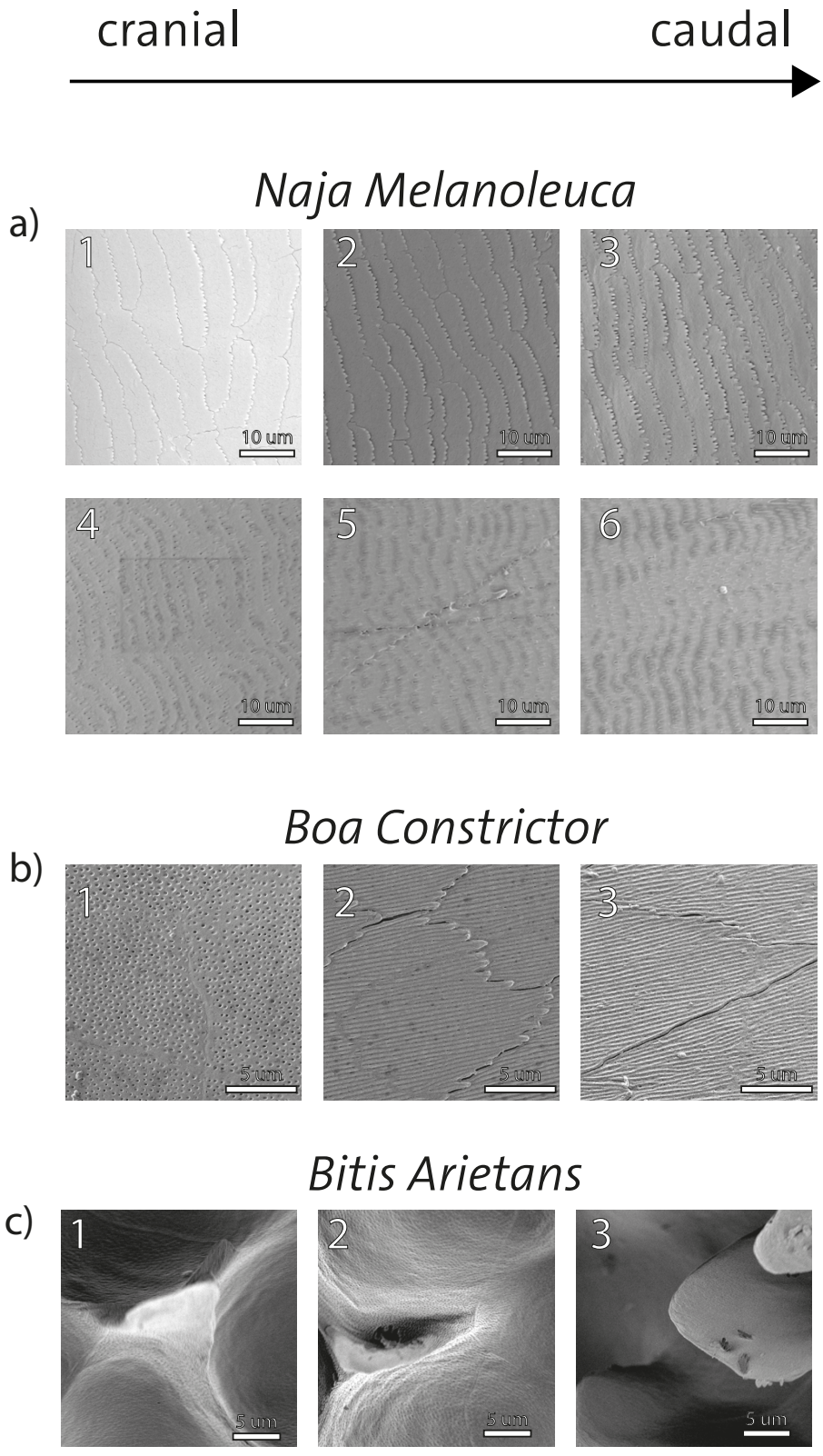


**Figure 4.2** – SEM images showing the evolution of the microstructure from head-side (cranial) to tail-side (caudal). (a) Images of *Naja Melanoleuca*, most of the fibril structures exhibit similar evolution. (b) Image of the evolution of plate structures on *Boa Constrictor*. (c) Unusual structure evolution on the *Bitis Arietans*.

### 4.1.2 Comparison with more general classification schemes

During the pursuit of this work, a detailed investigation of thousands of snake species, focusing on microstructure evolution, was reported by Arrigo and al. [7] This study allowed us to place our morphological observations in a more general context and obtain valuable information on life habit classification of the different species.

To classify snake scale microstructures, Arrigo et al. developed a system based on four morphological parameters:

- **Cell shape**: polygonal, wide
- **Cell border**: regular, short/mild/long digitation, sawteeth
- **Cell surface**: smooth, holes, straight channels, labyrinth channels
- **Ridges**: absence, presence

As shown in Fig. 4.3, the **cell shape** is defined as polygonal if the ratio between the width of the cell and its length is inferior to 2; otherwise, it is considered as wide. The **cell borders** are easily distinguishable as regular, digitated or sawteeth. Moreover, the ratio between the length and width of the fingers was considered to further separate three categories of digitation: short, mild and long. For the **cell surface**, the authors used an image processing technique based on the *OpenCV* computer vision library in combination with machine learning algorithms with a training set of manually selected contours defining whether the surface presented holes or channels.

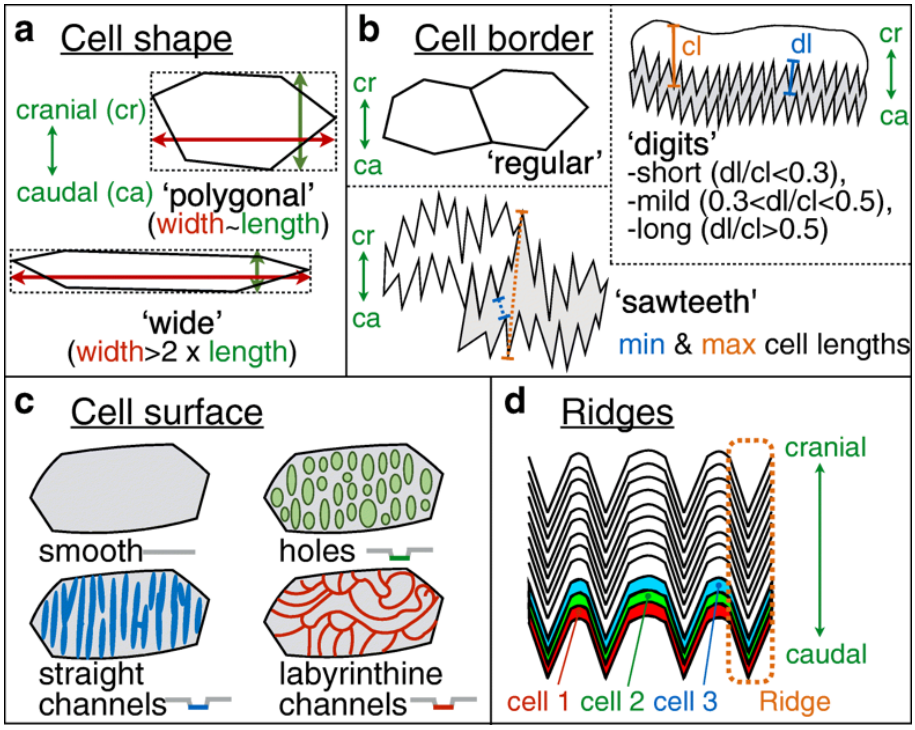


**Figure 4.3** – Figure from Arrigo & al [7]. showing the four morphological parameters. (a) **Cell shape** is either polygonal or wide. (b) **Cell border** is either regular, sawteeth, or digits; with a subclassification for digits, depending on the length to width ratio of the digits. (c) **Cell surface** can present holes, straight/labyrinthine channels or be flat. (d) Finally the surface can present **ridges** or not.

To verify if our morphological observations are compatible with this classification scheme, they were sorted using the parameters above. Given the small data set of sixteen species investigated in this study, simple visual inspection of the cell surface from SEM and AFM images was used to classify the structures. As summarised in Table 4.2, we see an excellent agreement with our initial classification, which works as an intuitive categorisation of the results of Arrigo et al., demonstrating a critical correlation between the morphological parameters. Cell border and cell shape are correlated and give rise to two subcategories:

"polygonal and regular" and "wide with digits". The former corresponds to the plate and dune structures, while the latter corresponds to our fibril classification. In retrospect, and with the insight provided by this extensive investigation, we can conclude that the dune structure can be seen as a type of plate. Of the two more unusual structures, spikes were seen in a single species and could be justifiably included in the hole structure. The leaf structure seems quite exceptional due to its 3D nature; unfortunately, its unusual shape precludes functional imaging, thus excluding it from further studies.

| Name | Cell shape | Cell border | Cell surface | Ridges | Habit | Classification |
|---|---|---|---|---|---|---|
| *Morelia viridis* | wide | **sawteeth** | holes | absence | arboreal | Plate |
| *Naja melanoleuca* | wide | digitation | smooth | absence | terrestrial | Fibril |
| *Naja nivea* | wide | digitation | **holes** | absence | terrestrial | Fibril |
| *Naja samarensis* | wide | digitation | straight | absence | terrestrial | Fibril |
| *Sanzinia madagascariensis* | N/A | sawteeth | holes | absence | arboreal | Plate |
| *Boa constrictor* **constrictor** | polygonal | regular | holes | absence | arboreal + terrestrial | Plate |
| *Corallus hortulanus* | N/A | N/A | **straight** | absence | arboreal | N/A |
| *Bitis arietans* | N/A | **N/A** | **N/A** | **N/A** | terrestrial | Leaves |
| *Crotalus atrox* | polygonal | regular | Straight + **holes** | absence | terrestrial | Dunes |
| *Deinagkistrodon acutus** | polygonal | regular | holes | absence | terrestrial | Holes |
| *Protobothrops elegans** | polygonal | regular | N/A | absence | N/A | Spikes |
| *Daboia russelii* | polygonal | regular | holes | absence | terrestrial | Holes |
| *Philodryas baroni* | wide | digitation | straight | presence | arboreal | Fibril |
| *Pantherophis guttatus* | wide | digitation | **holes** | absence | terrestrial | Fibril |
| *Orthriophis taeniurus friesi* | wide | digitation | N/A | absence | terrestrial | Fibril |
| *Lampropeltis triangulum* **hondurensis*** | wide | digitation | **holes** | absence | terrestrial | Fibril |

**Table 4.2** – Snakes species with a star (*) are not present in Arrigo & al. publication [7], parameters in bold are in disagreement with the publication. N/A corresponds to parameters which could not be clearly estimated from SEM measurements. Arrigo. & al. showed correlation of polygonal with regular and of wide with digits. The former corresponds to the plate and dune structure, whereas the latter corresponds to the fibril classification.

In a few cases, our morphological observations disagree with those of Arrigo et al. In most of these, as shown in Fig. 4.4, the variations come from the gold deposed on the surface, masking some of the finer details of the structure. In other cases, differences arise when AFM topography enables features such as holes to be resolved when they are not distinguishable by SEM only. In the case of *Bitis Arietans*, the structure shown by Arrigo et al. resembles our observation of the cranial part of the scale. This variation could be caused by the age difference between the individuals, leading to a less developed microstructure on the younger individual. With further research, we found that the microstructure of *Bitis Rhinoceros* seems to change depending on whether the scales are black or white [11]. It is possible that *Bitis Aritans* has the same property and could be a subject of further studies. In the case of *Morelia Viridis*, the difference appears to be depending on individual specimens, as no obvious explanation can give a reason for the observed disparity.

In addition to these morphological categories, Arrigo & al. define a simplified habitat classification consisting of four categories: aquatic, terrestrial, fossorial and arboreal. Additionally, they define the following mixed categories: terrestrial+aquatic, terrestrial+fossorial, terrestrial+arboreal. When possible, the same habitat classification was used in our study, since the determination of habitat is complex because most snake species live in large areas encompassing multiple environments.

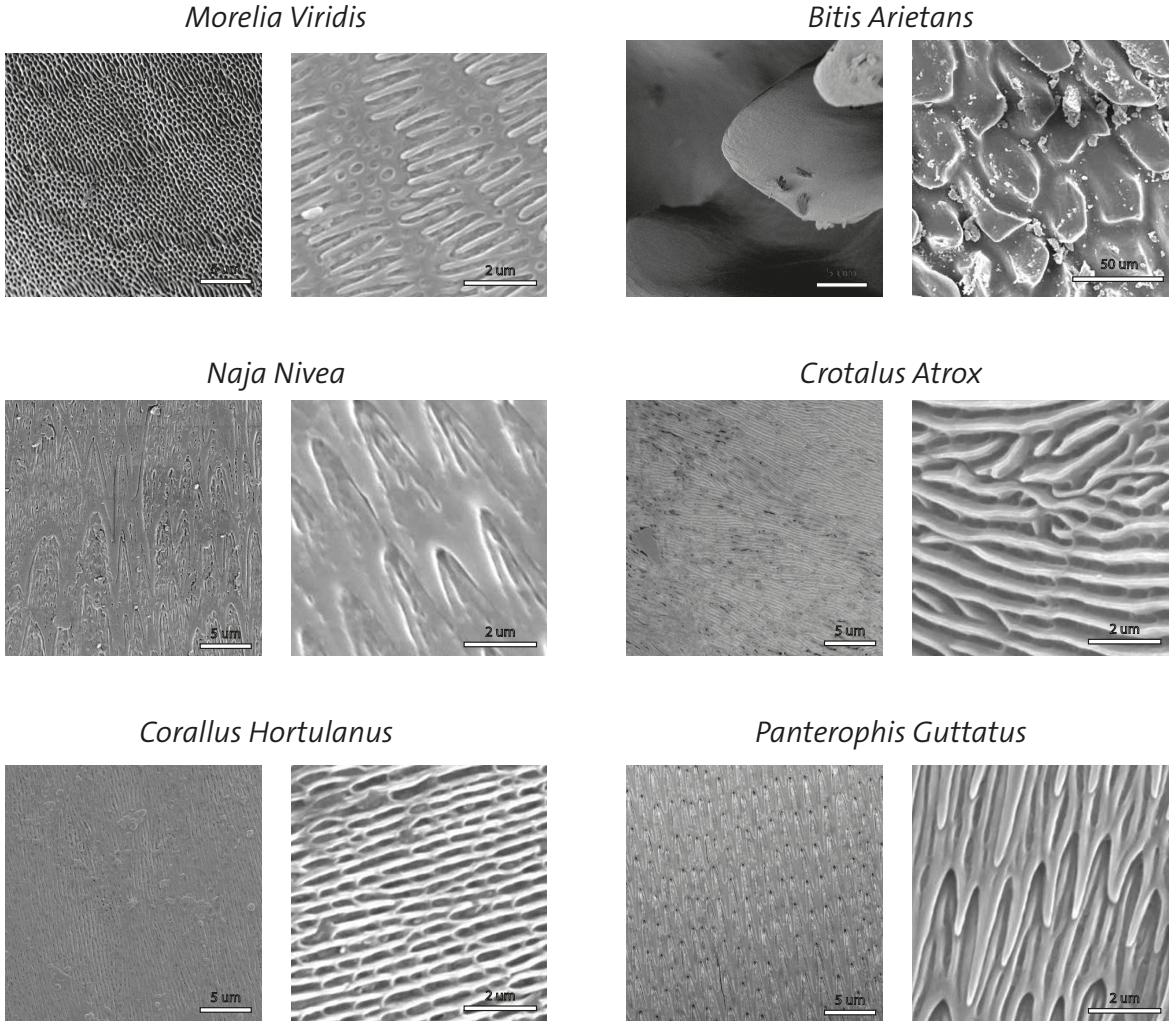


**Figure 4.4** – Comparison of the structures observed in this study (left) with the work of Arrigo et al. [7] (right). The images of *Morelia Viridis* shows significant variations, which are difficult to explain and probably comes from an animal-to-animal basis. For *Bitis Arietans*, structures observed by Arrigo & al. resemble the cranial side structure. The variations observed for *Naja Nivea*, *Crotalus Atrox*, *Corallus Hortulanus* and *Panterophis Guttatus* are mostly due to the deposited gold layer masking fine structures, as finer details can be seen by AFM.

## 4.2 | Nanomechanical and nanotribological properties of snake scale microstructures

Once morphological categorisation of the different microstructures present in our samples was established, our study focused on the nanomechanical and nanotribological properties of the scales. A correlation between the structure and the local mechanical response could potentially confer an evolutionary advantage in particular habitats or in terms of locomotion, leading to a better understanding of snakes at multiple length scales.

### 4.2.1 Young modulus

The Young modulus was measured in order to quantify the local stiffness of the scales. To obtain the elastic modulus at the nanometer scale, we used force mapping: at each point of a regularly spaced grid, a force curve measurement was performed with the AFM and the Young modulus was extracted using the Hertz Model (see chapters 2.1 and 3.4 for more details). This technique allowed us to locally acquire the topography, the stiffness and the tip-sample adhesion in one measurement.

In a first approach, force measurements of the different structures and were used to generate stiffness histograms. As can be seen in Fig 4.5, the histograms from fibril seem to be Gaussian peaks with the presence of shoulders. The low-value peak in the data of *Naja Melanoleuca* and *Crotalus Atrox* is probably caused by bad tip-sample interaction, an artefact due to sudden height changes as can be seen in the inset map. The histograms of plate and dune structures seem to consist of a single peak, indicating no significant variation of the Young modulus.

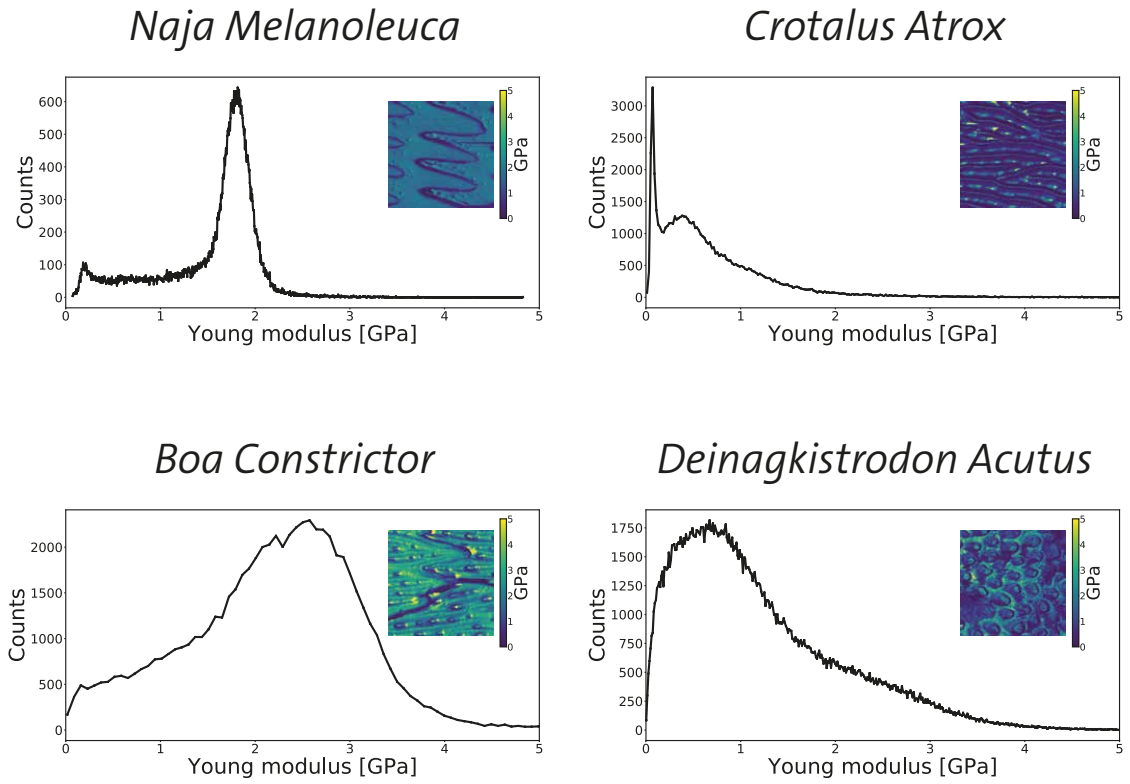


**Figure 4.5** – Histogram representation of the stiffness for some of the different microstructures. All of the histograms show Gaussian behaviour. On *Naja Melanoleuca* there is a left shoulder on the Gaussian peak. The two low-value peaks on *Naja Melanoleuca* and *Crotalus Atrox* are probably due to bad tip-sample contact.

On the digitated structures, we manually defined regions of interest with masks to separate the area of depression from the actual finger-like structure (see Fig 4.6) and searched for correlations between

the shoulder values and the topography. In order to reduce the subjective appreciation of the data, the full histogram of Young modulus was fitted with Gaussian functions without any information about the masked regions. As can be seen in Fig. 4.6, the best Gaussian fit usually consists of two or three peaks, where two are correlated with the masked regions we manually selected. The third peak is correlated with the artefact at low values of the Young modulus. These results lead us to believe that a difference in stiffness between the recesses and the finger-like structures exists.

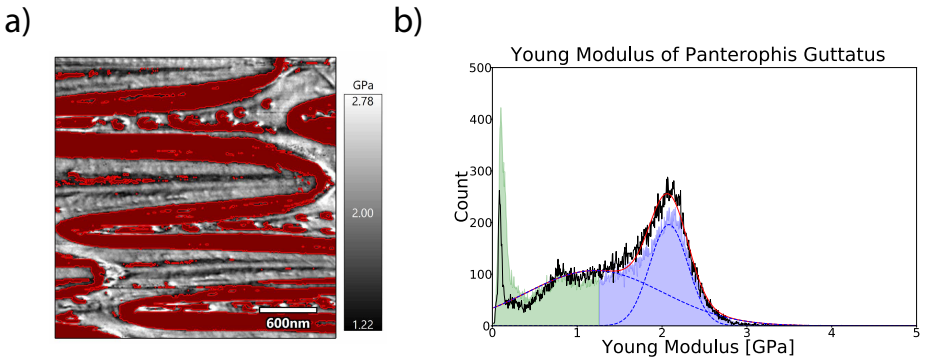


**Figure 4.6** – (a) Young modulus map on *Panterophis Guttatus*, with a mask covering the topographical recesses. (b) Histogram of the stiffness. The green area corresponds to the masked area and the blue to the unmasked one. Two Gaussians were fitted to the whole histogram, without any information on the shaded areas. Gaussian fitting reproduces the effect of the mask, suggesting that at least two regions with different Young moduli coexist within the probed area.

To confirm this observation, the complete dataset consisting of surface topography, stiffness, adhesion, and applied force was combined into a 4-D space with each axis representing a physical property. K-means clustering was then applied to the dataset: clustering data such that each cluster corresponds to a region of similar physical properties (see appendix 6.4 for more details on the algorithm). As k-means requires the number of clusters to be defined by the user, we repeated the calculation with one to five clusters. Most of the significant variations were correctly represented by three clusters, as expected from the previous analysis (see Fig. 4.6).

The result of k-means clustering consists of a spatial map of the clustered regions and four graphs, one per measured physical property. Each graph corresponds to the projection of the clustering along the property axis.

In the case of fibril and hole microstructures, the clustering resulted in regions of different Young modulus, which correlates with the topographical data (Fig. 4.7). In each of the structures, the stiffness seems to be smaller on the border and recesses of the features. A low value of stiffness in the recesses could allow for some flexibility of the digits, allowing them to move laterally if necessary. This hypothesis is supported by the observation of slight movements of the fibrils during contact mode AFM scans with large applied force. Adhesion seems to be higher at the location of hole structures, whereas it is rather homogeneous and small for the fibril structure. A large adhesion could mean that the results produced by the Hertz model cannot be taken as quantitatively correct, especially since the adhesion and stiffness histograms look very similar, which could indicate a possible cross-talk between the two.

For the plate and dune microstructures, clustering does not reveal significant variations of the adhesion or stiffness. However, the overall Young modulus of the dune microstructure seems to be lower than the rest of the structures. This could be due to the assumptions of the Hertz model: as it assumes a constant contact area contact. Due to the elevation variation of the microstructures, the contact surface of the tip with the sample may change significantly during the measurement, resulting in a lower effective Young modulus.

The mean-behaviour of the elastic modulus on different microstructures was also investigated, as we expected a change of the overall modulus on structures with digitation. Looking at the variations between lateral, ventral and dorsal scales on snakes with similar structures, (see Fig. 4.8, *Panterophis Guttatus* and *Naja Melanoleuca*) and comparing them with scales covered by other microstructures, there does not seem to be significant disparity in modulus between the two primary microstructure types (see light-blue and light-green comparison in Fig. 4.8). As can be seen, the overall spread is large (between 0.5 and 3.5 GPa), but the average value of the modulus always lies around 1.6 GPa. Since all microstructures have

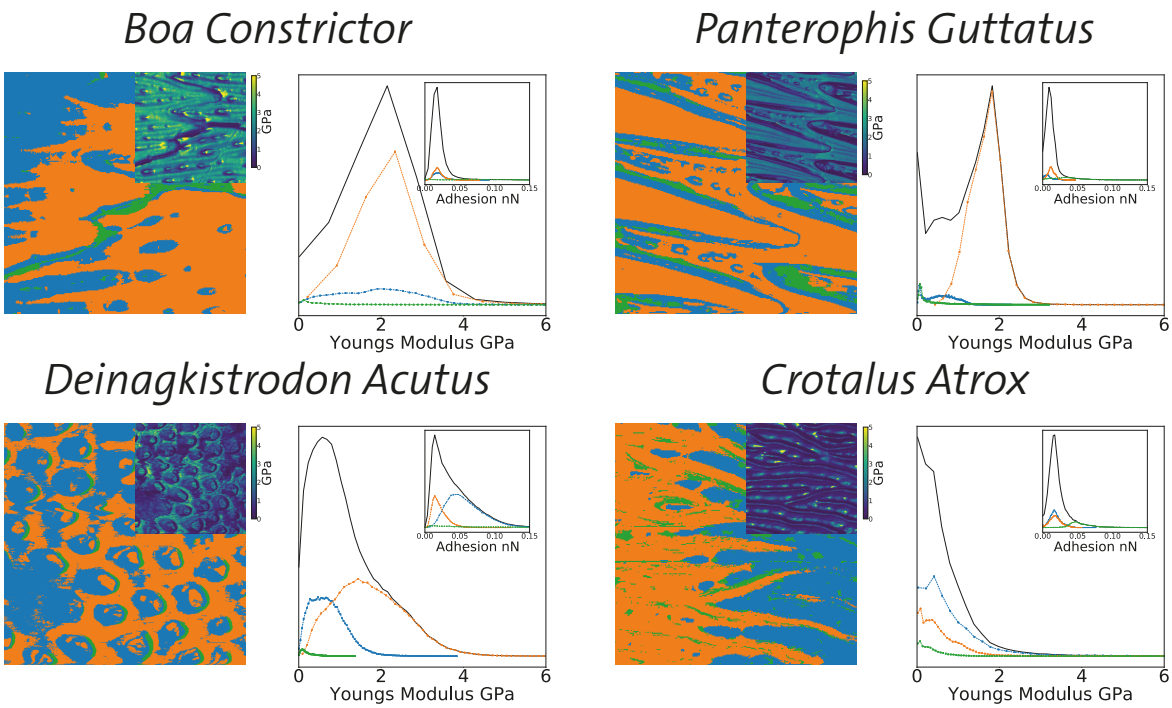


**Figure 4.7** – K-means clustering results, with three clusters. A cut-off was applied for low values of the stiffness to remove the artefacts due to bad tip contact. Each colour of the masked region corresponds to an individual cluster and is associated with a curve on the Young modulus and adhesion plots. Similar looking curves indicate that clustering has selected features along another axis. For example, on *Boa Constrictor* the stiffness and adhesion curves do not show significant variation, as opposed to the measurements performed on *Panterophis Guttatus* and *Deinagkistrodon Acutus*. It should also be noted that the low value of the Young modulus on *Crotalus Atrox* is probably due to bad tip-sample contact. Supplementary measurements can be found in Fig. 6.7.

similar elastic moduli, we presume that the keratinous layers are comparable between the scales, and therefore the observed changes in nanomechanical properties of the microstructures are only due to the micro-scale arrangement.

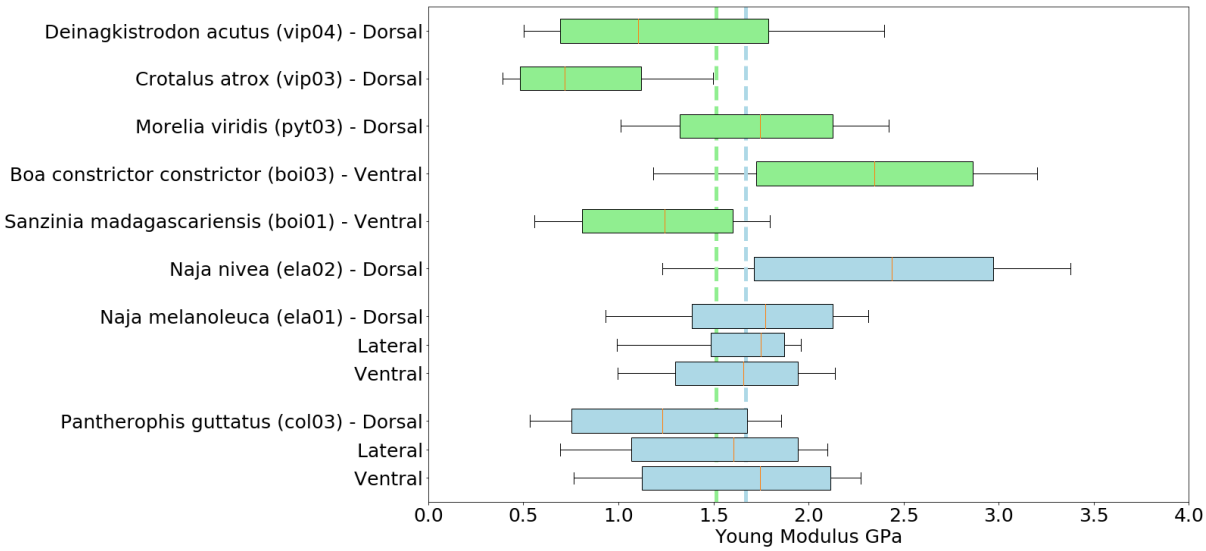


**Figure 4.8** – Comparison of the Young modulus of different snake species and scales. The boxes in blue correspond to structures classified as fibril, the green cover all the other structure types. The dashed lines correspond to the mean value of the fibril (in blue) and non-fibril (in green) structures.

### 4.2.2 Friction coefficient mapping

Although the similarity of the elastic modulus across all scales is not unexpected due to their keratinous nature, a significant difference in the friction coefficients thereon should arise. The fibrils are the cause of the "anti-slip" mechanism which allowing snakes to locomote on tilted surfaces due to the friction anisotropy between forward and backward movement [9]. In this work, we wanted to investigate whether a mechanism at the sub-micrometre scale could complement the microscale mechanism. It was thus necessary to map the frictional properties at a higher resolution than in previous studies. Several AFM-based techniques were employed in this part of the study. First, *Naja Melanoleuca*, a snake with a fibril structure was imaged with the simple lateral force microscopy (LFM) scanning technique. As can be seen in Fig. 4.9, the friction force, defined as the difference in lateral deflection between the backward and forward tip motion, is maximum at the edges of the digits. These results are consistent with literature: the friction coefficient in the forward motion of the snake is lower than the friction in the backward motion [9].

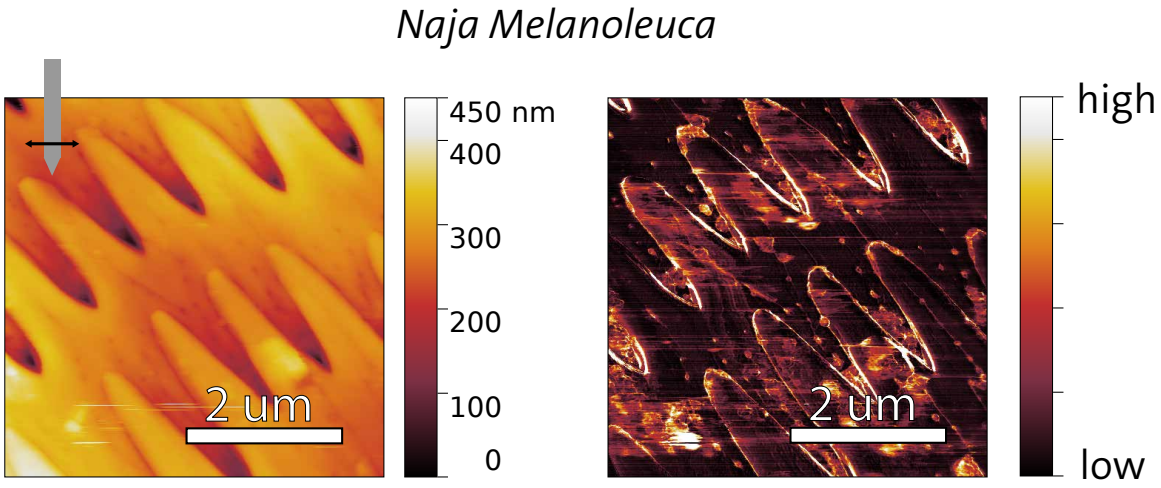


**Figure 4.9** – Lateral force miscroscopy based friction measurement on *Naja Melanoleuca*. As expected the border of the fibrils shows the largest friction response.

However, LFM is prone to cross-talk with topographical features, even more so in the case of snake

scales which exhibit higher elevation compared to the usual samples probed by AFM. Therefore it was necessary to probe our samples with other techniques designed to reduce the cross-talk: band-excitation and bending-oscillation (see Chap. 3.4.2). As it was the first time these techniques were used in our research group, they were first benchmarked on a sample of PS-LDPE, a two-component polymer known to give excellent contrast in mechanical property measurements.

While the results on the PS-LDPE and HOPG shown in Figs. 3.13 to 3.15 appeared promising for the detection of regions with varying friction coefficients, the results on snake scales are not as clear as expected. As can be seen in Fig. 4.10, while amplitude variation not visible in the corresponding topography maps is present in all measurements, it does not seem to be linked to any obvious friction feature which would lead to an evolutionary advantage. On *Naja Melanoleuca* and *Panterophis Guttatus*, most of the features are in fact caused by small scratches on the scales, additionally to the contrast expected at the digit edges. On *Deinagkistrodon Acutus*, the features appear to be linked to the underlying alignment of keratin fibres, as a layered structure is visible inside the holes. Additional features with very high or very low amplitude are also due to surface contamination or spurious tip-sample interaction and can be linked visually to topographic features.

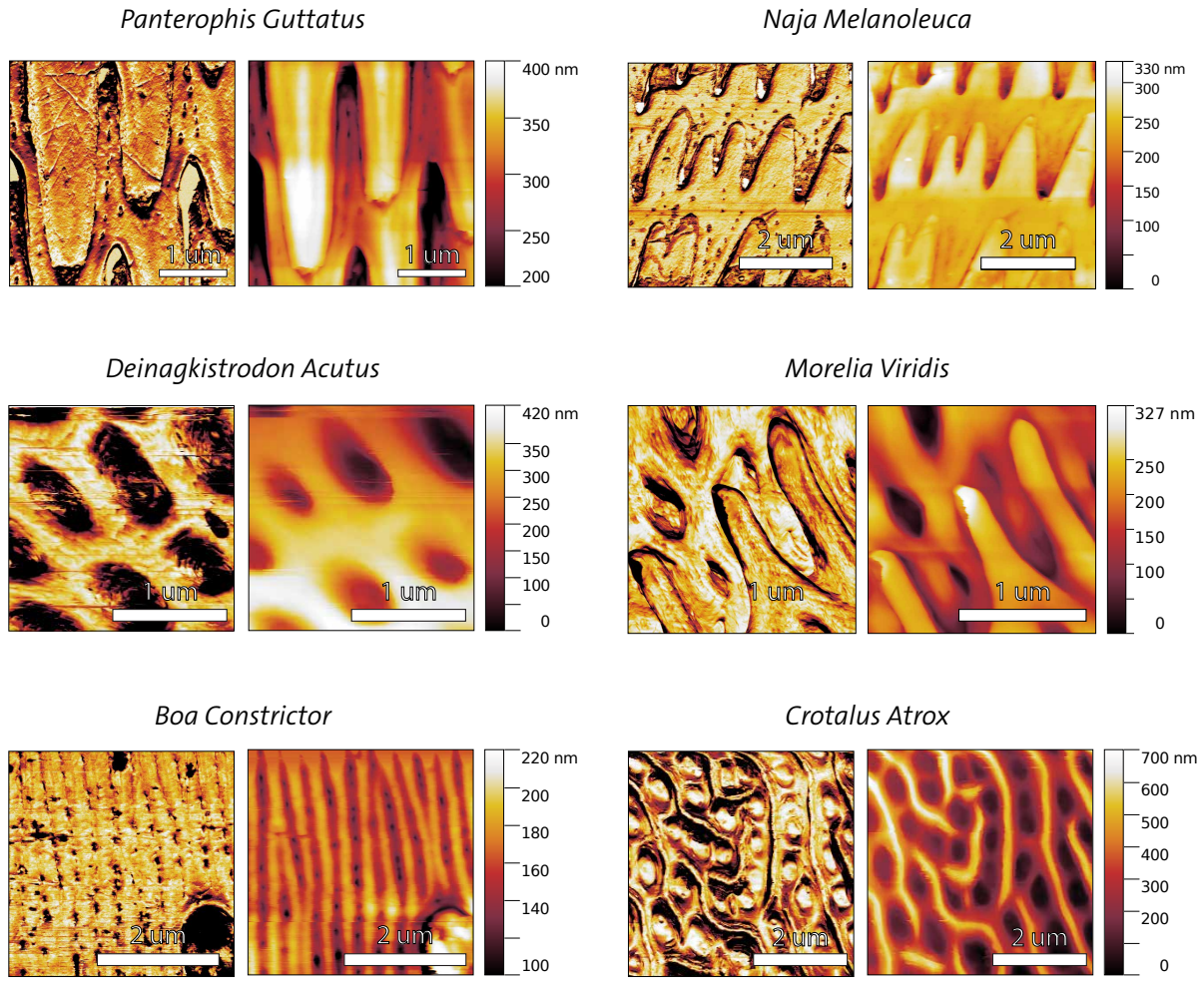


**Figure 4.10** – Amplitude (left side) and topography (right side) for different species of snakes. On the *Panterophis Guttatus* and *Naja Melanoleuca* structures, streak-like features on the amplitude images are probably caused by scale damage. On *Deinagkistrodon Acutus* and *Morelia Viridis*, the features seem to reveal the underlying keratin structure. On *Boa Constrictor* and *Crotalus Atrox*, the amplitude features seem to be directly linked to topographic variations.

## 4.3 | Wettability measurements

While the ventral and lateral scales are mainly structured in fibrils or plates, the dorsal scales exhibit more structural diversity. They are probably not linked to motion optimization, but might produces other advantages, such as self-cleaning properties or improved camouflage due to the interaction of light with microstructures [11, 48]. However, the most apparent benefit of these microstructures is water repulsion, as has been shown on multiple kind of animals whose surface microstructures give rise to iridescence and hydrophobicity [49].

As discussed in section 2.3, wettability measurements do not give the exact contact angle $\theta_W$ but an angle in the range $[\theta_A, \theta_R]$. However, the development of a shaking stage to improve the precision would have gone too far from the scope of the project. Therefore multiple measurements of contact angle on each scale were performed, and despite variations of the order of tens of degrees, it was still possible to extract meaningful information from these simple measurements.

First of all, we looked at the time evolution of water droplets on the scales. Once a droplet had stabilized, we observed that its shape did not evolve for at least two minutes, after which the evaporation started to become significant, and the angle of contact reduced (see Fig. 4.11).

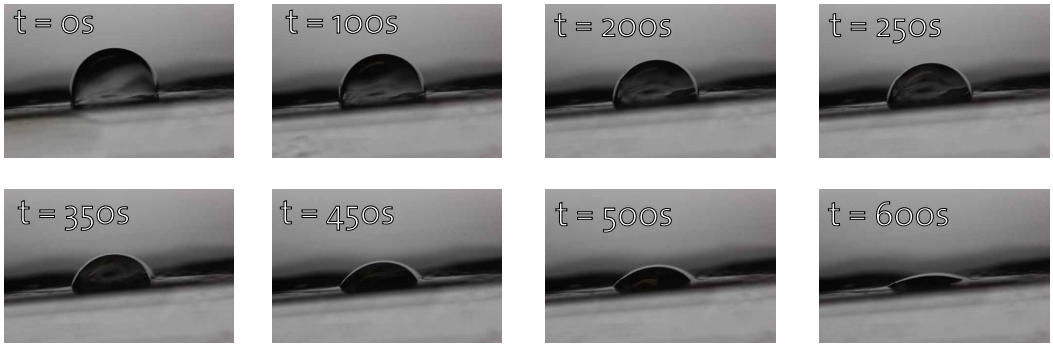


**Figure 4.11** – Time evolution of the shape of the droplet on the skin of *Naja Melanoleuca*. The droplet keeps roughly the same shape for up to 200s. The apparent surface tilt was due to the camera alignment.

Overall, measurements on snake scales were challenging for two reasons, leading to high uncertainties:

- It was observed that the droplet often rolls on the surface before stabilizing, leading to a slight decrease in the contact angle.
- On the smaller scales, the droplet was of similar size of the scale, leading to its interaction with the scale edges.

Additionally, multiple measurements were performed from the front and from the side of the individual scales and no anisotropy of the contact angle was found. We also compared the shape of the droplet on bare and gold-coated scales, to investigate whether the observed contact angles were only due to the sample microstructures. As can be seen in Fig. 4.12, on *Naja melanoleuca*, *Daboia russelli* and *Boa constrictor*, a small reduction of the contact angle on the gold-plated samples is visible compared to the bare scales. On *Crotalus Atrox*, *Deinagkistrodon acutus* and *Protobothrops elegans* the gold-plated scales became so hydrophilic, that contact angle were not measurable. Looking back at the Cassie-Baxter model, a change from keratin to gold could lead to the transition from the configuration with air pockets, to the fully wet configuration.

All of the bare snake scales exhibit a hydrophobic behaviour, with contact angles higher than 90 degrees. From all these snakes, *Daboia Russelli*, *Crotalus Atrox* and *Prothobothrops elegans* are the one exhibiting the largest contact angle, and all three have dorsal scale differing from the ventral scale one.

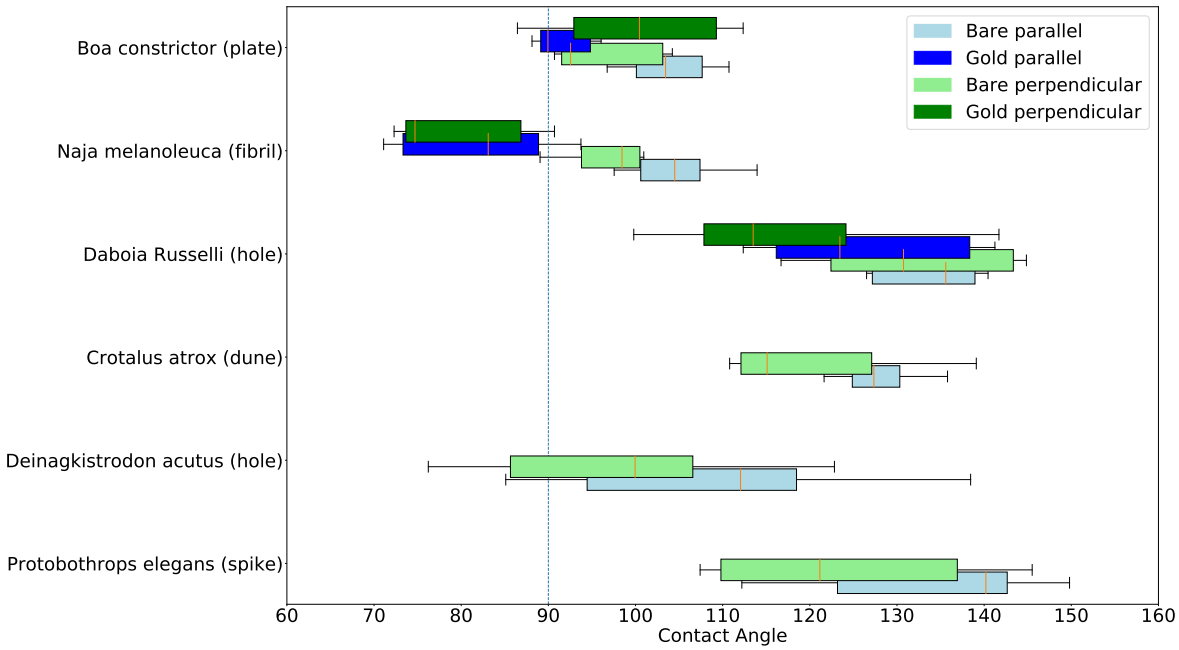


**Figure 4.12** – Comparison of the contact angle for different species and microstructures. Overall, bare samples show hydrophobic behaviour. No clear effect of the anisotropy is visible. The gold coating seems to reduce the hydrophobicity of the samples, leading to hydrophilicity on *Crotalus atrox*, *Deinagkistrodon acutus* and *Protobothrops elegans*.

## 4.4 | Pyroelectricity

The snake scale structures investigated in this work possess a preferred orientation. For biological structure, the presence of a dipolar moment in its constituents can be the cause of an anisotropic growth[2]. Pyroelectric measurements can probe such dipolar moment since a variation of temperature leads to a change in polarization, which in turn results in the production of current. In order to measure the pyroelectric coefficients along the different directions, cross-shaped gold contacts were deposited on top of a *Naja Melanoleuca* scale, and a single electrode at the bottom of the scale (see Fig. 3.19 for a schematic representation). Pyroelectric measurements were then performed in collaboration with Prof. Dragan Damjanovic at the EPFL. Initial measurements were performed along the growth axis of the scale microstructure. SEM images were used to compute the surface area of the electrodes. The electrodes deposited are one millimetre wide circles (see Fig. 4.13), as expected by the size of the drill used to produce the shadow mask. As can be seen in Fig. 4.14(a), the resulting current seems to be uncorrelated with temperature, with values just above the amplifier noise level. To improve the signal-to-noise ratio, the data was averaged over five temperature cycles, (Fig. 4.14(b)) yielding a pyroelectric coefficient of $p = 3.82 \cdot 10^{-2} \left[\mu C m^{-2} K^{-1}\right]$.

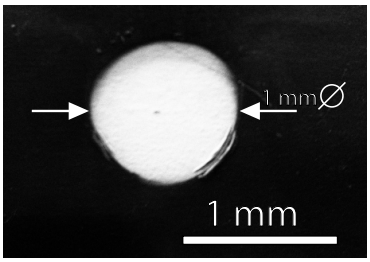


**Figure 4.13** – Image of the electrod size to determine the surface for the pyroelectric measurement.

In comparison, ferroelectric materials usually have pyroelectric coefficient ranging from 50 up to 5000 $\left[\mu C m^{-2} K^{-1}\right]$, whereas the non-ferroelectric pyroelectrics have values of $5 - 150 \left[\mu C m^{-2} K^{-1}\right]$ [50].

The obtained pyroelectric coefficient is almost non-existent, even from what is expected from a non-ferroelectric material. Additionally, the current signal was close to the noise level, leading to a bad signal-to-noise ratio. The sample preparation could have been improved by increasing the electrode area, thus increasing the current. However, this would have been at the expense of the spatial characterization of the pyroelectric coefficient, as we would not have been able to distinguish between $p_{xx}, p_{yy}, p_{zz}$. In the end, we choose not to pursue this part of the investigation due to the low pyroelectric coefficient of the preliminary observation and the time constraints of this project.

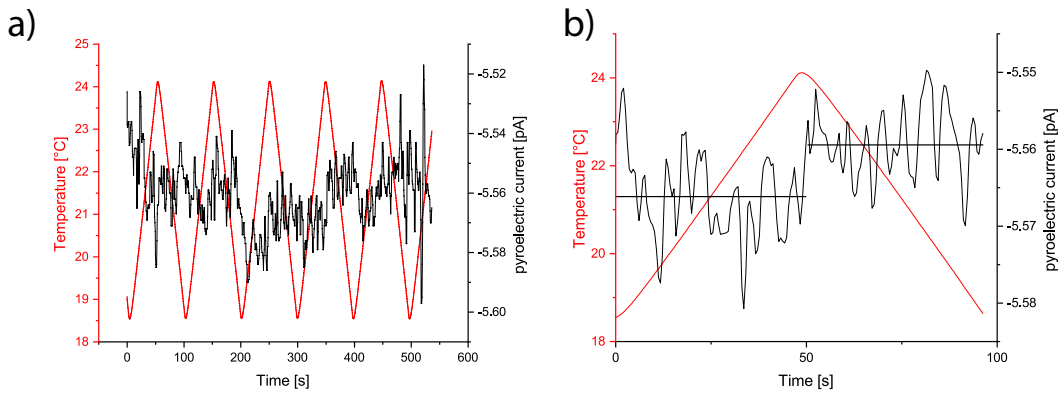


**Figure 4.14** – (a)Full data over five cycles with $\Delta T = 5^{\circ}C$ over $50s$. The pyroelectric signal is just above noise level. (b) Current and temperature averaged over the five cycles, revealing a current offset between the positive and negative temperature ramps, leading to a pyroelectric coefficient of $p = 3.82 \pm \cdot 10^{-2} \left[\mu C m^{-2} K^{-1}\right]$

[2]It should be noted that polarity is not the only mechanism causing anisotropy. For example, a strain can also cause anisotropic growth

# 5 Conclusion

Throughout this project, we analyzed the scale microstructure of sixteen species of snakes by using SEM and AFM techniques. Based on the SEM measurements, we defined six classification groups of snake scale microstructures, which present similarities with the classification in Arrigo & al.'s paper [7].

We also successfully implemented two novel SPM techniques, extending the capabilities of our laboratory: fast force mapping and dynamic friction. As part of this study, these techniques allowed us to probe the mechanical properties - stiffness, adhesion and friction coefficient - of snake scales at the nanoscale. Through the use of K-means clustering, a simple data mining algorithm, we found regions with local variations of the Young modulus. However, interpretation was hindered by the complex topographical features of the scales, inducing cross-talk between topography and stiffness measurements, through the varying tip-sample contact area. Further studies are necessary to confirm that the measured properties are not caused by sample elevation, for instance by using colloidal probes. Frictional measurements highlighted features which did not appear on the topographical images, leading us to believe that the technique successfully decorrelated the topography from the frictional properties. However, the lack of clear indications of evolutionary adaptations is visible on the structures, leading us to believe that the friction anisotropy does not come from the sub-micrometric features. Beyond the scope of this study, these two techniques could lead to novel measurements on the mechanical properties of functional materials such as ferroelectrics, such topics being the main focus of our research group.

Going beyond the measurement of mechanical properties, we probed the interaction of water with the scales. Since the measurements of the precise contact angle require the measure of the receding and advancing angle, the complete analysis of the wetting properties could have been a project in itself which would have required the development of a new experimental setup. However, the values resulting from our brief analysis of the resting angles indicate that all the structures are hydrophobic, and lead us to believe that the dorsal structure has a slightly better hydrophobicity.

Finally, with the help of Prof. Damjanovic (*EPFL*), we tested the snake scales for the presence of a significant pyroelectric coefficient, in the hope to find an explanation for the highly anisotropic structural arrangement. However, these results were not conclusive with extracted pyroelectric coefficients being arguably just above the noise level of the system.

In summary, snake scales are complex and varied structures with material properties at the edge of multiple research fields: physics and biology; bulk and interface physics; macroscopic and nanoscale physics. Such a combination could lead to novel materials, for instance through biomimetism or their integration into materials design processes. A fundamental understanding of their structure and properties can moreover further our understanding of snakes from a biological point of view.

Were the project to continue, further studies would focus on a deeper understanding of the nanoscale stiffness, for instance by using colloidal probes to make sure that the signal is not due to topographic cross-talk. The study would additionally be extended to a larger variety of snakes, especially ones living in fossorial or aquatic habitats. Since the sheds dry quickly after moulting, the control of shed water content by rehydration could also lead to interesting results.

# 6 Annexes

## 6.1 | Deformation free energy development

We start from the expansion of the free energy in term of the strain tensor components:

$$F = F_0 + \frac{\lambda}{2}\left(\sum_i u_i i\right)^2 + \mu \sum_{ik} (u_{ik})^2 \tag{6.1}$$

This equation can be rewritten in a more elegant form by splitting the strain tensor into two parts: one where the diagonal elements are zero and one fully diagonal. The former corresponds to shear, where the deformation does not affect the volume of the object, and the latter corresponds to a deformation where the shape of the object stays constant and only the volume change.

$$u_{ik} = \left(u_{ik} - \frac{1}{3}\delta_{ik}\sum_l u_{ll}\right) + \frac{1}{3}\delta_{ik}\sum_l u_{ll} \tag{6.2}$$

We first expand $u_{ik}^2$:

$$\begin{aligned} u_{ik}^2 &= \left[\left(u_{ik} - \frac{1}{3}\delta_{ik}\sum_l u_{ll}\right) + \frac{1}{3}\delta_{ik}\sum_l u_{ll}\right]^2 \\ &= \left(u_{ik} - \frac{1}{3}\delta_{ik}\sum_l u_{ll}\right)^2 + \frac{2}{3}\delta_{ik}\left(u_{ik} - \frac{1}{3}\delta_{ik}\sum_l u_{ll}\right)\sum_l u_{ll} + \frac{1}{9}\delta_i k\left(\sum_l u_{ll}\right)^2 \\ &= \left[u_{ik}^2 + \frac{1}{9}\delta_{ik}\left(\sum_l u_{ll}\right)^2 - \frac{2}{3}\delta_{ik}u_{ik}\sum_l u_{ll}\right] + \frac{2}{3}\delta_{ik}u_{ik}\sum_l u_{ll} - \frac{1}{9}\delta_{ik}^2\left(\sum_l u_{ll}\right)^2 \\ &= \left[u_{ik} - \frac{1}{3}\delta_{ik}\sum_l u_{ll}\right]^2 + \frac{2}{3}\delta_{ik}u_{ik}\sum_l u_{ll} - \frac{1}{9}\delta_{ik}^2\left(\sum_l u_{ll}\right)^2 \end{aligned} \tag{6.3}$$

and insert it into the free energy equation (6.1):

$$\begin{aligned} F &= F_0 + \mu\sum_{ik}\left(u_{ik} - \frac{1}{3}\delta_{ik}\sum_l u_{ll}\right)^2 + \frac{\lambda}{2}\left(\sum_l u_{ll}\right)^2 + \frac{2\mu}{3}\sum_{ik}\delta_{ik}u_{ik}\sum_l u_l l - \frac{\mu}{9}\sum_{ik}\delta_{ik}\left(\sum_l u_{ll}\right)^2 \\ &= F_0 + \mu\sum_{ik}\left(u_{ik} - \frac{1}{3}\delta_{ik}\sum_l u_{ll}\right)^2 + \frac{\lambda}{2}\left(\sum_l u_{ll}\right)^2 + \frac{2\mu}{3}\sum_i u_{ii}\sum_l u_{ll} - \frac{\mu}{9}\sum_i\left(\sum_l u_{ll}\right)^2 \\ &= F_0 + \mu\sum_{ik}\left(u_{ik} - \frac{1}{3}\delta_{ik}\sum_l u_{ll}\right)^2 + \frac{\lambda}{2}\left(\sum_l u_{ll}\right)^2 + \frac{2\mu}{3}\left(\sum_l u_{ll}\right)^2 - \frac{3\mu}{9}\left(\sum_l u_{ll}\right)^2 \\ &= F_0 + \mu\sum_{ik}\left(u_{ik} - \frac{1}{3}\delta_{ik}\sum_l u_{ll}\right)^2 + \left(\frac{\lambda}{2} + \frac{1\mu}{3}\right)\left(\sum_l u_{ll}\right)^2 \end{aligned} \tag{6.4}$$

By defining $K = \lambda + \frac{2}{3}\mu$, we finally obtain the usual form of the free energy, where each term corresponds to pure hydrostatic compression or pure shear:

$$F = F_0 + \mu \sum_{ik} \left( u_{ik} - \frac{1}{3}\delta_{ik} \sum_{l} u_{ll} \right)^2 + \frac{K}{2} \left( \sum_{l} u_{ll} \right)^2 \tag{6.5}$$

with $\mu$ the shear modulus and $K$ the bulk modulus.

## 6.2 | Humidity Controller

This section is based on the work done in the summer preceding this project. It was done in collaboration with Dr. Iaroslav Gaponenko and has been submitted to *Engineering Research Express* [45].

### 6.2.1 Working principle

The humidity controller presented here operates on a flow-mixing principle. A flow of dry nitrogen gas is split in two at the inlet and injected into two mass flow controllers (MFC). The output of the first MFC is then circulated through a chamber containing a water-saturated atmosphere provided by an ultrasonic nebulizer. The humidified flow is then recombined with the output of the second MFC, allowing for smooth control of moisture in the system under consideration from fully dry (0 %RH) to water-saturated (100 %RH)[1]. A first sensor measures both the relative humidity and temperature of the flow as close as possible to the mixing point, with the values used for the active feedback loops in the software. The resulting flow is then circulated in the experiment. When possible under experimental design considerations, a second sensor can be used to monitor the humidity and temperature of the output flow, allowing the user to visualize the stabilization and transient humidity changes that can occur due to icing, evaporation, or condensation.

At the heart of the system lies a *Raspberry Pi* microcomputer, with the Python-based control software performing the following tasks:

- Sensor parameter acquisition (temperature and humidity of the flow towards and from the system under test)
- Mass flow controller flow regulation (wet and dry flow ratio, keeping the total flow constant)
- Data recording (local file containing all system parameters and sensor values)
- Communication with a remote user interface through a web-based API

A user interface developed in *.NET* is used to operate the humidity controller remotely through the web-based API, allowing an interactive visualization of the sensor and flow values, as well as control of the various subsystems (fans, PID, nebulizer). Moreover, the interface possesses a miniature JavaScript interpreter, allowing the user to script and automate humidity control through the use of an interpreted language.

### 6.2.2 Hardware implementation

The humidity controller has been designed with standalone operation and portability in mind. The system whose humidity is to be regulated only needs to be connected through a pneumatic inlet/outlet pair in series with the controller, the latter performing regulation independently based on integrated injection and exhaust sensors. The internal layout of the controller is shown in Fig. 6.1(a), as assembled inside a rack-mount unit. The front and back plates provide for electrical, digital and flow access. The hardware implementation of the various subsystems of the controller is described in more detail below, and detailed schematics of the assembly and bill of materials are available online [51].

#### Electrical distribution, signaling, and control

The electrical distribution, analog/digital control and sensing pathways are shown in Fig. 6.1(b). At the heart of the system lies a *Raspberry Pi* microcontroller, running the software, and interfacing the various AD/DA converters, relays, digital potentiometer, RH/T sensors and the mass flow controllers through dedicated wiring. It interfaces to the remote control GUI through an ethernet port, and local control is possible through the use of frontal USB and HDMI ports. A line-input AC-DC converter provides power distribution to the system with 5 V/12 V/24 V outputs.

Although digital communication has been favored for most subsystems (relays, potentiometer, sensors), an AD/DA board has been selected to interface the analog setpoints and readouts of the mass flow controllers to maintain universality and reduce the dependence on a single manufacturer for the highest cost parts. While this decision resulted in a limited granularity of the flow control, no notable effects on the stabilization process were observed.

[1] The specific values depend on the ambient temperature and the dryness of the input flow

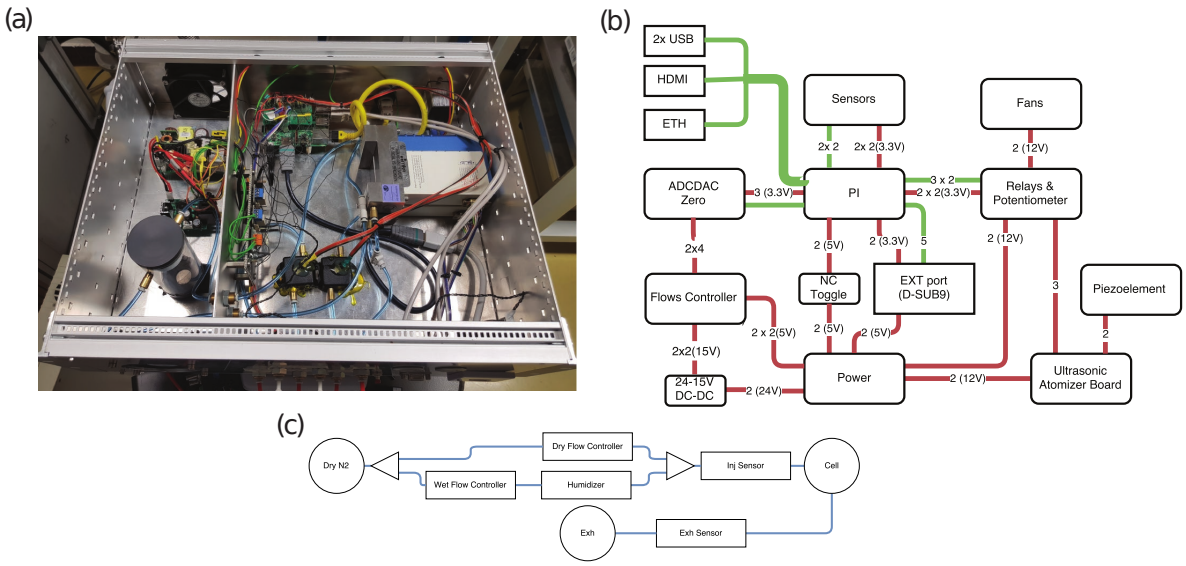


**Figure 6.1** – (a) Standalone humidity controller mounted within a standard rackable unit. The front and back panels provide access to the power/digital and gas flow input/output lines. The nebulizer chamber fill-port is accessible from the top. (b) Electrical/digital wiring diagram, designed for the controller to be operated with at minimum a single power line input. (c) The diagram of the gas flows and humidification apparatus. A single input provides the dry gas, and a combination of outlet/inlet allows the measured system to be connected in series. The outlet port can be used to vent the linear gas flow. An auxiliary humidifier outlet/inlet is provided for potential external humidification apparatus.

### Flows, humidification and sensing

The gas flows through a pneumatic tubing network, as shown in Fig. 6.1(c). Dry air is provided to the system via a pass-through quick-release connector on the back-plate. The flow is then split into two and regulated by two mass flow controllers, with one flow passing through a humidification apparatus to reach full saturation. The dry and wet flows are then combined, their humidity/temperature measured, and the resulting flow is injected into the measurement system. The total flow is thus kept constant, and the ratio of the wet to dry flows will determine the resulting relative humidity. If the system is hermetically connected in series with the controller, its exhaust flow is collected, its humidity/temperature measured before ejection through a back-plane quick-release connector.

The design presented here makes use of an ultrasonic nebulizer, which we have previously demonstrated to prevent mechanical noise from affecting the system while achieving a fast stabilization rate through the full humidity range [44]. A different humidification system may be used instead - a bubbler for instance - through the provisioned auxiliary connectors on the back-plate.

Sensing of the humidity and temperature is done at two locations of the flow: just past the point of mixing of wet/dry flows (hereafter referred by $INJ$, and measuring $T_{inj}$ and $RH_{inj}$), and at the return of the flow from the system under investigation (hereafter referred by $EXH$, and measuring $T_{exh}$ and $RH_{exh}$). The monitoring of the exhaust parameters is vital, as it provides information on the dynamic processes that take place within the measurement chamber. It is, for instance, possible to detect evaporation, condensation, and icing by comparing the flows and temperatures at the two points. A third sensor can be attached to the controller for calibration, $T_{cell}$ and $RH_{cell}$, and is discussed in the corresponding section below.

The typical total flow that the system has been designed to handle ranges from 500 to 20000 sccm. Tested volumes of measurement systems ranged from 5 to 100 ml, but a higher capacity is expected to increase the stabilization time. Better results are obtained when the exhaust tubing has a similar length to the intake tubing, that is the connection between the $INJ$ and $EXH$ sensors.

### 6.2.3 Software implementation

The software is based on a client-server architecture, with the server written in Python and running on the *Raspberry Pi*, and the client user interface written in .NET running on a network-connected computer and interfaced through a REST/JSON API. The source code and compiled files for both are available online [51].

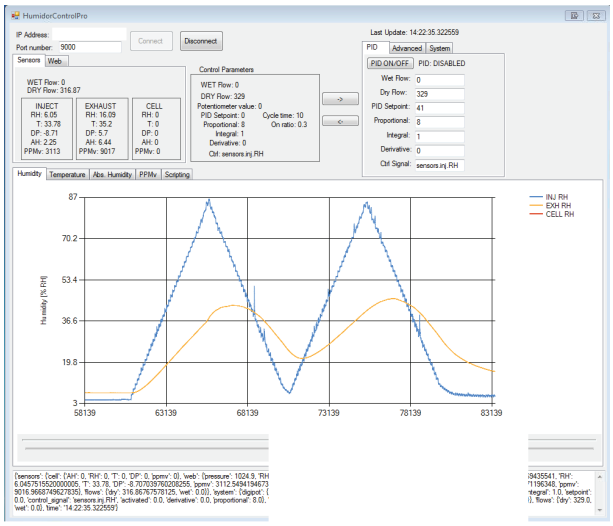


**Figure 6.2** – Client-side graphical user interface for the humidity controller written in .NET. A graph control displays the time evolution of the different parameters, and the toggles and inputs enable the control of various subsystems of the controller. The communication uses a REST/JSON interface with a client-server architecture.

#### Server-Side

The server-side software is segmented into nine different processes that run in parallel and that access a shared memory containing the last state of the controller - sensors, flows, setpoints, etc. This architecture prevents memory leaks, as no more than a single state is stored in memory at any time.

1. **p_webServer** The communication with the remote user interface is performed through a simple web server exposing a REST/JSON API to interact with the shared memory. Specifically, the remote client can both read and write any of the values at any given time, enabling direct control of the subsystems below.

2. **p_flows** The flow control thread's sole mission is to handle the interaction with the mass flow controllers. To this effect, it continuously polls the shared memory for the values of the wet/dry flow setpoints and sends these values to the mass flow controllers if the values differ from its internal memory. The values of the flows may either be changed manually by the remote API commands to write the shared memory or internally by the PID subsystem. Moreover, the flow control thread is also in charge of reading the current flows going through the mass flow controllers. In the current implementation, the flows are acquired and set through AD/DA converters to maintain universality across mass flow controller brands.

3. **p_pid** The PID control thread - when activated through the corresponding shared memory flag - will regulate the flow outputs to reach a specific sensor setpoint. The sensor to be used as a setpoint as well as the specific setpoint value are contained in the shared memory, with the former defaulting to the $RH_{inj}$ signal. The PID gains can also be changed through interaction with the shared memory through the REST/JSON API.

4. **p_sensors** Running on a separate clock from the other threads due to the averaging time required by RH/temperature sensors, the sensor acquisition thread will continuously update the latest $RH_{inj}$, $T_{inj}$, $RH_{exh}$, $T_{exh}$, $RH_{cell}$ ,and $T_{cell}$ values. It also performs the calculation of the absolute humidity, dewpoint and parts per million (volume) for each sensor. Each value is stored in the shared memory, for use

by other processes.

5. **p_webAcquisition** As some of the calculations performed by the thread above require knowledge of the atmospheric pressure, a website containing real-time meteorological information is acquired by this thread every minute and parsed to extract the current data. The resulting meteorological conditions are then updated in the shared memory.

6. **p_potentiometer** A potentiometer is necessary to regulate the power of the nebulizer, and digital control is implemented through this thread. As soon as the corresponding shared memory value is changed, it is sent to the digital potentiometer - thus varying the density of mist in the atomizer.

7. **p_pwm** A pulse width modulation subsystem has been implemented to preserve the durability and reduce the heating of the ultrasonic nebulizer, as well as to reduce the production of water droplets in the circuit which can produce humidity peaks. When enabled through the shared memory, it will start a timer and modulate the value of the atomizer relay shared memory value at a given on/off ratio over a specific delay.

8. **p_relays** This process monitors for changes of relay states in the shared memory and sends the updated state to the corresponding relays. Currently, two relays have been implemented: atomizer on/off and fan on/off control. In the current implementation, pulses sent to *Raspberry Pi* GPIO pins are used to set or reset external latching relays.

9. **p_writeFile** As there is only a single state present in memory at a given time, it is vital to record it to disk as soon as any changes occur. This thread will thus monitor the shared memory for changes, and continuously record the complete memory onto the disk in the form of a comma-separated values file with timestamps for further processing.

#### Client-side

A client-side user interface has been implemented for monitoring and control of the humidity controller. The interface, written in .NET for Windows, is shown in Fig. 6.2. Specifically, it queries the REST/JSON API provided by the web server and displays numeric indicators and plots a time graph of the humidities, temperatures and various other values of the shared memory. Toggle switches allow the PID, PWM or relays to be turned on and off, and input boxes enable the setting of all parameters in the shared memory.

#### Scripting interface

A scripting interface has been developed to enable easy automation and interfacing of the humidity controller in conjunction with the user interface. A JavaScript engine with custom commands enables target behavior to be scripted just by sending a list of commands directly to the controller. The scripts we developed take the form of a finite state machine, and range from simple PID control to humidity ramps and pulse trains. The graphs in the calibration section below have been produced by scripting specific controller behavior. Example scripts are available online[51].

### 6.2.4 Calibration and testing

As the dynamical response of each system under measurement is different and a humidity/temperature sensor may not be readily available or even practical, we have implemented a simple method to calibrate the humidity/temperature values from the measurement system versus the values at the $INJ$ sensor. For this, a third sensor, $CELL$, is tethered to the controller and placed in the measurement system or an equivalent hermetic volume with an inlet and outlet port. A software toggle switch is available in the user interface to enable the acquisition of this sensor, and the controller can then be calibrated through pulse and ramp scripts.

To determine the difference in behaviour between the $INJ$ and $CELL$ locations, $AH_{cell}$ was measured at the end of the stabilization of multiple $AH_{inj}$ setpoint values, as shown in Fig. 6.3(a). From this test, we concluded that the relation between the cell and injection absolute humidity is linear after enough time has passed for stabilization to occur, with a slope of 0.95 and a y-intercept of 0.57, as shown in Fig. 6.3(b). The fit values can be changed in the GUI, allowing the use of multiple volumes and types of systems with the controller. Moreover, if a sensor can be placed inside of the system under test and tethered to the controller, this calibration is not necessary since the PID controller can directly be driven by that sensor.

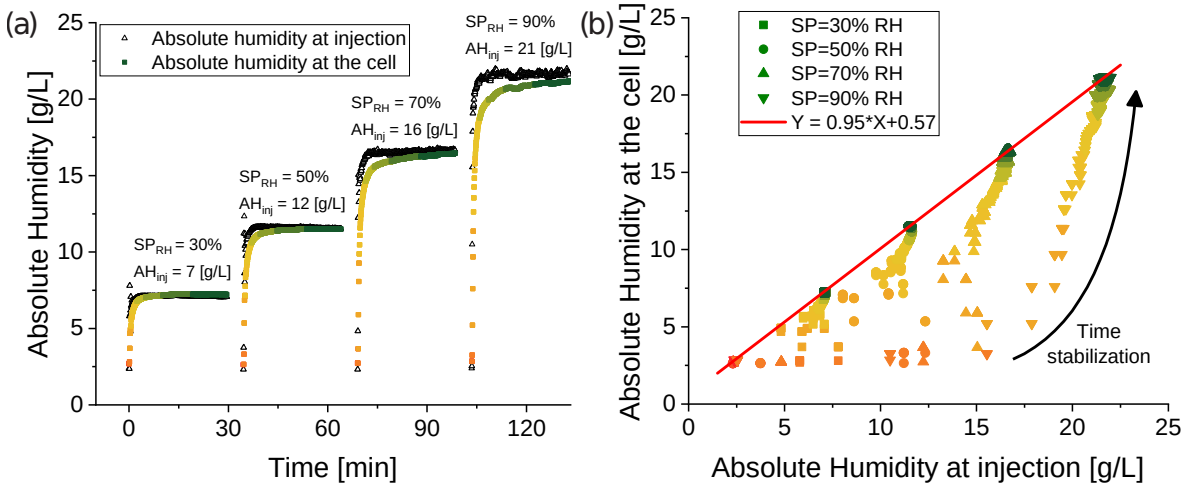


**Figure 6.3** – (a) Absolute humidity as a function of time at the $INJ$ and $CELL$ points shows a gradual stabilization once the setpoint has been applied to the PID. (b) The $CELL$ versus $INJ$ absolute humidity show a linear relationship after having been allowed to stabilize. The linear relationship can be used to extrapolate the humidity within the system under test when a tethered sensor is not available.

The complete range of the attainable relative humidities depends on the temperature as well as on the inlet gas humidity. Typically, the most conservative range that can be guaranteed is between 10% RH with a full dry and 90% RH with a full wet flow. The stabilization time will depend on the differential, but will typically vary between a few minutes for the smallest steps to a few hours for the largest. Some spikes in the humidity may appear due to water bubble transport through the humid air line, but these are effectively smoothed due to the PID reaction time.

The stability of the humidity with the PID turned on is usually below 0.5% RH, and drifts of more than 1% RH can be observed when the PID is turned off, as illustrated in Fig. 6.4.

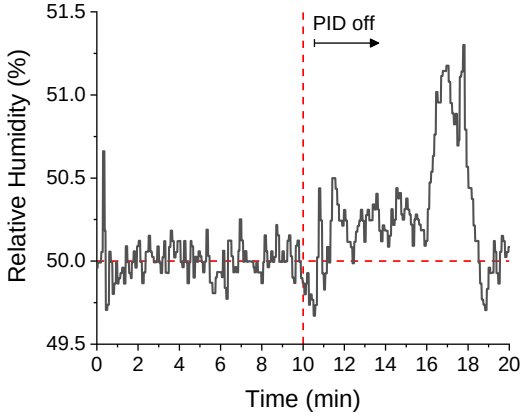


**Figure 6.4** – The humidity setpoint was fixed at 50% relative humidity using the PID controller. After ten minutes, the PID was turned off, and the humidity was left to drift freely. After only a few minutes without the PID control, the humidity had drifted more than a percent.

An illustration of this stability and stabilization speed can be seen in Fig. 6.5, where a humidity pulse train was applied by the use of the scripting interface. Specifically, three two-hour cycles were performed by alternating a 10% RH setpoint with a sequence of 30% RH, 50% RH, and 70% RH setpoints. The PID was set to follow the relative humidity inside of the cell through the third tethered sensor. A peak of the humidity at the injection sensors can be observed as the humidity changes. This peak does not affect the humidity at the cell since the humidity change is not instantaneous in the system. Moreover, while the humidity at the cell closely follows the value given to the PID, the exhaust has some latency due to the

dynamical nature of the system.

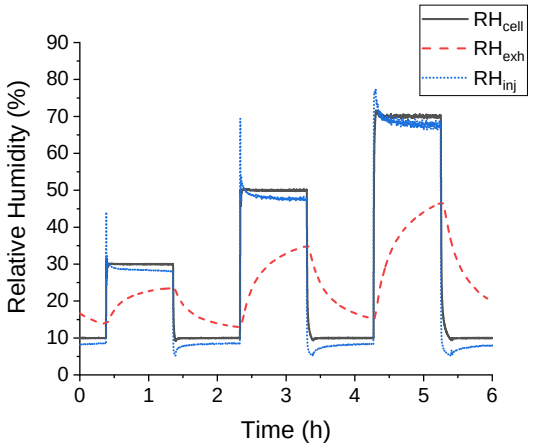


**Figure 6.5** – Pulse sequence alternating between 10% RH and 30% RH, 50% RH, and 70% RH, respectively. The PID control was set to follow the relative humidity inside of the measurement system. The peaks observed at the injection sensor can be attributed to the flow propagation lag, but do not affect the setpoint humidity.

To confirm the long-term reproducibility and stability of the target conditions, we have performed triangular ramps with 10% humidity increments, from 10% RH to 60% RH. The cycle was reproduced four times, and the resulting humidity is shown in Fig. 6.6. Additionally, automated measurement combining humidity ramps while acquiring scanning probe micrographs have been performed unattended for durations of up to three days. Finally, the overall design is durable and has been used for more than two years semi-intensively, only requiring minor maintenance such as the replacement of the ultrasonic nebulizer unit.

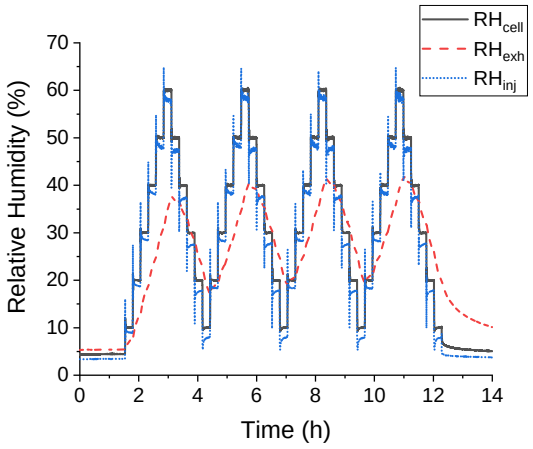


**Figure 6.6** – Four triangular ramp cycles have been performed in order to assess the reproducibility of the humidity conditions. As can be seen, the resulting curves confirm the expected humidity values.

## 6.3 | Additional Young modulus measurements

Young modulus measurements and their clustering are shown in Fig. 6.7 for four more snake species. They do not provide additional insight to the one presented in section 4.2.1, but are shown here for completeness. The measurements on *Corallus Caninus* and *Naja Nivea* does not exhibit significant features, and the clustering was probably based on topographical features. It is also possible that the damaged part show a higher adhesion. *Naja Melanoleuca* is similar in properties to *Panterophis Guttatus*. Finally, *Morelia Viridis* seems to show regions of lower adhesion which are difficult to explain due to their seemingly random distribution on the clustering map.

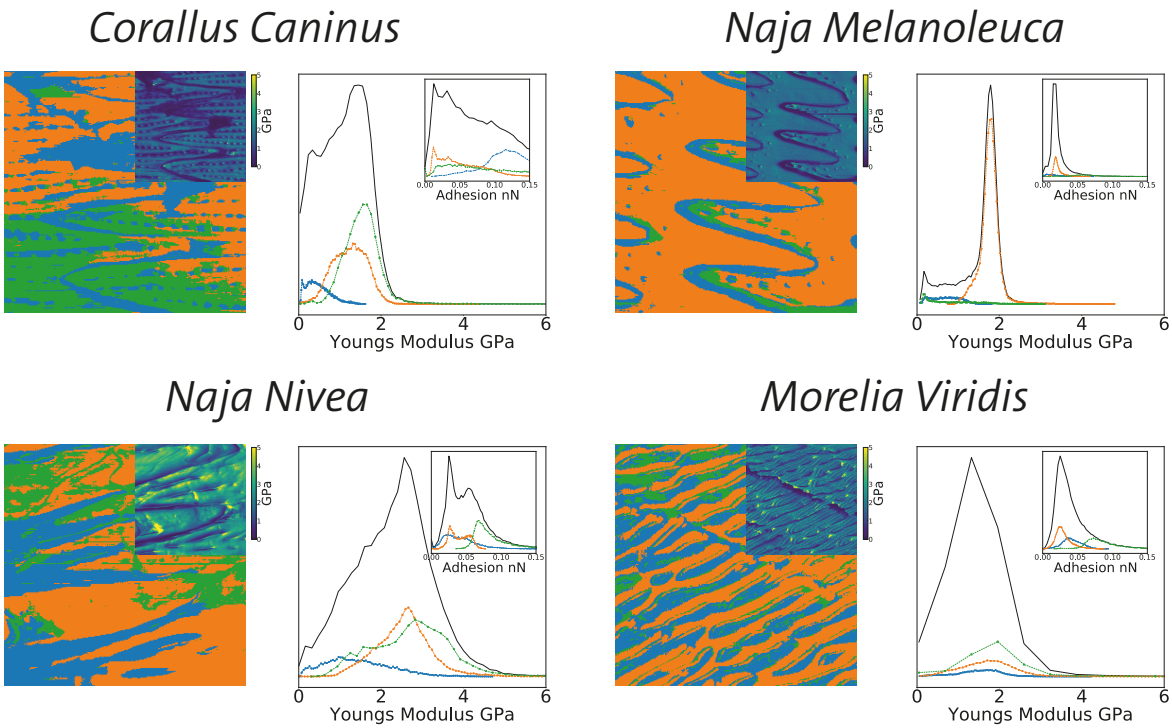


**Figure 6.7** – Supplementary measurements of Young modulus. The histograms of *Corallus Caninus* and *Naja Nivea* do not show clear separation of the histogram features, probably due to the damaged sample surfaces. *Naja Melanoleuca* shows histograms similar to *Panterophis Guttatus*. The green clustering on *Morelia Viridis* presents a higher adhesion, which is difficult to explain since the cluster seems to be randomly placed on the sample.

## 6.4 | Data analysis using K-means clustering

Force map measurements enable multiple physical parameters to be acquired at each point of the AFM scan. From these, we wanted to extract regions with similar properties. To do so, K-means clustering was used. The principle of the algorithm is to generate an N-dimensional space, whit each axis being a measured physical property, and with a distance metric separating points within this space. Centroids are generated randomly in this space (Fig. 6.8(a)): they are the "seeds" of our clusters. The distance between these centroids and all the data points is computed through the specific metric, and the points are assigned to their closest centroid (Fig. 6.8(b)). After the assignment, the centroids are moved to the centre of mass of the clusters (Fig. 6.8(c)). These measurements and assignment steps are repeated until the centroids converge to stationary positions: the clusters are optimized and represent regions on the scan area where the physical properties are similar (Fig. 6.8(d)).

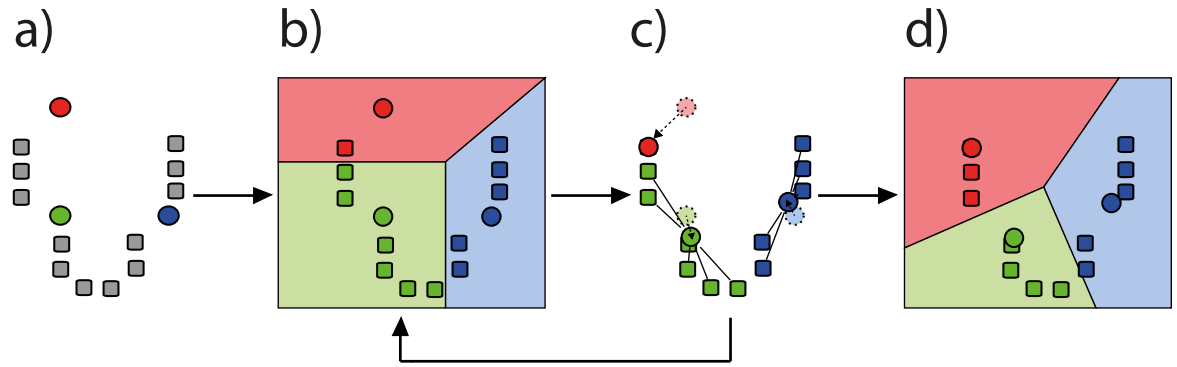


**Figure 6.8** – (a) Centroids are randomly placed in the N-dimensional space. (b) Data point is assigned to a cluster, by taking the shortest distance between the centroids and the data point. (c) The centroid is moved to the center of mass of the cluster. The process in (b) and (c) is repeated until the centroids do not move. (d) The algorithm finished the minimisation, and the clusters correspond to regions with similar properties [52].

## 6.5 | Poster

This work was presented at the 2019 *Deutsche Physikalische Gesellschaft* spring meeting. The poster used for this presentation can be found in Fig. 6.9.

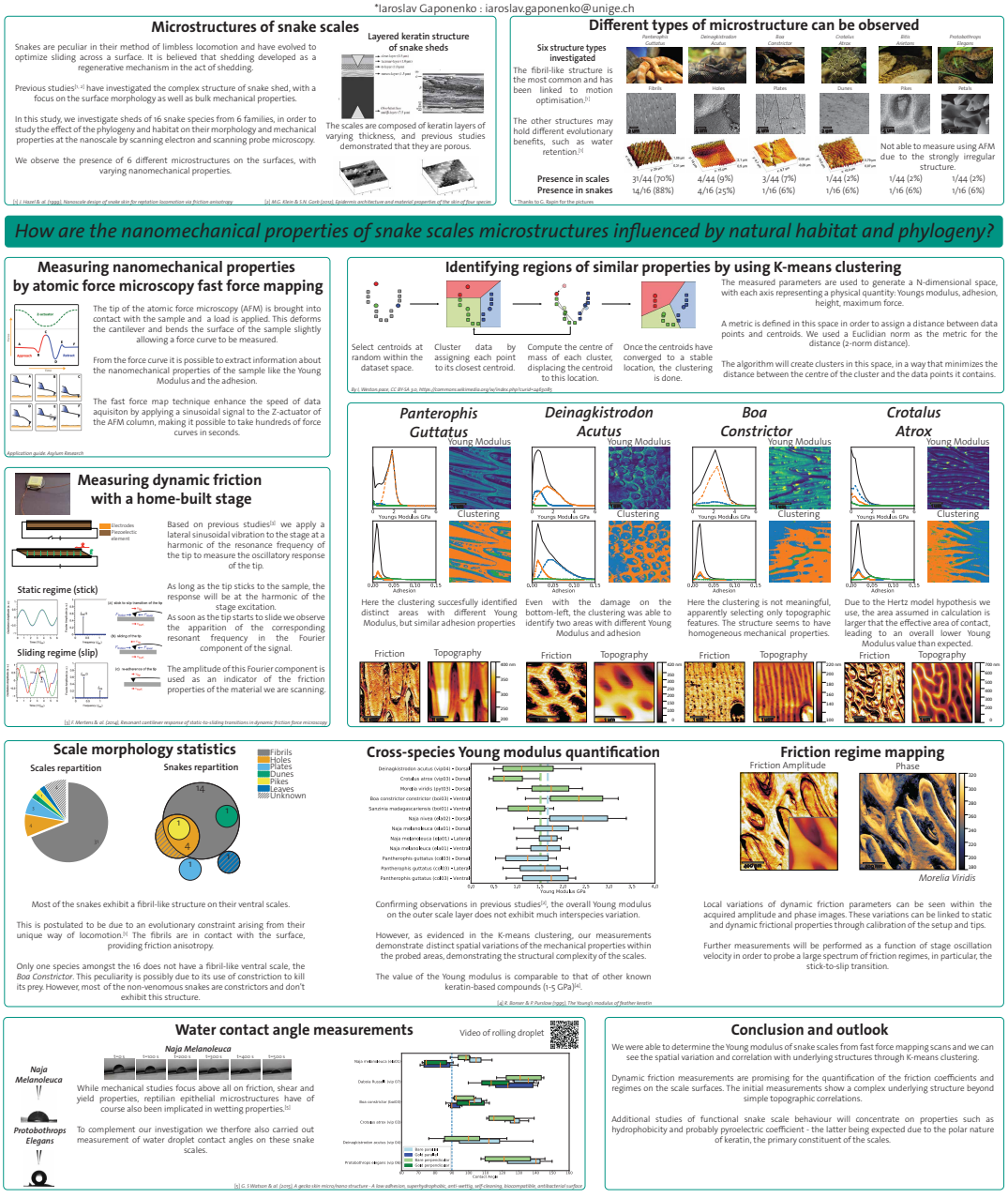


**Figure 6.9** – Poster presented at the 2019 *Deutsche Physikalische Gesellschaft* spring meeting.

# Bibliography


[1] H. A. Abdel-Aal, "Surface structure and tribology of legless squamate reptiles," *Journal of the Mechanical Behavior of Biomedical Materials*, vol. 79, pp. 354–398, Mar. 2018.

[2] W. Mosauer, "On the locomotion of snakes," *Science*, vol. 76, no. 1982, pp. 583–585, 1932.

[3] W. Schöttler, "Die gifte yon vipera latasti und v. lebetina," *Zeitschrift für Hygiene und Infektionskrankheiten*, vol. 120, pp. 408–434, 1983.

[4] A. R. Hoge and P. S. Santos, "Submicroscopic structure of "stratum corneum" of snakes," *Science*, vol. 118, no. 3067, pp. 410–411, 1953.

[5] F. Leydig, "Ueber die äusseren bedeckungen der reptilien und amphibien," *Archiv für mikroskopische Anatomie*, vol. 9, pp. 753–794, Dec 1873.

[6] C. Schmidt and S. Gorb, "Snake scale microstructure: phylogenetic significance and functional adaptations," *Zoologica*, vol. 157, pp. 1–106, 01 2012.

[7] M. I. Arrigo, L. M. De Oliveira Vilaca, A. Fofonjka, A. N. Srikanthan, A. Debry, and M. C. Milinkovitch, "Phylogenetic mapping of scale nanostructure diversity in snakes," *BMC Evolutionary Biology*, vol. 19, Apr. 2019.

[8] J. McKittrick, P.-Y. Chen, S. G. Bodde, W. Yang, E. E. Novitskaya, and M. A. Meyers, "The structure, functions, and mechanical properties of keratin," *JOM*, vol. 64, pp. 449–468, Apr 2012.

[9] J. Hazel, M. Stone, M. S. Grace, and V. V. Tsukruk, "Nanoscale design of snake skin for reptation locomotions via friction anisotropy," *Journal of biomechanics*, vol. 32, no. 5, pp. 477–484, 1999.

[10] M.-C. G. Klein and S. N. Gorb, "Ultrastructure and wear patterns of the ventral epidermis of four snake species (Squamata, Serpentes)," *Zoology*, vol. 117, pp. 295–314, Oct. 2014.

[11] M. Spinner, S. N. Gorb, A. Balmert, H. Bleckmann, and G. Westhoff, "Non-contaminating camouflage: multifunctional skin microornamentation in the west african gaboon viper (Bitis rhinoceros)," *PLoS ONE*, vol. 9, p. e91087, Mar. 2014.

[12] J. Wang, H. Chen, T. Sui, A. Li, and D. Chen, "Investigation on hydrophobicity of lotus leaf: Experiment and theory," *Plant Science*, vol. 176, no. 5, pp. 687 – 695, 2009.

[13] S. Pan, A. K. Kota, J. M. Mabry, and A. Tuteja, "Superomniphobic surfaces for effective chemical shielding," *Journal of the American Chemical Society*, vol. 135, pp. 578–581, Jan. 2013.

[14] E. A. Monroe and S. E. Monroe, "Origin of iridescent colors on the indigo snake," *Science*, vol. 159, no. 3810, pp. 97–98, 1968.

[15] L. D. Landau and E. Lifchitz, *Théorie de l'élasticité*, vol. 7. Editions Mir, 1967. Translated from russian to french by Gloukhian E.

[16] K. L. Johnson, *Contact mechanics*. Cambridge University Press, 1985.

[17] H. Hertz, "Ueber die berührung fester elasticher körper," *Journal füur die reiner une angewandte Mathematik*, vol. 92, pp. 156–171, 1881.

[18] V. L. Popov, *Contact mechanics and friction: physical principles and applications*. Heidelberg ; New York: Springer, english ed. ed., 2010. OCLC: ocn471803040.

[19] E. Meyer, ed., *Nanoscience: friction and rheology on the nanometer scale*. Singapore: World Scientific, reprinted ed., 2002. OCLC: 175169971.

[20] D. Bonn, J. Eggers, J. Indekeu, J. Meunier, and E. Rolley, "Wetting and spreading," *Rev. Mod. Phys.*, vol. 81, pp. 739–805, May 2009.

[21] P.-G. de Gennes, F. Brochard-Wyart, and D. Quere, *capilarity and wetting phenomena*. Springer, 2003. Translated from french to english by Reisinger A.

[22] K.-Y. Law and H. Zhao, *Surface wetting: characterization, contact angle, and fundamentals*. Cham: Springer, 2016. OCLC: 928624396.

[23] L. Gao and T. J. McCarthy, "Wetting 101°," *Langmuir*, vol. 25, pp. 14105–14115, Dec. 2009.

[24] T. S. Meiron, A. Marmur, and I. Saguy, "Contact angle measurement on rough surfaces," *Journal of Colloid and Interface Science*, vol. 274, pp. 637–644, June 2004.

[25] A. K. Batra and M. D. Aggarwal, *Pyroelectric materials: infrared detectors, particle accelerators and energy harvesters*. Bellingham, Washington, USA: SPIE Press, 2013.

[26] A. Bogner, P.-H. Jouneau, G. Thollet, D. Basset, and C. Gauthier, "A history of scanning electron microscopy developments: Towards "wet-stem" imaging," *Micron*, vol. 38, no. 4, pp. 390 – 401, 2007. Microscopy of Nanostructures.

[27] J. Goldstein, ed., *Scanning electron microscopy and x-ray microanalysis*. New York: Kluwer Academic/Plenum Publishers, 3rd ed ed., 2003.

[28] J. Orloff, ed., *Handbook of charged particle optics*. Boca Raton: CRC Press/Taylor & Francis, 2nd ed ed., 2009. OCLC: ocn213765926.

[29] W. Commons, "Interaction volume in scanning electron microscopy." `https://commons.wikimedia.org/wiki/File:Pear_interaction_SEM_english.svg`.

[30] K. Wasa, I. Kanno, and H. Kotera, *Handbook of sputter deposition technology: fundamentals and applications for functional thin films, nanomaterials and MEMS*. Waltham, MA: William Andrew, 2nd ed ed., 2012.

[31] M. Kenneth, *Glow discharge spectroscopies*. Springer-Verlag New York, 2013.

[32] P. J. Eaton and P. West, *Atomic force microscopy*. Oxford ; New York: Oxford University Press, 2010. OCLC: ocn455831540.

[33] B. Voigtländer, *Scanning probe microscopy*. New York, NY: Springer Berlin Heidelberg, 2015.

[34] Y. Cheng and H. Huang, "Van der waals interaction between a molecule and a solid surface," *Chinese journal of physics*, vol. 31, no. 1, pp. 137 – 145, 1993.

[35] G. Binnig, C. F. Quate, and C. Gerber, "Atomic force microscope," *Physical Review Letters*, vol. 56, pp. 930–933, Mar. 1986.

[36] R. Erlandsson, G. M. McClelland, C. M. Mate, and S. Chiang, "Atomic force microscopy using optical interferometry," *Journal of Vacuum Science & Technology A: Vacuum, Surfaces, and Films*, vol. 6, pp. 266–270, Mar. 1988.

[37] Z. Peng and P. West, "Crystal sensor for microscopy applications," *Applied Physics Letters*, vol. 86, p. 014107, Jan. 2005.

[38] M. Tortonese, H. Yamada, R. C. Barrett, and C. F. Quate, "Atomic force microscopy using a piezoresistive cantilever," in *TRANSDUCERS '91: 1991 International Conference on Solid-State Sensors and Actuators. Digest of Technical Papers*, pp. 448–451, June 1991.

[39] S. Alexander, L. Hellemans, O. Marti, J. Schneir, V. Elings, P. K. Hansma, M. Longmire, and J. Gurley, "An atomic-resolution atomic-force microscope implemented using an optical lever," *Journal of Applied Physics*, vol. 65, pp. 164–167, Jan. 1989.

[40] Y. Song and B. Bhushan, "Coupling of cantilever lateral bending and torsion in torsional resonance and lateral excitation modes of atomic force microscopy," *Journal of Applied Physics*, vol. 99, p. 094911, May 2006.

[41] S. Jesse and S. V. Kalinin, "Band excitation in scanning probe microscopy: sines of change," *Journal of Physics D: Applied Physics*, vol. 44, p. 464006, Nov. 2011.

[42] F. Mertens, T. Göddenhenrich, and A. Schirmeisen, "Resonant cantilever response of static-to-sliding transitions in dynamic friction force microscopy," *Applied Physics Letters*, vol. 104, p. 113105, Mar. 2014.

[43] F. Mertens, *Fractional resonance excitation in dynamic friction force microscopy*. PhD thesis, Justus-Liebig-Universität Giessen, 4 2015.

[44] I. Gaponenko, L. Gamperle, K. Herberg, S. C. Muller, and P. Paruch, "Low-noise humidity controller for imaging water mediated processes in atomic force microscopy," *Review of Scientific Instruments*, vol. 87, no. 6, 2016.

[45] I. Gaponenko, L. Musy, S. Muller, and P. Paruch, "Open source standalone relative humidity controller for laboratory applications." Submitted to Engineering Research Express, 2019.

[46] A. Stalder and Biomedical Imaging Group of École Polytechnique Fédérale de Lausanne, "Drop shape analysis — free software for high precision contact angle measurement.." `http://bigwww.epfl.ch/demo/dropanalysis/`. Accessed: 2019-06-05.

[47] D. Denning, M. Abu-Rub, D. Zeugolis, S. Habelitz, A. Pandit, A. Fertala, and B. Rodriguez, "Electromechanical properties of dried tendon and isoelectrically focused collagen hydrogels," *Acta Biomaterialia*, vol. 8, pp. 3073–3079, Aug. 2012.

[48] M. Spinner, A. Kovalev, S. N. Gorb, and G. Westhoff, "Snake velvet black: Hierarchical micro- and nanostructure enhances dark colouration in Bitis rhinoceros," *Scientific Reports*, vol. 3, Dec. 2013.

[49] B. A. Bober, J. K. Ogata, V. E. Martinez, J. J. Hallinan, T. A. Leach, and B. Negru, "Investigating nanoscopic structures on a butterfly wing to explore solvation and coloration," *Journal of Chemical Education*, vol. 95, pp. 1004–1011, June 2018.

[50] H. Landolt and R. Börnstein, *Numerical data and functional relationships in science and technology - New Series*, vol. Condensed Matter (Group III). Springer, 2015.

[51] I. Gaponenko, L. Musy, S. Muller, and P. Paruch, "Open Humidity Controller GitLab repository with all of the system diagrams, mechanical schematics, client/server software and example scripts." `https://gitlab.unige.ch/paruch-group/open-humidity-controller`. Accessed: 2019-05-17.

[52] P. Weston, "K-means clustering." `https://en.wikipedia.org/wiki/K-means_clustering`. Accessed: 2019-08-05.